UNIVERSITY OF CALIFORNIA, SAN DIEGO

A Bayesian Approach to Matched-Field Geoacoustic Inversion with Analysis of ASIAEX Experimental Data

A dissertation submitted in partial satisfaction of the
requirements for the degree Doctor of Philosophy
in
Oceanography

by

Chen-Fen Huang

Committee in charge:

William S. Hodgkiss, Chair
Michael J. Buckingham
William A. Coles
Peter Gerstoft
William A. Kuperman
Robert Pinkel

2005

ProQuest Information and Learning Company
300 North Zeeb Road
P.O. Box 1346
Ann Arbor, MI 48106-1346

The dissertation of Chen-Fen Huang is approved, and it is acceptable in quality and form for publication on microfilm:

William A Coles

Robert Pinkel

Peter Gerstoft

William

Michael J.

W Hodgkiss

Chair

University of California, San Diego

2005

TO
MY PARENTS
FOR THEIR
UPBRINGING
AND
ENCOURAGEMENT
THROUGHOUT THE YEARS AT
SIO

TABLE OF CONTENTS

Signature Page . . . iii

Dedication . . . iv

Table of Contents . . . v

List of Symbols . . . viii

List of Figures . . . x

Acknowledgements . . . xiii

Vita, Publications, and Fields of Study . . . xv

Abstract . . . xix

1 Introduction . . . 1
- 1.1 Background and Objectives . . . 1
- 1.2 Basic Concepts . . . 2
- 1.3 Scope of the Dissertation . . . 5

2 Geoacoustic Inversion of Low-Frequency Data . . . 7
- 2.1 Introduction . . . 7
- 2.2 Data Acquisition . . . 10
  - 2.2.1 Experimental Geometry . . . 10
  - 2.2.2 Oceanographic Measurements . . . 11
  - 2.2.3 Seismic Measurements . . . 11
- 2.3 Data Processing . . . 14
- 2.4 Matched-Field Geoacoustic Inversion . . . 17
  - 2.4.1 Acoustic Propagation Model . . . 17
  - 2.4.2 Environmental and Array Parameterizations . . . 17
  - 2.4.3 Objective Function . . . 20
  - 2.4.4 Sensitivity Analysis . . . 22
  - 2.4.5 Genetic Algorithms . . . 22
  - 2.4.6 Uncertainty Estimates . . . 24
- 2.5 Results and Discussion . . . 24
  - 2.5.1 Source Localizations . . . 30
  - 2.5.2 Inversion Results over Time . . . 32
- 2.6 Conclusions . . . 36

3 Mid-Frequency Data Analysis . . . 41
- 3.1 Sensitivity Analysis . . . 41
- 3.2 Model Parameter Estimation . . . 43
- 3.3 Results and Discussion . . . 44
- 3.4 Conclusions . . . 49

4 Uncertainty Estimation 50
4.1 Introduction 50
4.2 Formulation of the Inverse Problem 53
4.2.1 Single frequency matched-field likelihood function 54
4.2.2 Multi-frequency matched-field likelihood function 55
4.2.3 Noninformative priors 57
4.3 Error Variance as a Nuisance Parameter 58
4.3.1 Full Bayesian estimation – numerical integration 58
4.3.2 Full Bayesian estimation – analytic integration 58
4.3.3 Empirical Bayesian estimation – optimizing error variance jointly with model parameters 60
4.3.4 Empirical Bayesian estimation – maximum likelihood estimate . . . 60
4.4 PPD of the Error Variance 61
4.5 Results and Discussion 63
4.5.1 Synthetic data 63
4.5.2 Experimental data 69
4.6 Conclusions 73
4.7 Appendix: Additive noise 74

5 Estimation of Transmission Loss: *A Posteriori* Analysis 77
5.1 Introduction 78
5.2 Inverse Problem Framework 80
5.2.1 Probability of **u** 81
5.2.2 Likelihood and Objective Function 81
5.3 Examples 83
5.3.1 TC1 – Inversion 84
5.3.2 TC1 – TL Estimation 86
5.3.3 ASIAEX – Inversion 90
5.3.4 ASIAEX – TL Estimation 93
5.4 Conclusions 95

6 Conclusions 97
6.1 Conclusions 97
6.2 Suggestions for Future Research 99

A Parabolic-Shape Array 101

B Empirical Orthogonal Functions 103
B.1 Recipes 103
B.2 Example: EOF Analysis on ASIAEX CTD Data 104

C Monte Carlo Sampling Algorithm 110
C.1 Numerical Integration 111
C.1.1 Metropolis-Hastings Sampler 112
C.2 Monte Carlo Sampling Algorithm Implemented in SAGA 114
C.2.1 Burn-in Period 114

    - C.2.2 Sampling PPD of $\mathbf{m}$ 114
    - C.2.3 Convergence Monitoring 116
- C.3 Options in SAGA 116

Bibliography 118

LIST OF SYMBOLS

$\mathbf{C}_{\mathrm{D}}$	Data covariance matrix
$\widehat{\mathbf{C}}_{\mathrm{M}}$	Posterior covariance matrix of model parameters
$\mathcal{CN}$	Symbol denoting the complex Gaussian distribution
$\mathbf{d}$	Vector of complex-valued pressure data; observed data
$\mathbf{d}(\mathbf{m})$	Vector for replica acoustic pressure fields (normalized to have unit length) computed from an acoustic propagation model for the model parameter $\mathbf{m}$
$\mathbf{D}(\mathbf{m})$	Forward model that maps $\mathbf{m}$ from the environmental domain to the data domain
$\mathcal{D}$	Data domain
$\boldsymbol{\eta}$	Vector of nuisance parameters
$\mathbf{I}$	Identity matrix
J	Number of processed frequencies
$\mathbf{K}$	Matrix of derivatives of the forward model with respect to a model parameter vector
$\mathcal{L}$	Likelihood function
$\mathbf{m}$	Vector of model parameters
$\widehat{\mathbf{m}}$	Maximum *a posteriori* (MAP) or maximum likelihood (ML) estimate of model parameter vector
M	Number of model parameters
M^*	Number of well-determined model parameters
$\mathcal{M}$	Environmental domain
$\mathbf{n}$	Vector of data errors; the residual variations between the observed data $\mathbf{d}$ and the modeled data $\mathbf{D}(\mathbf{m})$
N	Number of sensors in an array
ν	Variance of the data errors
$\mathrm{p}(x\|y)$	Conditional probability density function of x given y
$p(r, z)$	Acoustic pressure field at a range r and depth z
$P_{\mathrm{BT},\, l}$	Bartlett power for the l-th processed frequency
$\phi(\cdot)$	Objective function

Φ_n	n-th normal mode corresponding to the horizontal wavenumber k_{rn}
$\mathbf{R}$	Correlation matrix of the observed data, cross-spectral density matrix
s	Complex-valued source strength
$\mathbf{u}$	Vector of field of interest; transmission loss at different frequencies, depths and ranges
$\mathbf{U}(\mathbf{m})$	Forward model that maps $\mathbf{m}$ from the environmental domain to the usage domain
$\mathcal{U}$	Usage domain

LIST OF FIGURES

1.1 Bayesian approach to matched-field geoacoustic inversion. 3

2.1 Plan view of the ASIAEX 2001 East China Sea experiment. 9
2.2 Side view of the experimental geometry. 10
2.3 Time-series plots of current speed and current vector stick 12
2.4 Measured sound-speed profiles by the CTDs on JD 158. 13
2.5 Time-evolving signal power and noise floor across the elements for 95, 195, 295, and 395 Hz. 15
2.6 Maximum obtainable Bartlett power versus time. 16
2.7 Geoacoustic model and experimental configuration for the ASIAEX 2001 East China Sea experiment 18
2.8 Empirical Orthogonal Function (EOF) analysis for the 2001 ASIAEX CTD casts. 19
2.9 The sensitivity index for the model parameters 23
2.10 Marginal dot diagrams of the SAGA search for the model parameters. 26
2.11 Two-dimensional cross-sections of Bartlett power for the selected model parameter 28
2.12 Comparison of the observed and modeled fields on the vertical array . 29
2.13 Range-depth ambiguity surfaces at SR = 1.7 km. 31
2.14 Range-depth ambiguity surfaces at SR = 2.8 km. 31
2.15 MF correlations over time for different array tilts at 295 Hz. 32
2.16 MF-derived source-receiver range over the time interval from 20 to 50 min. 33
2.17 MF-derived source depth over the same time interval shown in Fig. 2.16. 33
2.18 The inverted environmental parameter values versus time. 37
2.18 (cont'd) The inverted environmental parameter values versus time. . . 37
2.19 Normalized received levels for the measured and normalized modeled fields as a function of time for the selected array elements 38
2.20 Correlation coefficient matrix for the environmental parameters computed using the inversion results shown in Fig. 2.18. 38

3.1 Sensitivity study of the model parameters for mid-frequency data analysis 42
3.2 Comparison of the estimated sound-speed profiles from the inversions 44
3.3 Range-depth ambiguity surfaces at SR = 1.7 km for each source frequency and the multi-frequency average. 47
3.4 Comparison of MF-derived source-receiver range and source depth over the time interval from 20 to 50 min. (a) The replica pressure field is computed using the low-frequency-derived best-fit model. (b) The replica pressure field is computed using the best-fit model derived from all 6 frequencies. 48

4.1 Posterior distribution of ν with a log-uniform prior on ν. 63

4.2 The **sdc** environment from the Geo-Acoustic Inversion Workshop 1997. 64
4.3 Range-depth transmission loss for $F = 100$ and 200 Hz, respectively using the **sdc** environment. The two white lines mark the water-sediment (top) and sediment-subbottom (bottom) interfaces. 65
4.4 Full Bayesian approach. 1-D and 2-D marginal posterior probability densities (PPDs) of the geoacoustic parameters as well as the error variance for $F = 100$ Hz. 66
4.5 Posterior marginal distribution of the error variance for $F = 100$ Hz. . 66
4.6 Comparison of the marginal PPDs for the model parameters using different approaches in the error variance (synthetic data. $F = 100$ Hz). 67
4.7 Full Bayesian approach. 1-D and 2-D marginal PPDs of the geoacoustic parameters as well as the error variance for 200 Hz. 68
4.8 Full Bayesian approach for the multi-frequency case (synthetic data). 70
4.9 Full Bayesian approach for the multi-frequency case (experimental data). 71
4.10 Posterior marginal distribution of the error variance (experimental data). 72
4.11 Comparison of the marginal PPDs for the model parameters using different approaches in the error variance (experimental data). 73

5.1 An observation $\mathbf{d}$ ($\in \mathcal{D}$) is mapped into a distribution of environmental parameters $\mathbf{m}$ ($\in \mathcal{M}$) that potentially could have generated it. These environmental parameters are then mapped into the usage domain $\mathcal{U}$. 78
5.2 Inversion results for Test Case 1 (TC1). 85
5.3 Marginal distributions for TC1 bottom sound speed profile. 86
5.4 Prior and posterior probability distributions for TL versus range at 80-m depth for TC1. 87
5.5 Prior and posterior probabilities of TL at 4200-m range and 80-m depth. 87
5.6 Median TL (dB) obtained from prior and posterior distributions of environmental parameters. 88
5.7 Range (dB) between 5th and 95th percentiles of the TL for prior and posterior probabilities. 89
5.8 Median TL and the true TL at 80-m depth obtained from prior and posterior samples. 89
5.9 Marginal scatter diagrams of the SAGA search for the model parameters (Repeated from Fig. 2.10). 91
5.10 Marginal probabilities for water depth and sediment sound speed. . . 91
5.11 Prior and posterior probability distributions for TL versus range at 50-m depth. 92
5.12 Prior and posterior probabilities of TL at 830-m range and 50-m depth. 93
5.13 Median TL (dB) obtained from prior and posterior distributions of environmental parameters. 94
5.14 Range (dB) between 5th and 95th percentiles of the TL for prior and posterior probabilities. 94
5.15 Median TL at 50-m depth obtained from prior and posterior samples. 95

A.1 Bowed-array shape in xz-plane and the depth deviation of the uppermost element for different bows: 0 m, 0.5 m, 1 m, 1.5 m and 2 m. 102

B.1 Empirical Orthogonal Function (EOF) analysis for the 2001 ASIAEX CTD casts. 105
B.2 Upper panel: measured sound-speed profiles as a function of time. Lower panel: time series of the estimated EOF coefficients of the above measured sound-speed profiles. 106
B.3 Reconstructed CTD0123 SSPs using the mean plus different numbers of EOFs. 107
B.4 Reconstructed CTD0547 SSPs using the mean plus different numbers of EOFs. 108
B.5 Reconstructed CTD0820 SSPs using the mean plus different numbers of EOFs. 109

ACKNOWLEDGMENTS

I am gratefully indebted to Professor William Hodgkiss for suggesting this thesis problem and for guiding it to its completion. his patience, encouragement, guidance and support. I am grateful beyond words for this life changing experience.

I would like to thank Dr. Peter Gerstoft who introduces me to the world of inverse theory, which is the second subject of my dissertation. He kept my motivation high by always having his door opened to me for countless discussions on this and many other subjects.

I would like to express my gratitude to each of my committee members, Professors William Kuperman, Michael Buckingham, Robert Pinkel, and William Coles for useful comments and discussing various topics related with my study.

I would like to thank the crew of R/V *Melville*, Richard Harris, Dave Ensberg and Jeff Skinner as well as the other participants in the scientific party of ASIAEX experiment.

I would like to thank everybody in the Marine Physical Lab for their input, not only the caffeine input, or academically, but also for dragging me along on hiking or other physical activity. I wish to express my gratitude to Evelyn Doudera, Diana Stockdale, Irina Tsimring, Arron Thode, Geoff Edelmann, Seongil Kim, Katherine Kim, Karim G. Sabra, Eric Giddens, Caglar Yardim, and Rich Yen.

I would like to thank my dear friends, Fernando, Karen, Guoqing Lin, Dori, Sky Yu, and Yi-Hsien Su. From them, I have learned that there is something, other than the research, important to the life.

I would like to thank Professor Jin-Yuan Liu for introducing ocean acoustics to me during my study in National Sun Yat-sen University, 1997.

This work was supported by the Office of Naval Research, Grant Nos. N00014-01-1-0096 and N00014-01-1-0171; to them I would like to express my profound thanks for their financial support.

Finally, I wish to express my most grateful thanks to my uncle and my parents for their spiritual and financial support throughout the years at SIO. Without their understanding and support I would not have been able to give full attention to this work and to complete it successfully.

The text of Chapter Two in part is a reprint of the material as it appears in Chen-Fen Huang and William S. Hodgkiss, "Matched field geoacoustic inversion of low frequency source tow data from the ASIAEX East China Sea experiment," IEEE J. Oceanic Eng., Vol. 29, 952–963, 2004. The dissertation author was the primary researcher/author and the co-author listed in this publication directed and supervised the research which forms the basis for this chapter.

VITA

1995	B.S., National Sun Yat-sen University, Kaohsiung, Taiwan
1997	M.S., National Sun Yat-sen University, Kaohsiung, Taiwan
1998	M.S., National Sun Yat-sen University, Kaohsiung, Taiwan
1998–2000	Research Assistant, National Sun Yat-sen University, Kaohsiung, Taiwan
2005	Doctor of Philosophy University of California, San Diego

PUBLICATIONS

Journals

1. Chen-Fen Huang, Peter Gerstoft, and William S. Hodgkiss, "Uncertainty analysis in matched-field geoacoustic inversion," J. Acoust. Soc. Am., (accepted upon revision, 2005)
2. Peter Gerstoft, Chen-Fen Huang, and William S. Hodgkiss, "Estimation of transmission loss in the presence of geoacoustic inversion uncertainty," IEEE J. Oceanic Eng., (in press, 2005)
3. Chen-Fen Huang and William S. Hodgkiss, "Matched field geoacoustic inversion of low frequency source tow data from the ASIAEX East China Sea experiment," IEEE J. Oceanic Eng., Vol. 29, 952–963, 2004.
4. Jin-Yuan Liu, Ping-Chang Hsueh, and Chen-Fen Huang, "Coherent reflection of acoustic plane wave from a rough seabed with random sediment layer overlying an elastic basement," IEEE J. Oceanic Eng., Vol. 27, 853–861, 2002.
5. Jin-Yuan Liu, Chen-Fen Huang, and Ping-Chang Hsueh, "Acoustic plane-wave scattering from a rough surface over a random fluid medium," Ocean Engineering, Vol. 29, No. 8, 915–930, 2002.
6. Bang-Fuh Chen and Chen-Fen Huang, "Hydrodynamic forces on concrete sea wall and breakwater during earthquake: effects of bottom sediment layers and back-fill soil," Ocean Engineering, Vol. 29, No. 7, 783–814, 2002.
7. Jin-Yuan Liu, Chen-Fen Huang, and Shiahn-Wern Shyue, "Effects of seabed properties on acoustic wave fields in a seismo-acoustic ocean waveguide," Ocean Engineering, Vol. 28, No. 11, 1437–1459, 2001.
8. Jin-Yuan Liu and Chen-Fen Huang, "Acoustic plane-wave interaction with a randomly inhomogeneous slab bounded by rough surfaces," Journal of Sound and Vibration, Vol. 241(3), 441–457, 2001.
9. Jin-Yuan Liu and Chen-Fen Huang, "Acoustic plane-wave reflection from a rough surface over a random fluid half-space," Ocean Engineering, Vol. 28, No. 7, 751–762, 2001.

10. Jin-Yuan Liu and Chen-Fen Huang, "Acoustic plane-wave scattering from a rough interface over an inhomogeneous transition fluid layer," Ocean Engineering, Vol. 28, No. 6, 603–619, 2001.
11. Jin-Yuan Liu and Chen-Fen Huang, "Effects of medium inhomogenieties on surface-generated ambient noise," Proc. Natl. Sci. Counc. ROC(A), Vol. 25, No. 1, 45–52, 2001.
12. Jin-Yuan Liu, Chau-Chang Wang, and Chen-Fen Huang, "Coherent reflection from a rough interface over an inhomogeneous transition fluid layer," Journal of Computational Acoustics, Vol. 8, No. 3, 401–414, 2000.
13. Jin-Yuan Liu and Chen-Fen Huang, "Surface-generated noise in an ocean waveguide with a transition layer of continuously varying density and sound speed," Journal of Computational Acoustics, Vol. 7, No.4, 253–268, 1999.
14. Bang-Fuh Chen and Chen-Fen Huang, "Nonlinear hydrodynamic pressures generated by a moving high rise offshore cylinder," Journal of Ocean Engineering, Vol. 24, No. 3, 201–216, 1997.

Conference Proceedings

1. Caglar Yardim, Peter Gerstoft, William S. Hodgkiss, and Chen-Fen Huang, "Refractivity from clutter (RFC) estimation using a hybrid genetic algorithm – Markov chain Monte Carlo method," IEEE APS international and USNC/URSI National Radio Science meeting, 2005.
2. Peter Gerstoft, Chen-Fen Huang, and William S. Hodgkiss, "Estimation of transmission loss and its uncertainty," Conference on Acoustic Inversion methods and Experiments, Ischia, 2004.
3. Peter Gerstoft, Chen-Fen Huang, William S. Hodgkiss, and Peter Nielsen, "Posterior transmission loss from ocean acoustic data," Sixth European conference on underwater acoustics, Delft, 2004.
4. Chen-Fen Huang and William S. Hodgkiss, "Mid-frequency geoacoustic inversion of source tow data from the ASIAEX East China Sea experiment," Oceans2003 MTS/IEEE Conference Proceedings, San Diego, California, 576–581, 2003.
5. Jin-Yuan Liu and Chen-Fen Huang, "Surface-generated noise in an ocean waveguide with an inhomogeneous transition layer," Oceans'99 MTS/IEEE Conference Proceedings, Seattle, Washington, Vol. 1, 439–445, 1999.

Presentations with Abstract

1. Jin-Yuan Liu, Li Ding, and Chen-Fen Huang, "The Concept of acoustic monitoring in Kaohsiung harbor area in Southern Taiwan," Turkish International Conference on Acoustics, Istanbul, Turkey, 2005.
2. Chen-Fen Huang, Peter Gerstoft, and William S. Hodgkiss, "Influence of data uncertainty on matched-field geoacoustic inversion," J. Acoust. Soc. Am., 115, 2409, 2004.
3. Peter Gerstoft, Chen-Fen Huang, and William S. Hodgkiss, "Iterative geoacoustic inversion," J. Acoust. Soc. Am., 115, 2408, 2004.
4. Chen-Fen Huang and William S. Hodgkiss, "Geoacoustic inversion results of low- to high-frequency source tow data from the ASIAEX East China experi-

ment," J. Acoust. Soc. Am., 114, 2344, 2003.

5. Chen-Fen Huang and William S. Hodgkiss, "Source tow geoacoustic inversions from the 2001 ASIAEX East China Sea experiment," J. Acoust. Soc. Am., 112, 2283, 2002.
6. Chen-Fen Huang, Philippe Roux, and William A. Kuperman, "Computing the two-point correlation function directly from the transport equation using split-step Padé solutions," J. Acoust. Soc. Am., 112, 2394, 2002.
7. Chen-Fen Huang and William S. Hodgkiss, "Low-frequency source tow geoacoustic inversions from the 2001 ASIAEX East China Sea experiment," J. Acoust. Soc. Am., 112, 2283, 2002.

FIELDS OF STUDY

Major Field: Applied Ocean Science

Studies in Applied Mathematics.
Professors William R. Young and Stefan L. Smith

Studies in Physical Oceanography.
Professors Lynne D. Talley and Myrl C. Hendershott

Studies in Biological Oceanography.
Professors Lisa Ann Levin and David Checkley

Studies in Marine Chemistry.
Professors Joris M. Gieskes and Ralph F. Keeling

Studies in Marine Geology.
Professor Peter F. Lonsdale

Studies in Underwater Acoustics.
Professors William A. Kuperman and Michael J. Buckingham

Studies in Digital Signal Processing and Array Signal Processing.
Professor William S. Hodgkiss

Studies in Geophysical Inverse Theory.
Professor Catherine G. Constable

ABSTRACT OF THE DISSERTATION

A Bayesian Approach to Matched-Field Geoacoustic Inversion
with Analysis of ASIAEX Experimental Data

by

Chen-Fen Huang
Doctor of Philosophy in Oceanography
University of California, San Diego, 2005
Professor William S. Hodgkiss, Chair

This dissertation applies a Bayesian framework for making quantitative statistical inferences about geoacoustic properties from ocean acoustic data using matched-field processing techniques. Data acquired during the ASIAEX 2001 East China Sea experiment are used to infer the geoacoustic properties.

In a Bayesian approach, information and uncertainty regarding model parameters obtained from the measurements are summarized in the posterior probability distribution. This posterior distribution is proportional to the product of a prior distribution (which incorporates information on model parameters before the measurements) and of a likelihood function (which quantifies how well a model fits the measurements). From this posterior distribution of model parameters, we obtain all information about the model parameters, such as maximum *a posteriori* estimate (best-fit model), mean as well as standard deviation.

The quality of the best-fit model is checked using matched-field processing for source localization. In the less than 1 kHz frequency band, the effect of environmental mismatch on source tracking can be reduced by using inversion techniques to estimate geoacoustic parameters, resulting in improved source localization performance. The parameter uncertainty (in terms of mean and standard deviation) given by the Bayesian approach is validated by comparing the variabilities of the estimated parameters inverted from multiple independent data sets.

A Bayesian approach to inverse problems requires estimation of the uncertainties in the data. An extension of the Bayesian parameter uncertainty analysis to include the uncertainty of data errors is carried out. Following a full Bayesian methodology, we derive the analytic expressions for the posterior probability distribution of the model parameters for both single and multi-frequency data.

The impact of uncertainty embedded in the geoacoustic inversion results on the estimation of transmission loss is investigated. An approach for estimating the statistical properties of transmission loss is developed using information on the model parameters obtained from the inversion. The utility of this approach is that one can compute the probability distributions of transmission loss at all frequencies, ranges and depths. Examples demonstrate the use of transmission loss probability density functions to extract characteristic features such as median and lower/upper percentiles.

Chapter 1

Introduction

1.1 Background and Objectives

Inferring geoacoustic properties indirectly from the measured sound fields in an oceanic environment using various signal processing schemes, referred to as ocean geoacoustic inversion, is an important application of underwater sound. This subject has attracted the attention of several researchers in the past decade, resulting in both theoretical [10,21,22,24,27–35,38,39,41] and experimental [13,25,29,40,42,57,75] work. Many studies have shown that even though the inversion results may present some degree of uncertainty, the techniques still prove to be a valuable and promising means of estimating environmental parameters. In particular, geoacoustic inversion is most useful for estimating those environmental variables that are difficult to approach directly on site, such as the density and sound speed (compressional or shear) profiles of the sea floor.

The primary objective of this dissertation is to carry out an analysis of geoacoustic inversion, based upon field data obtained in the Asian Seas International Acoustics EXperiment (ASIAEX). ASIAEX was an international scientific endeavor involving ocean acousticians from the United States and several countries surrounding the west Pacific Rim, including the People's Republic of China, the Republic of Korea, Japan, Taiwan, Russia, and Singapore. The major field experiments of ASIAEX were conducted from May to August of 2001 and consisted of two parts: the South China Sea (SCS) experiment and the East China Sea (ECS) experiment. The SCS experiment placed emphases on acoustic propagation over the continental shelf and acoustic interactions with a dynamic oceanographic environment (specifically, internal waves), while the ECS experiment concentrated on boundary interactions, reverberation, and geoacoustic inversion. The complete program and some results to-date have been published in the IEEE Journal of Oceanic Engineering Special Issue on the Asian Marginal Seas (2004) [59].

As a part of the ASIAEX ECS program, data were collected to invert for the geoacoustic properties in the ECS using acoustic measurements over the frequency range of $O(100 - 1000)$ Hz. The data obtained are analyzed in this thesis. These data supplemented by the comprehensive oceanographic and geophysical measurements also obtained during the experiment are used to assess quantitatively the reliability of the inverted parameters and the employed seafloor model.

During the past decade, substantial effort has been devoted to the development of computational algorithms for inversion [27–29, 32, 33]. Among others, the SAGA program for geoacoustic inversion [34] has been widely accepted and is used in this research. The state-of-the-art has reached the point that many important issues such as uncertainties due to measurement noise and modeling errors as well as robustness for *a posteriori* estimation are now worthy of more consideration. These subjects also constitute another part of the objectives of this dissertation.

1.2 Basic Concepts

Matched-Field Geoacoustic Inversion

In this thesis, matched-field (MF) geoacoustic inversion techniques are applied to estimate seafloor properties. The concept of MF processing where a passive array of receivers is used to locate in range and depth (and bearing) an acoustic source traveling in a *known* oceanic environment was introduced to the underwater acoustics community by Bucker [10]. Many studies [10, 21, 30, 39, 41] have shown that MF processing for source localization is sensitive with respect to the variations of, or the "mismatch" of, the environmental parameters, such as sound speed profiles, water depth, seabed properties, etc. As a result, the concept of employing the procedure "inversely" by treating the environment, and/or source position itself, as *unknowns* and obtaining them from the

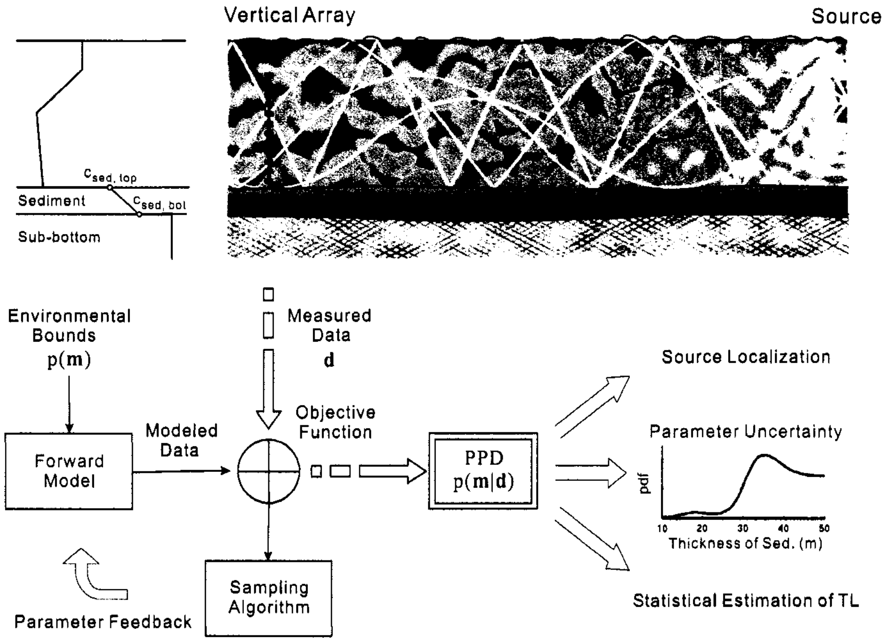

Figure 1.1: Bayesian approach to matched-field geoacoustic inversion.

sound field has been conceived and developed [25,31,40,42].

MF geoacoustic inversion uses measurements of the acoustic field made at an array of hydrophones to extract information on the parameters that determine sound propagation in the ocean. The procedure is shown schematically in Figure 1.1. Given some measured data and some prior information on the values of a parameterized environmental model (e.g., the ocean and sediment sound speeds, attenuations and their thicknesses), a theoretical relationship (the forward model) is constructed to relate the predicted data to the environmental model parameters. Then, by minimizing an appropriate objective function that measures the difference between the measured data and the predictions from the forward model, a set of parameters that best describes the environment is obtained.

Due to the fact that inversion problems make inferences about the environmental parameters using a finite set of noisy data, one always faces the problem of nonuniqueness, i.e., more than one solution can represent the data at hand. The Bayesian approach is adopted in this analysis. The solution of the inverse problem is not only to find a single model parameter vector that fits the measurements best, referred to as the best-fit model, but also to assess the uncertainty of the estimated model parameter.

Bayesian Approach

Since the analysis of geoacoustic inversion always involves errors (noise) and uncertainties in the observed data and model parameters, which may be characterized by probability density functions, probability theory is thus invoked in this study.

There are, however, two different interpretations of probability [76, p. 16][60, p. 25]. In the "frequentist" interpretation, probability is used to describe the likelihood of a particular event occurring in a series of repeated experiments; the higher the value, the more it is likely to occur. On the other hand, in the "Bayesian" interpretation [50], probability is simply used to describe the degree of belief of a predicted value, based upon a single experiment. Here, the Bayesian framework of probability is adopted.

The probabilistic approach in geophysics was pioneered by Tarantola and Valette [78], and Tarantola [76]. The formulation presented in the Tarantola's book is general enough to cover a wide variety of problems in applications. Recently, the Bayesian framework has been adopted in underwater acoustics by some researchers [22, 32, 38].

The fundamental objective of Bayesian inference is to obtain the posterior probability distribution (PPD) of the model parameters. This posterior distribution consists of the product of two probability density functions. The first, the likelihood function, defines what it means for a model to fit the data. The likelihood function quantifies the misfit between the measured data and the modeled data generated by a forward model. Thus, this function takes into account the noise in the measured data as well as the error in the forward modeling procedure. The second, the prior density function, incorporates our *a priori* understanding of model parameters before having access to the measured data.

Using a Bayesian approach to inverse problems requires estimation of the uncertainties in the data due to ambient noise as well as modeling errors. The variance parameter of the Gaussian error model, referred to as error variance, is assumed to describe the data uncertainties. In practice, this parameter is often poorly known *a priori*, and choosing a particular value is often problematic. Hence, to account for the uncertainty in the error variance, several methods are introduced to implement both the full and the empirical Bayesian approaches. A full Bayesian approach permitting uncertainty of the error variance to propagate through the parameter estimation processes is a natural approach. However, the computational effort is substantial. Thus, several methods using an empirical Bayesian approach were developed in which the posterior distributions of model parameters are conditioned on a point estimate of the error variance.

Using the Inversion Results: *A Posteriori* Analysis

In Bayesian inference, all information on the model parameters is derived from the PPD. Such information can be expressed in many ways, for instance, as error bars on the parameter estimates, or marginal PPDs of the model parameters. All of these are explored in this work.

The variability in the geophysical properties of the ocean bottom has a significant impact on sonar performance in shallow water. A key element in the sonar equation is transmission loss (TL) which requires the information on the geoacoustic properties at site.

Recent work related to translating the environmental uncertainty to sonar performance predictions has been undertaken by Abbot and Dyer [1]. In their approach, a probabilistic description of TL was estimated at a given range where many acoustic measurements were made. Then the TL probability density function is assumed to apply universally for all ranges. It does not account for the spatial variations of TL due to multi-path propagation.

Here, we use a Bayesian probabilistic approach to estimate the statistical properties of TL in the presence of geoacoustic inversion uncertainty. Since TL is estimated from a full wave solution, the resulting probability density function of TL should be more representative.

1.3 Scope of the Dissertation

The major contents of this dissertation consist of four chapters, Chapters 2 to 5[1]. Chapter 2 is devoted to the analysis of ASIAEX ECS experimental data. The

---

[1] Each chapter has been written in a paper format. As of this date, they either have been accepted for publications or published in a professional journal or conference proceeding.

experimental geometry, acoustic, oceanographic, and seismic measurements are first described and analyzed. A parameterized environmental model is proposed to describe the experimental region. Then the inversion procedure based on MF processing using low-frequency data (195, 295, and 395 Hz) is applied to estimate the model parameters. The quality of the inversion results are gauged by two different approaches. First, the best-fit model is confirmed by continuous source localization over a period of time. Second, a comparison of the uncertainties of the parameter estimation provided by the Bayesian procedure with those obtained by separate inversions at many different ranges (a frequentist approach) is made and analyzed [46].

In Chapter 3, the analysis is extended from low-frequency to include mid-frequency data (805, 850, and 905 Hz) in the inversion procedure. First, a test run of mid-frequency MF source localization is carried out using the best-fit model derived from lower frequency data. Motivated by the increased ambiguity in the estimated source position, a refined estimate of the environmental model is obtained by incorporating the mid-frequency data in the inversion. The quality of the refined model is again confirmed by continuous source localization over the same period of time as in the low frequency data case [45].

Chapter 4 addresses the issue of uncertainty estimation using the Bayesian statistical treatment. The uncertainty of each estimated parameter is quantified by the variance associated with it, and analysis is then carried out by several methods based upon both the full and the empirical Bayesian approaches [44].

In Chapter 5, *a posteriori* analysis is undertaken using the inverse solution as an intermediate step to estimate TL. TL is estimated by first solving for an ensemble of relevant environmental model parameters and then using this ensemble to map into the TL domain. The probability distribution of TL is presented along with its statistical properties such as median and lower/upper percentiles [37].

Finally, Chapter 6 addresses the conclusions of the thesis and suggestions for future research.

Chapter 2

Geoacoustic Inversion of Low-Frequency Data

Geoacoustic inversion results based on data obtained during the Asian Seas International Acoustics Experiment (ASIAEX) 2001 East China Sea experiment are presented. The inversion process uses a genetic-algorithm-based matched-field-processing approach to optimize the search procedure for the unknown parameters. Inversion results include both geometric and geoacoustic variables. To gauge the quality of the inversion, two different analyses are employed. First, the inversion results based upon discrete source-receiver ranges are confirmed by continuous source localization over an interval of time. Secondly, separate inversions at many different ranges are carried out and the uncertainties of the parameter estimation are analyzed. The analysis shows that both methods yield consistent results, ensuring the reliability of inversion in this study.[‡]

2.1 Introduction

Probing geoacoustic properties indirectly from acoustic sound fields in an oceanic environment is an important application of underwater sound and has attracted the attention of several authors in recent years [35, 40, 42, 75]. Many studies have shown that even though the inversion results may present some degree of uncertainty, the techniques

---

[‡] The contents of this chapter are adapted from the paper entitled "Matched field geoacoustic inversion of low frequency source tow data from the ASIAEX East China Sea experiment" by Chen-Fen Huang and William S. Hodgkiss, *IEEE Journal of Oceanic Engineering*, Vol. 29, 952–963, 2004.

still prove to be an efficient and promising way to estimate environmental variables, particularly for those that are difficult to measure directly on site.

The purpose of this chapter is to present the geoacoustic inversion results based upon source tow data obtained during the Asian Seas International Acoustics Experiment (ASIAEX) 2001 East China Sea experiment. The experimental site, as depicted in the upper panel of Fig. 2.1, is in the East China Sea, and is located roughly at 500 km off the coast of the Zhejiang Province in east China. The thick curve in the figure illustrates the ship track of R/V *Melville* from Julian day (JD) 149 to 162 of 2001.

During the experiment, both acoustic and oceanographic data were collected. These data are analyzed to invert for the geoacoustic properties of the waveguide. In this analysis, matched-field (MF) inversion techniques are applied to estimate the environmental parameters. The basic principle of the MF inversion technique is to estimate the unknown parameters by minimizing an objective function that quantifies the mismatch between measured acoustic fields and simulated replica fields derived from an acoustic propagation model in a parameterized environment. The best estimates for the unknown parameters then correspond to the lowest mismatch. Since the dimension of the search space depends upon the number of unknown parameters which sometimes may be large, an efficient algorithm is needed to optimize the global search procedure. In this regard, a few methods geared to global optimization, such as simulated annealing and genetic algorithms, have been developed [18,19,25,27,32]. Furthermore, in the past decade, several authors, e.g., [34,73,80], have implemented inversion procedures in terms of computational software. Among others, the genetic-algorithm-based software SAGA developed by Gerstoft [34] has been widely applied and is used in this analysis along with the normal-mode propagation model SNAP [52] for a range-independent environment.

To ensure the robustness of the inversion, two different analyses were employed and both have yielded consistent results. The chapter is organized as follows: Sections 2.2 and 2.3 provide, respectively, the descriptions of the data acquisition and the data processing. Section 2.4 outlines the MF inversion procedure, and Section 2.5 presents the inversion results, followed by a conclusion in Section 2.6.

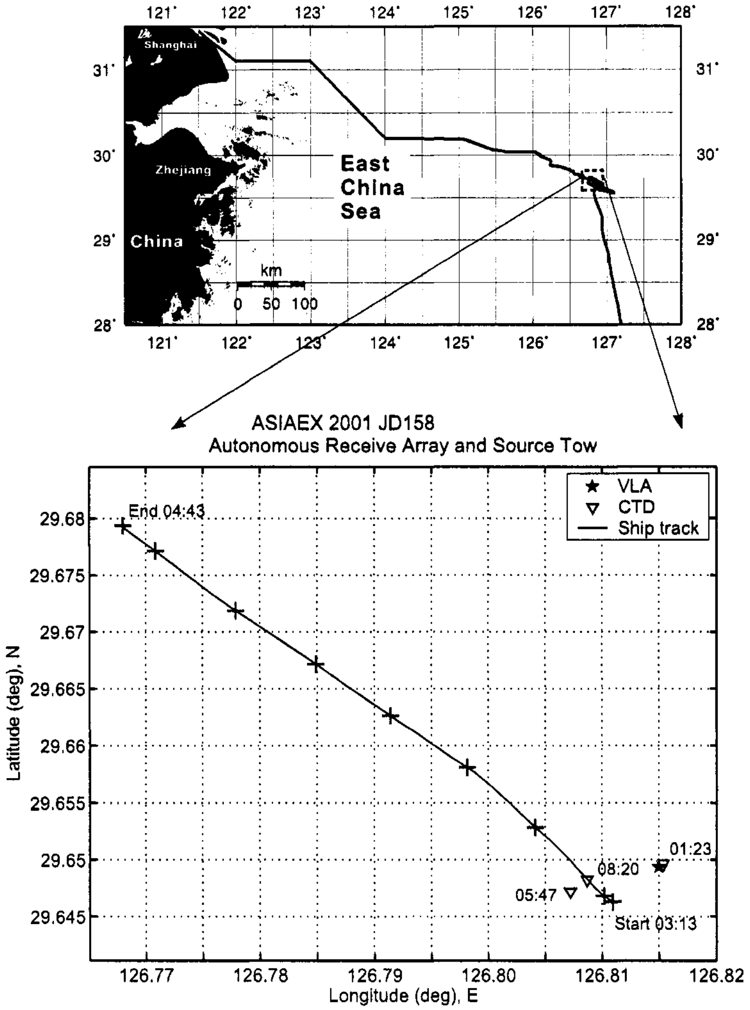

Figure 2.1: Plan view of the ASIAEX 2001 East China Sea experiment. Upper panel: the thick line illustrates the track of R/V *Melville* during the Julian days (JD) 149 – 162. Lower panel: the line is the ship track where the source energy was transmitted, and the plus signs mark 10-minute intervals starting from the acoustic measurement. The triangle signs represent the locations where the CTD measurements were taken. The star sign indicates the location of the vertical line array (VLA). All times are in Coordinated Universal Time (UTC).

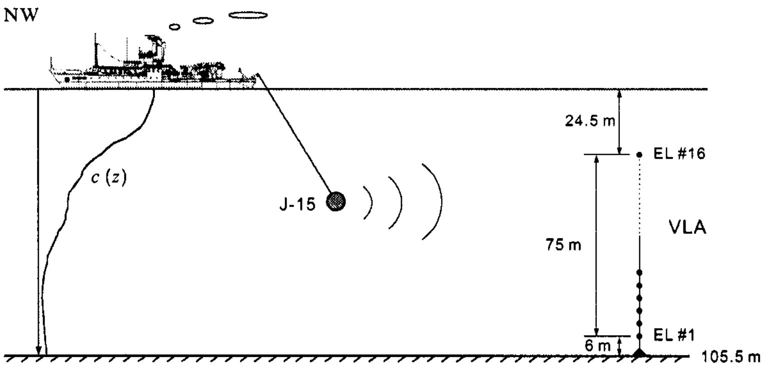

Figure 2.2: Side view of the experimental geometry.

2.2 Data Acquisition

In the following subsections, a few details of the experiment as well as the characteristics of the acquired data are described. These include experimental geometry, oceanographic and seismic measurements.

2.2.1 Experimental Geometry

The map of the region where the acoustic and oceanographic measurements were taken is shown in the lower panel of Fig. 2.1. On JD 158, acoustic energy was transmitted from the J-15 source towed near 47 m depth by R/V *Melville* with a speed of about 3 knots. The ship track is indicated by the line in the figure, on which the distances between the source and the receiver range from 0.5 to 6 km. The experimental geometry is illustrated schematically in Fig. 2.2. A 16-element, 75-m aperture, autonomous recording vertical line array (VLA) was moored up from the seafloor at location 29°38.927′ N, 126°48.892′ E where the measured water depth was approximately 105.5 m. The lowermost element (element #1) was approximately 6 m above the bottom; Element #4 failed during deployment.

Continuous-wave (CW) tonals at 95, 195, 295, 395, 805, 850, and 905 Hz were transmitted and the sound field was recorded from 0313 to 0443 Coordinated Universal Time (UTC). In this study, only the low frequency data at 95, 195, 295, and 395 Hz are employed for inversion analysis.

2.2.2 Oceanographic Measurements

The current profile in the water column from 30 to 100 m was measured by a ship-mounted ADCP system on board R/V *Melville.* The ADCP measurement from JD 158 to 158.25 is shown in Fig. 2.3. The upper and lower panels illustrate, respectively, time-series plots of current speed and current vector stick at different depths. The time window of the acoustic transmissions is indicated by the two white lines on the upper panel and the shaded area on the bottom. It is noted that there existed a strong eastward tidal current with magnitude greater than 0.5 m/s around the middle of the water column. This results in a tilt of the VLA.

The sound-speed profile in the water column was measured by CTD. Three measured sound-speed profiles on JD 158 are shown in Fig. 2.4, on which the times when the measurements were taken are labeled. CTD0123 (solid line) was the profile when the VLA was deployed; CTD0547 (dashed line) and CTD0820 (dashed-dotted line) were the profiles measured roughly 1 and 4 hours after the acoustic tonals were transmitted, respectively.

The locations of CTD measurements are indicated in the lower panel of Fig. 2.1. These sound-speed profiles show that higher sound speed near the surface and, in the thermocline layer, time-evolving sound speed fluctuations were observed, while below 75 m the sound speed remained the same. Note that for a sound source at about 47 m as in the present case, the sound speed structure will result in a downward-refracting propagation pattern, so that strong interactions of the sound fields with the seafloor might be expected.

2.2.3 Seismic Measurements

Geoacoustic ground truth measurements of the region covered by 28° – 30°N and 126°30′ – 128°E were made in 2000 and 2001 as part of the ASIAEX East China Sea field program. The surveys include gravity and piston cores and water-gun and chirp sonar generated subbottom profiles. The detailed discussion on geoacoustic measurements are presented in Miller *et al.* [67]. In short, these data suggest that the sedimentary bottom presents a layered structure. The thickness of the upper layer from seafloor to Transgressive Systems Tract (TST) is about 0 to 2 m, and that of the lower

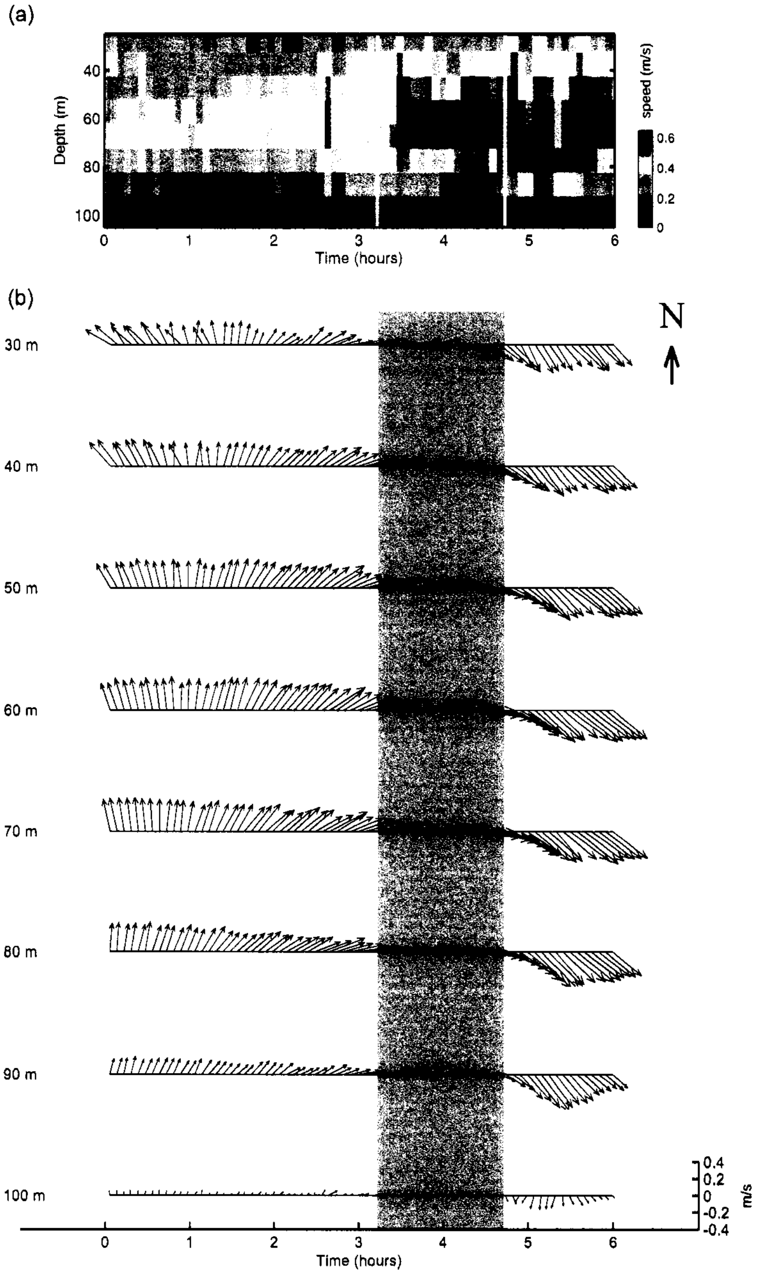

Figure 2.3: Time-series plots of current speed (upper panel) and current vector stick (bottom panel) at different depths from JD 158 to 158.25. The time windows of the acoustic transmissions are indicated by the two white lines on the upper panel and the shaded area on the bottom.

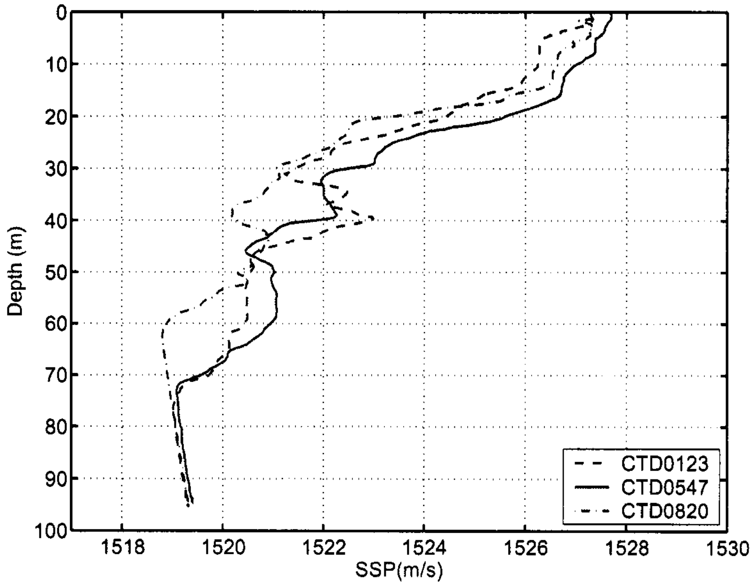

Figure 2.4: Measured sound-speed profiles by the CTDs on JD 158. Each sound-speed profile is labeled by the time when the measurement was taken. The locations of the CTD measurements are indicated in Fig. 2.1.

layer from TST to Sequence Boundary (SB) is about 5 to 7 m at the site of towed source propagation experiments. Moreover, the sediment coring analysis indicates this region spanned a surficial sediment "front" consisting of mud-and-sand type of sediment to the west and sand to the east. The acoustic experimental site was located to the west of the front; a mean grain size (in phi scale) of 4.3 ϕ consistent with mud-and-sand-like sediment. The coring data also show a sound speed going from approximately 1575 m/s at the water-sediment interface to 1600–1675 m/s at approximately 1 m into the sediment.

2.3 Data Processing

The entire 90-minute time series data were processed using 262,144-point FFTs with 50% overlap. With a sampling rate of 20470.8 samples/sec (the bin width is 0.0781 Hz), the time duration of each FFT (snapshot) is 12.805 sec and the interval between consecutive snapshots is 6.40 sec. The long length of the snapshot is to ensure high signal-to-noise ratio (SNR). Due to the narrow bin width and the Doppler shift resulting from ship motion, the frequency bin selected for the inversion needs to be chosen with care. For each snapshot and frequency, the bin chosen corresponds to the bin containing the highest average power across the array. Since there are 15 functioning array elements, there are 15 complex pressure values sampling the acoustic field across the water column for each snapshot. Figure 2.5 shows the calibrated time-evolving signal power across the array for 95, 195, 295, and 395 Hz, and the corresponding noise floor which is estimated by averaging over the 15 adjacent bins separated from the signal bin by 5 bins. In this figure, the vertical axis is the element number with element #1 being the deepest transducer. Note that at 95 Hz the SNR is very low and this frequency is not used in the inversion. In contrast, the SNR is high for the frequencies 195, 295, and 395 Hz.

The estimated normalized cross-spectral density matrix (CSDM), $\widehat{\mathbf{R}}$, for a signal frequency is given by

$$\widehat{\mathbf{R}} = \frac{\langle \mathbf{d}\mathbf{d}^{\dagger} \rangle}{\mathrm{Tr}\left[\langle \mathbf{d}\mathbf{d}^{\dagger} \rangle\right]}, \tag{2.1}$$

where $\mathbf{d}$ is the vector containing the measured complex pressures, and $\langle \cdot \rangle$ and $\dagger$ denote, respectively, the average over several snapshots and the complex transpose operation. The covariance matrix is normalized by its trace. The maximum obtainable Bartlett

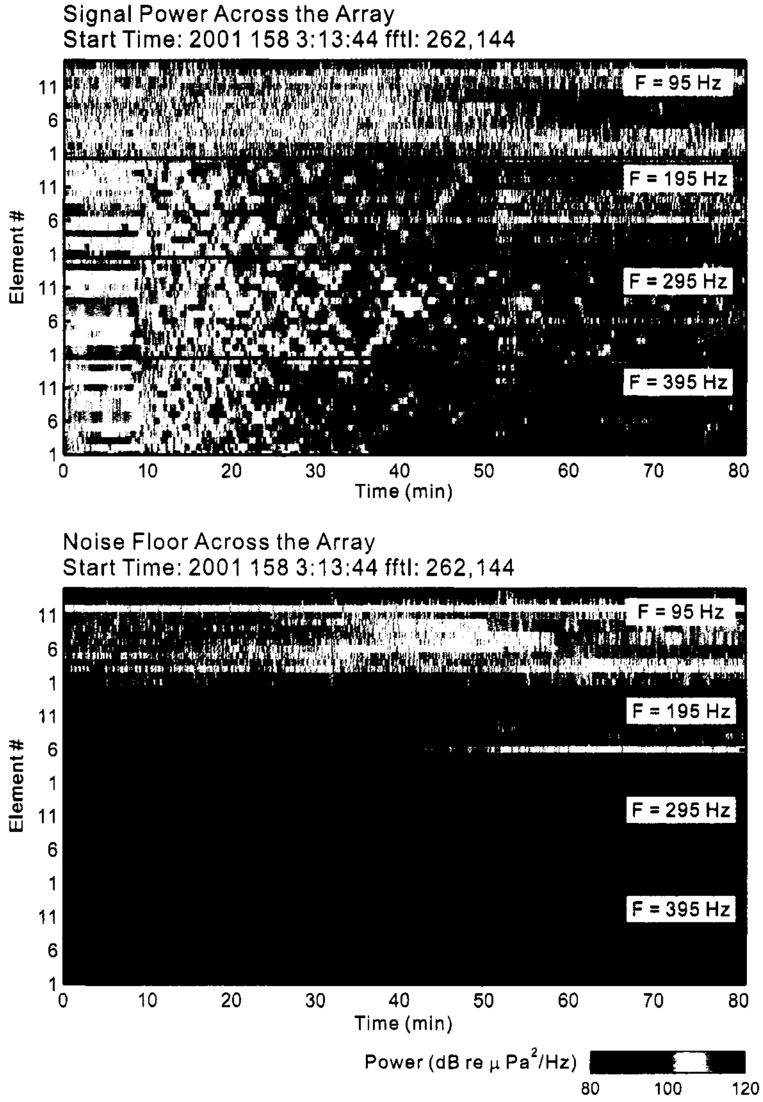

Figure 2.5: Time-evolving signal power (upper panel) and noise floor (lower panel) across the elements for 95, 195, 295, and 395 Hz.

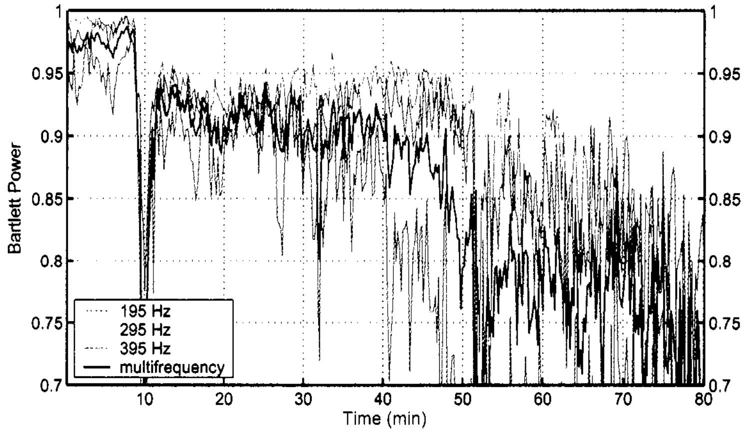

Figure 2.6: Maximum obtainable Bartlett power versus time: the thin lines are for the frequencies 195, 295, 395 Hz, and the thick line is the Bartlett power averaged over all three frequencies.

power from the MF inversion is defined as

$$P_{\mathrm{BT,\ max}} = \max\ \mathrm{EIV}[\widehat{\mathbf{R}}], \tag{2.2}$$

where EIV denotes the eigenvalues of the matrix. Due to noise contamination in the data, the value of $P_{\mathrm{BT,\ max}}$ must be less than one. In the following analysis, we shall use this value as a measure of SNR.

Under the assumption of statistical stationarity, each value of CSDM was estimated from 4 snapshots which span a time interval of 32 sec and cover about 48 m in source range. Figure 2.6 shows $P_{\mathrm{BT,\ max}}$ as a function of time on a linear scale for each single frequency 195, 295, and 395 Hz (thin lines), as well as for all three frequencies (thick line) for which the power is defined as the average of $P_{\mathrm{BT,\ max}}$ over the three frequencies. During the first 10 minutes of the acoustic transmissions, the ship was stationary and high values of $P_{\mathrm{BT,\ max}}$ are seen in the figure. As the ship began to move away from the VLA, the SNR decreased resulting in the values of $P_{\mathrm{BT,\ max}}$ being lower.

2.4 Matched-Field Geoacoustic Inversion

In this section, the procedure and the required components for the MF geoacoustic inversion are addressed. To prepare for the inversion, an acoustic propagation model and a parameterized environmental model must be chosen. An appropriate objective function and an optimization algorithm must also be defined or selected. The sensitivity of the objective function with respect to environmental variability needs to be tested and the quality of the inversion should be measured.

2.4.1 Acoustic Propagation Model

For ranges greater than several water depths, the acoustic pressure field may be expressed as a finite sum of normal modes. A general bathymetric and geological survey has indicated that in the neighborhood of the experimental site the environment is nearly range-independent. Therefore, the acoustic pressure at a depth z and range r produced by a time-harmonic $\mathrm{e}^{-i\omega t}$ point source at depth z_s in an environment with arbitrary sound speed distribution may be expressed as [53]

$$p(r,z) = \frac{i\mathrm{e}^{-i\pi/4}}{\rho(z_s)\sqrt{8\pi r}} \sum_{n=1}^{N} \Psi_n(z_s)\Psi_n(z)\frac{\mathrm{e}^{ik_{rn}r}}{\sqrt{k_{rn}}} \tag{2.3}$$

where Ψ_n is the n-th normal mode corresponding to the horizontal wavenumber, k_{rn}. The calculations of the modeled acoustic pressure fields were performed by the SACLANTCEN Normal-mode Acoustic Propagation program (SNAP) [52].

2.4.2 Environmental and Array Parameterizations

As mentioned previously, the experimental area is characterized by a fairly flat bottom. The environment is modeled as a waveguide with a constant water depth over a two-layered seafloor as shown schematically in Fig. 2.7. The water depth is known to be approximately 105.5 m. The seafloor is modeled as a uniform sediment layer with sound speed c_{sed}, density ρ_{sed}, attenuation α_{sed}, and thickness d, overlying a semi-infinite subbottom. The sound speeds in these two layers are related by

$$c_{\text{sub}} = c_{\text{sed}} + \Delta c \tag{2.4}$$

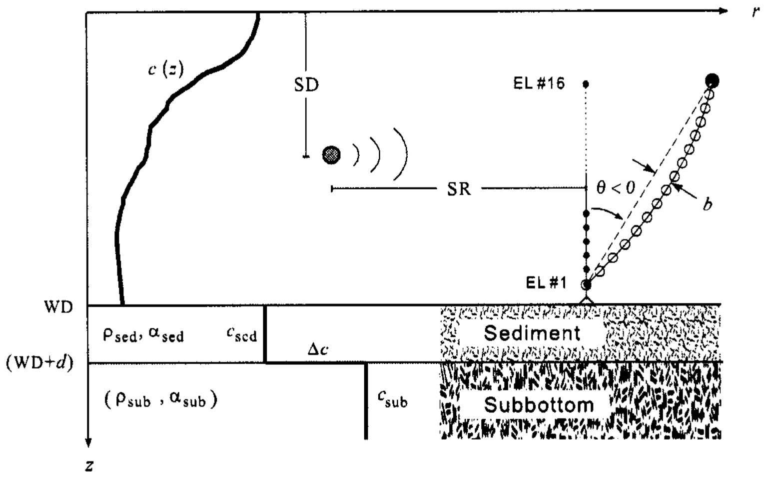

Figure 2.7: Geoacoustic model and experimental configuration for the ASIAEX 2001 East China Sea experiment. Thick lines indicate schematically the sound speed distribution in the water and in the bottom. For the nomenclature, see Table 2.2.

where Δc is the sound speed difference between the two layers and is a positive value. The above-mentioned unknown parameters are estimated in the inversion along with the water depth (although it is known from direct measurement). As for the density and attenuation of the subbottom, separate simulations suggest that the inversion result is relatively insensitive to these parameter values. Therefore, rather than inverting for them, they were set at nominal values of density 2.4 g/cm^3 and attenuation 0.01 dB/λ.

For optimal array-processing, it is necessary to determine the relative positions of the sensors. To achieve a loss of less than 1 dB in conventional array-processing gain requires that the element positions be prior known within a distance of $\lambda/10$, where λ is the wavelength at the frequency of interest [43]. Due to the effects of a nonuniformly-distributed tidal current over the water column as indicated in Section 2.2.2, the VLA might be tilted and curved. To account for the array curvature, a parabolic VLA shape is assumed and the geometry of the VLA is specified in terms of the bow b at the mid-point of the array as shown in Fig. 2.7 and the length of the undisturbed straight array L_s. Note that the value of L_s is known and equals 75 m. According to this geometry, the location of each array element (assuming $\theta = 0$) becomes

$$(x_\mathrm{p}, z_\mathrm{p}) = \left(\frac{4b}{L_\mathrm{s}^2} (L_\mathrm{s} - z_\mathrm{s}) z_\mathrm{s},\ \left(1 - \frac{8}{3}\frac{b^2}{L_\mathrm{s}^2}\right) z_\mathrm{s} \right) \tag{2.5}$$

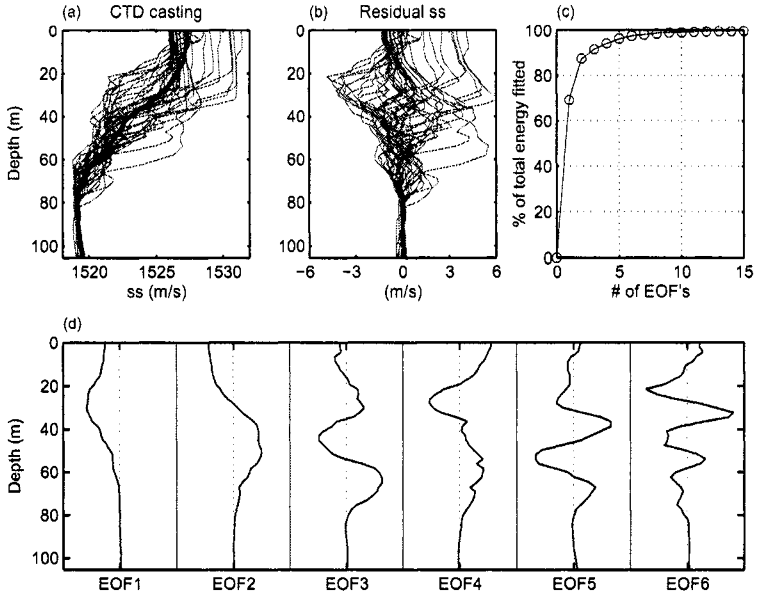

Figure 2.8: Empirical Orthogonal Function (EOF) analysis for the 2001 ASIAEX CTD casts. (a) sound-speed profiles measured from R/V *Melville* and the average sound-speed profile (thick black line); (b) Residual sound-speed profiles; (c) Percent of total fit energy with limited sets of EOF's; (d) First 6 EOF's.

where the subscripts s and p denote the straight and the parabolic arrays, respectively. Then, the tilt of the array is determined by the angle θ. A negative value of θ indicates the array is tilting away from the source. (A 1° tilt corresponds to a approximately 1.3-m horizontal displacement at the topmost array element.)

Because the sound speed difference in the thermocline layer was significant between CTD0123 and CTD0547, an Empirical Orthogonal Function (EOF) analysis of the sound speed measurements [58] was carried out. Figure 2.8 summarizes the EOF analysis for the sound-speed profile measurements. Figure 2.8(a) shows the ensemble of CTD casts from JD 149 to 162 and the average sound-speed profile (thick line); Fig. 2.8(b) shows the variations of residual sound-speed profiles; Fig. 2.8(c) shows the percent of total fit energy, i.e., eigenvalues, within the first 15 EOF's; the shape of the first 6 empirical orthogonal functions is shown in Fig. 2.8(d). It shows that the first 4 EOF's contain about 95 % of the energy.

Table 2.1: The EOF Coefficients for the Measured Sound-Speed Profiles Listed on Fig. 2.4.

Measured SSP	EOF 1	EOF 2	EOF 3	EOF 4	EOF 5	EOF 6
CTD0123	9.39	−0.63	−0.80	1.97	2.20	−0.27
CTD0547	6.77	−2.50	0.52	2.79	0.03	−0.28
CTD0820	11.95	−4.04	−2.73	1.45	0.21	0.68

EOF i denotes the i-th EOF coefficient.

Table 2.1 shows the EOF coefficients for three CTD's taken on JD 158. The search bounds in the estimate of the ocean sound-speed profile are based on this table. The ocean sound-speed profile is modeled by the first three EOF's with CTD0547 as the baseline model.

The forward model parameters can be divided into three subsets: geometrical, geoacoustic and ocean sound speed parameters. Table 2.2 lists each inversion parameter along with their search bounds. These values were selected based upon *a priori* knowledge about the environment.

2.4.3 Objective Function

The objective function measures the discrepancy between the measured acoustic field and replica fields calculated for likely values of the unknown parameters. The data misfit objective function chosen here is based on the incoherent multi-frequency Bartlett processor [63]. Under the assumption of no spatial coherence across frequencies, the misfit objective function can be expressed as

$$\begin{aligned} \phi(\mathbf{m}) &= \frac{1}{L}\sum_{l=1}^{L}\left[1 - \mathbf{d}_l^{\dagger}(\mathbf{m})\widehat{\mathbf{R}}_l\mathbf{d}_l(\mathbf{m})\right] && (2.6)\\ &= 1 - \frac{1}{L}\sum_{l=1}^{L} P_{\mathrm{BT},l}(\mathbf{m}) && (2.7)\end{aligned}$$

where $\mathbf{d}(\mathbf{m})$ is the replica field generated for the vector of unknown parameters $\mathbf{m}$, normalized to have unit length, $\widehat{\mathbf{R}}$ is an estimated CSDM as given in Eq. (2.1), and L is the number of source frequencies. The misfit objective function can be re-written

Table 2.2: Inversion Parameters with Search Bounds

Model parameter		Search bounds	
Description	Symbol	Lower	Upper
Geometrical			
Source range (m)	SR	1650	1800
Source depth (m)	SD	46	51
Water depth (m)	WD	104	108
Bow of parabola (m)	b	0.5	2
Array tilt (deg)	θ	-7	-5
Geoacoustic			
Sediment			
Comp. speed (m/s)	c_{sed}	1550	1650
Attenuation (dB/λ)	α_{sed}	0.01	0.5
Density (g/cm^3)	ρ_{sed}	1.3	2.2
Subbottom			
Increase comp. speed (m/s)	Δc	10	200
Depth of subbottom (m)	d	1	20
Ocean sound speed			
EOF 1		5	10
EOF 2		-5	0
EOF 3		-3	3

The search interval for each parameter was discretized into 128 points.

The array tilt refers to the angle with respect to the vertical axis. (negative in the direction away from the source).

as a function of the Bartlett power as shown in Eq. (2.7), in which the second term is the arithmetic mean of Bartlett powers over the selected frequencies. By minimizing the misfit objective function, the most likely values of the environmental parameters can be found.

2.4.4 Sensitivity Analysis

To investigate the relative importance of the parameters, a sensitivity study was carried out. Figure 2.9 summarizes the sound-field sensitivity for the selected frequencies 195, 295, and 395 Hz for the model parameters given in Table 2.2. The sensitivity of the Bartlett power for the given frequency and the given parameter was computed by correlating the data vector generated by the "true" parameter value with replica vectors computed by varying the parameter value. In each case, the parameters that are not varied are held at their nominal values (the values taken from the best-fit model at T = 29 min) and the search bounds of each parameter were as shown in Table 2.2. A sensitivity index (SI) for a particular parameter m_i is obtained by incorporating the minimum point in the sensitivity curve, $P_{\mathrm{BT}}(m_i')/P_{\mathrm{BT}}(m_i)$, in the following expression:

$$\mathrm{SI}\ (m_i) = 1 - \min_{l_i \le m_i' \le u_i} P_{\mathrm{BT}}(m_i')/P_{\mathrm{BT}}(m_i) \tag{2.8}$$

where m_i' denotes the values taken from the search interval between the lower bound l_i and the upper bound u_i. $P_{\mathrm{BT}}(m_i)$ is always one due to no noise in the simulation. For highly sensitive parameters, SI is almost one which means that the correlation degrades rapidly as the parameter value departs from the "true" value. For less sensitive or the so-called non-identifiable parameters, the correlation remains about the same even with some changes in such parameters. Note that the value of SI for each parameter is also dependent on the corresponding search bounds. However, this measure of sensitivity is useful for inter-frequency comparison.

2.4.5 Genetic Algorithms

Genetic algorithms (GA's) are robust search mechanisms based on underlying genetic biological principles. The complete description is well documented in [34]. The values of the GA parameters used in this analysis are as follows: the population size was

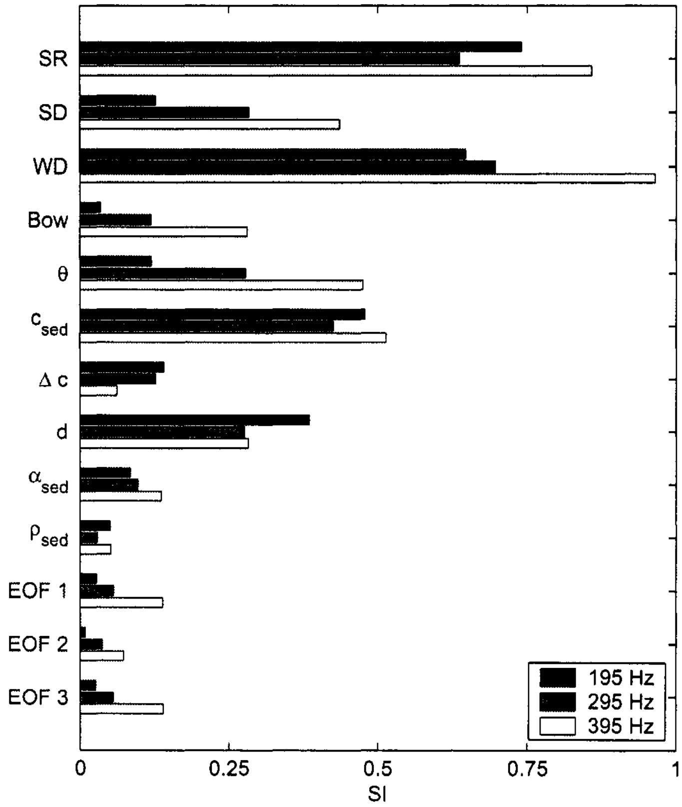

Figure 2.9: The sensitivity index for the model parameters given in Table 2.2 .

set to 64, reproduction size was 0.5, crossover probability was 0.8, mutation probability was 0.05, and number of forward model computations for each population was 2500. However, to collect statistical information in order to estimate the parameter uncertainty, the number of parallel populations was set to 45. Approximately 112,500 forward models were run.

2.4.6 Uncertainty Estimates

Because of the ambiguity imposed by data incompleteness, measurement noise, and theoretical simplifications of the environment, a range of model parameters may explain the data equally well. The global optimization method in SAGA is used to obtain the samples of the search space. To estimate the parameter uncertainty, the obtained samples are then used to calculate the posterior probability density (PPD) as follows [76]:

$$P(\mathbf{m}) = \frac{\mathcal{L}(\mathbf{m})}{\sum_{j=1}^{N_{\mathrm{obs}}} \mathcal{L}(\mathbf{m}^j)} \tag{2.9}$$

where N_{obs} is the total number of observations (forward model runs). Under the assumption of Gaussian errors, the likelihood function $\mathcal{L}(\mathbf{m})$ is related to the objective function $\phi(\mathbf{m})$ through an exponential $\mathcal{L}(\mathbf{m}) \propto \exp(-\phi(\mathbf{m}))$. From the PPD, the mean model parameter $\langle \mathbf{m} \rangle$ and the model covariance matrix $\mathrm{Cov}(\mathbf{m})$ can be estimated, respectively, as follows:

$$\begin{aligned} \langle \mathbf{m} \rangle &= \sum \mathbf{m} P(\mathbf{m}) && (2.10) \\ \mathrm{Cov}(\mathbf{m}) &= \sum \mathbf{m}\mathbf{m}^{\mathrm{T}} P(\mathbf{m}) - \langle \mathbf{m} \rangle \langle \mathbf{m} \rangle^{\mathrm{T}} && (2.11) \end{aligned}$$

where T denotes the transpose operation, and the sum is taken over the total observations. A measure of the accuracy of the inversion is defined as standard deviations of the model parameters computed by the square roots of the diagonal terms of $\mathrm{Cov}(\mathbf{m})$.

2.5 Results and Discussion

Matched-field geoacoustic inversion using the selected frequencies 195, 295, and 395 Hz was carried out at T = 29 min over a parameter space of 13 parameters including the geometrical, geoacoustic, and ocean sound speed EOF coefficients. Based upon the GPS measurement on R/V *Melville*, the source was approximately 1.7 km away from the VLA. Figure 2.10 shows the marginal dot diagrams for the model parameters. The vertical axis is the achieved misfit (i.e., Eq. (2.7)) with respect to the parameter sampled during the SAGA optimization. The thick line superimposed on each scatter plot was obtained by using the best-fit model corresponding to the optimal value of the objective function as a baseline and computing the sensitivity for the optimized parameter. We see that the sampled values for the array bow and tilt parameters (b and θ) are spread mainly inside the sensitivity curve and align mostly with the best-fit values. A similar behavior is observed for the ocean sound speed EOF coefficients but with a wider span. The consistency between the local (line) and global (dots) searches shows that this set of parameters is weakly correlated with the other parameters. For the geoacoustic parameters, most sampled values wander outside the curve. This reveals the more complicated structure in the multi-dimensional search space. Note that the sampled values for the source range (SR) and the water depth (WD) are spread uniformly throughout the range of the parameter interval. This is due to the strong coupling between these two parameters.

Parameter coupling is another factor that determines the degree of uncertainty in the model parameter estimates. Figure 2.11 shows the two-dimensional cross-sections of Bartlett power for the selected parameters. The colorbar next to each plot indicates the dynamic range in terms of dB. The two-dimensional dependence of Bartlett power on SR and WD (Fig. 2.11(a)) exhibits a long narrow ridge indicating a strong correlation between these two parameters. Similar correlations between c_{sed} and WD, and c_{sed} and d are illustrated in Figs. 2.11(c) and (d), respectively. In each case, similar Bartlett power would be achieved with increases in both parameters. As a result, high values of one parameter tend to occur consistently with high values of the other parameter during the SAGA optimization. Physically, the positive correlation between the water depth (WD) and the source range (SR) can be explained by the waveguide invariant [26].

The SAGA-determined best-fit parameters and the mean estimated from the PPD along with their standard deviations are tabulated in Table 2.3. Note that $\text{SAGA}_{\text{best}}$ and $\text{SAGA}_{\text{mean}}$ estimated model parameters are not necessarily equal. This is due to the nonlinear relation between the data and the model parameters, a data set with a

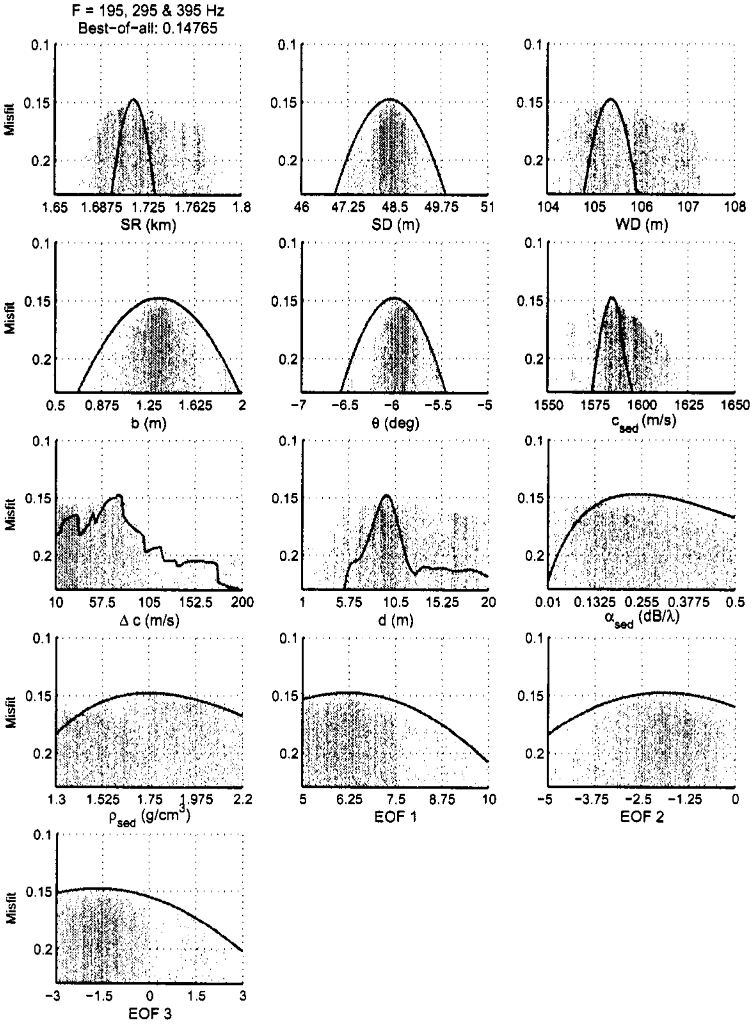

Figure 2.10: Marginal dot diagrams of the SAGA search for the model parameters. The vertical axis represents the attained misfit on a linear scale. The thick line is the sensitivity curve of the multi-frequency misfit function using the best-fit model as a baseline.

Table 2.3: Parameter Estimates at SR = 1.7 km

Parameter		$\text{SAGA}_{\text{best}}$	$\text{SAGA}_{\text{mean}} \pm \sigma$
SR	(m)	1714	1714 ± 16
SD	(m)	48.3	48.4 ± 0.2
WD	(m)	105.4	105.4 ± 0.6
b	(m)	1.3	1.3 ± 0.1
θ	(deg)	-6.02	-6.02 ± 0.08
c_{sed}	(m/s)	1585	1588 ± 7
Δc	(m/s)	74	43 ± 24
d	(m)	10	10 ± 3
α_{sed}	(dB/λ)	0.28	0.2 ± 0.1
ρ_{sed}	(g/cm^3)	1.8	1.8 ± 0.2
EOF 1		6.3	6.1 ± 0.6
EOF 2		-2.2	-2.0 ± 0.6
EOF 3		-1.6	-1.7 ± 0.7

σ indicates the standard deviation.

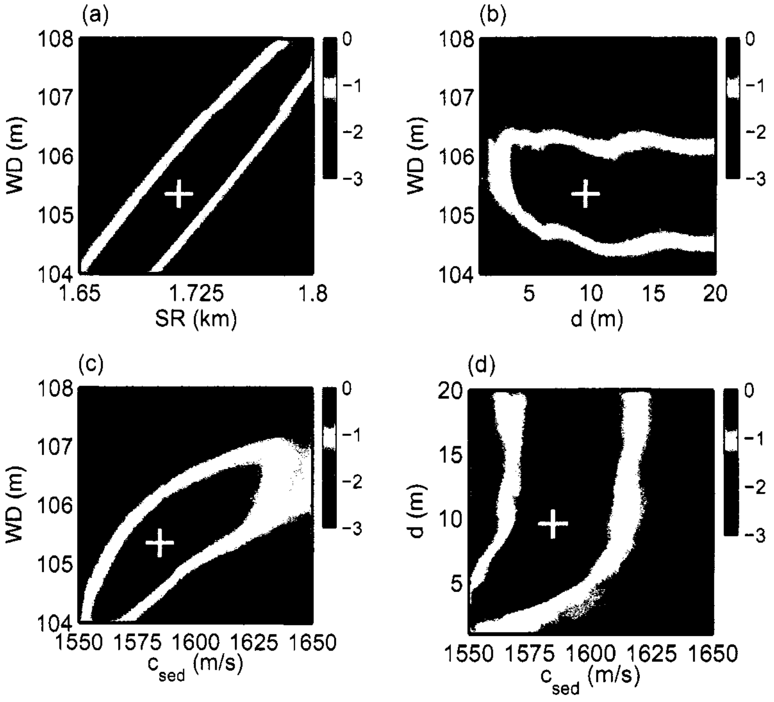

Figure 2.11: Two-dimensional cross-sections of Bartlett power for the selected model parameter estimated at SR = 1.7 km. The plus signs indicate the true parameter values taken from the SAGA best-fit model. (synthetic cases)

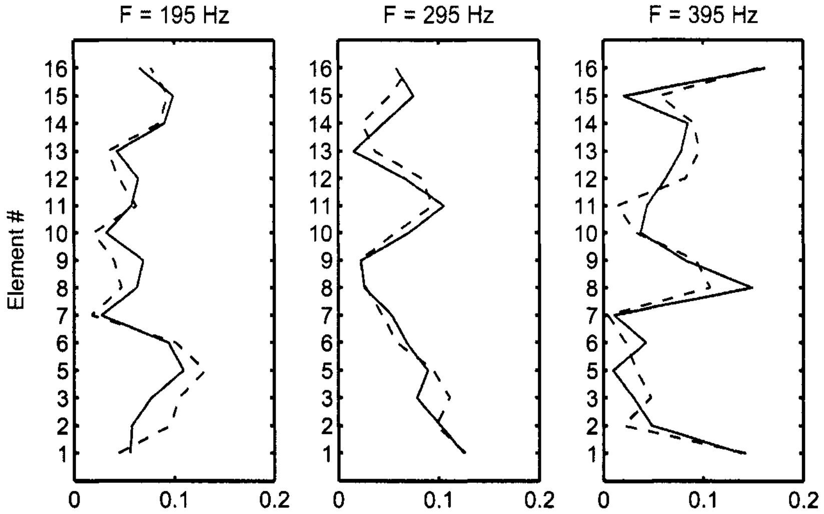

Figure 2.12: Comparison of the observed and modeled fields on the vertical array for each of the frequencies used in the inversion. The solid and dashed lines indicate the magnitude of the observed and modeled fields, respectively. Note that element #4 has been deleted.

Gaussian error law in general is mapped onto a estimator of the model having a non-symmetric density function.

It shows that the geometrical parameters (SR, SD, WD, b, θ), sediment sound speed (c_{sed}), and the sediment thickness (d) all are well-determined. However, the parameter Δc isn't well-determined (the SAGA best-fit value is outside the mean plus one standard deviation). Although the sediment attenuation and density have low sensitivity, the standard deviation also is relatively small due to the narrow search bounds selected for these two parameters.

Figure 2.12 shows the comparison of the observed and modeled fields on the vertical array for each of the frequencies used in the inversion. The solid line represents the magnitude of the observed field normalized by the total power registered at VLA and the dashed line represents the magnitude of the modeled field computed by the best-fit model and similarly normalized. The comparison shows good agreement between the observed and modeled data for the frequencies 195, 295, and 395 Hz.

2.5.1 Source Localizations

The inversion quality also is checked by using MF processing for source localization. The replica pressure field computed by the best-fit model from the inversion carried out at SR = 1.7 km was used in this subsection. To avoid search grid mismatch in the frequency band of interest [56], the grid spacings Δr and Δz were set to be 10 m and 1 m, respectively. Figure 2.13 shows the source range-depth ambiguity surfaces for each source frequency and the multi-frequency average at SR = 1.7 km. The multi-frequency ambiguity surface is defined as the arithmetic mean of MF correlations over the selected frequencies. We see the distinguishing mainlobe/sidelobe structure and the high MF correlations for both single and multiple frequencies.

An environmental model that localizes the source at one range may not localize the source at another range. In order to confirm the applicability of the environmental model estimated at SR = 1.7 km, this model was also applied to the data from a greater range. Figure 2.14 shows the ambiguity surface at T = 42 min using the environmental parameters listed in Table 2.3. The grid spacing $(\Delta r, \Delta z)$ was the same as before. The results in Fig. 2.14 show that the peak on each ambiguity surface still remains at a high correlation level and the peak locations for the different frequencies are located at the same range/depth and agree with the experimental configuration.

Encouraged by the consistency of the geoacoustic model at two different ranges, we then applied this model on the acoustic data over the time interval from 20 to 50 minutes. First, an exhaustive search was conducted over three of the geometrical parameters (SR, SD and θ) at 295 Hz. Figure 2.15 shows the MF correlations over time for different array tilts. As mentioned in Section 2.4.2, the accuracy to which sensor positions should be known has to be better than $\lambda/10$. *A priori* information showed that the array was not purely vertical and it had some tilt on the order of -5 or -7 degrees from vertical. Due to the current force on the VLA, the source and the VLA are not in the same vertical plane in which the r-axis is defined by the source and the deepest array element. Therefore, from the perspective of the source, the apparent tilt of the array changes over time. In Fig. 2.15, the bow of the array was taken to be the estimated value from the inversion and θ varies from -5 to -7 degrees in 0.5 degree increments. The tilt is such that the uppermost part of the array is farther away from the source than the

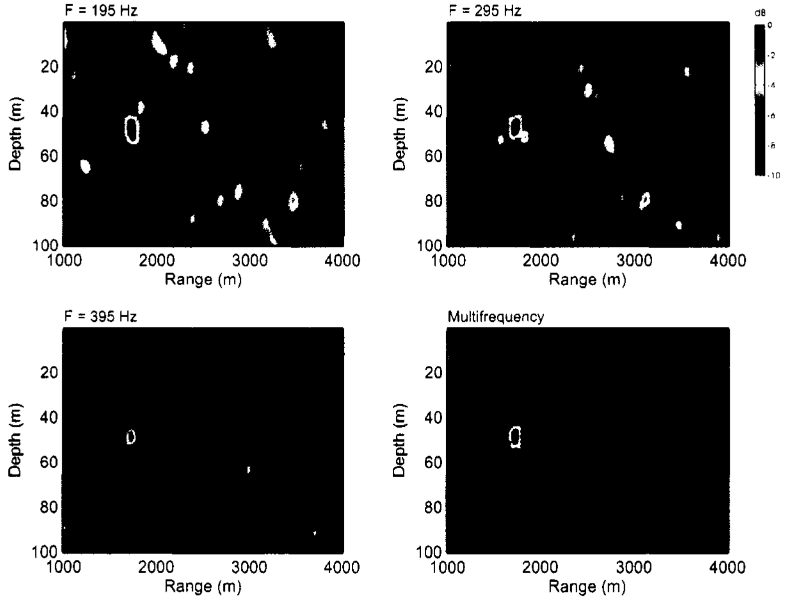

Figure 2.13: Range-depth ambiguity surfaces at SR = 1.7 km. The replica pressure field is computed using the environmental parameters listed in Table 2.3.

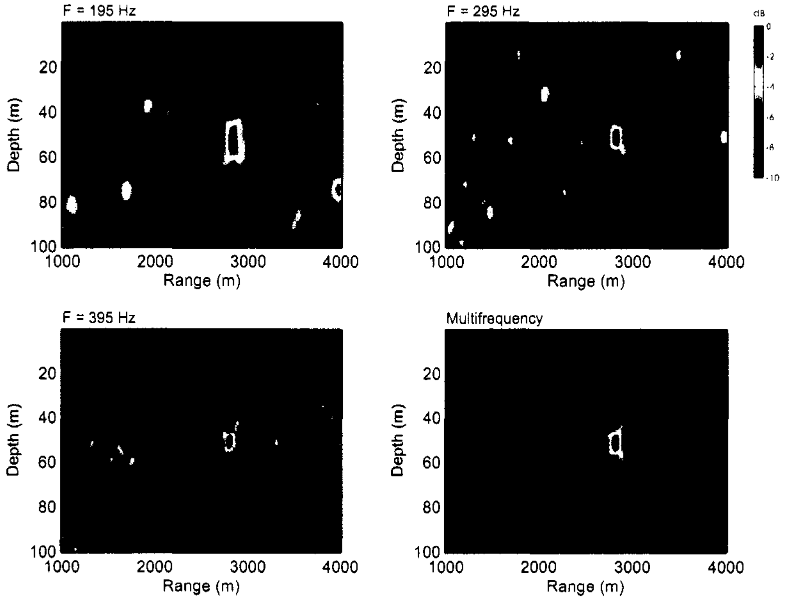

Figure 2.14: Range-depth ambiguity surfaces at SR = 2.8 km. The replica field is computed using the environmental parameters listed in Table 2.3.

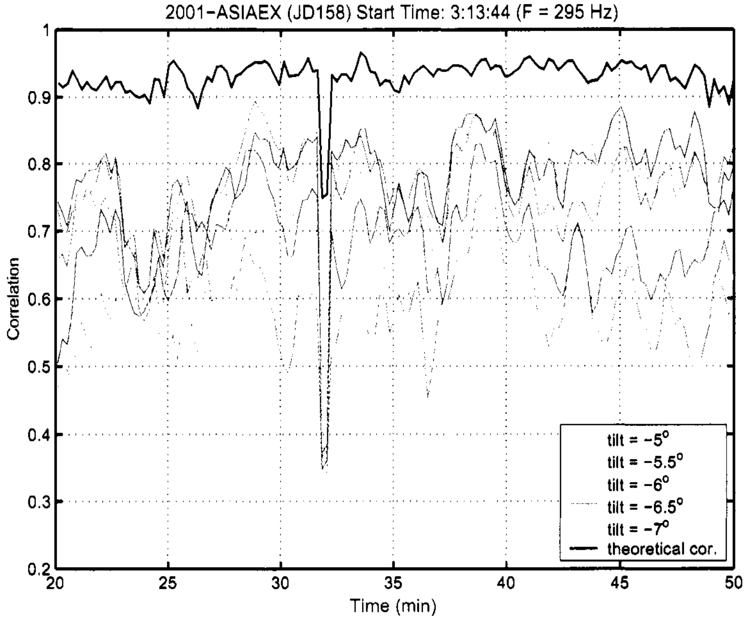

Figure 2.15: MF correlations over time for different array tilts at 295 Hz. The replica pressure field is computed using the environmental parameters listed in Table 2.3.

lower part of the array. As expected, the highest MF correlation appears at the range where the inversion was carried out.

MF-derived source-receiver range and source depth using 195, 295, and 395 Hz over the time interval from 20 to 50 minutes are displayed in Figs. 2.16 and 2.17, respectively. The peak tilt correlations shown in Fig. 2.15 were used as a guide for which tilts to use in this time period. Based upon the GPS measurements, the data in this time interval cover the range from 1 to 3.5 km. The source depths measured by the depth sensor are indicated by the plus signs in Fig. 2.17. Compared with the GPS and the depth sensor measurements, MF-derived source position is consistent with the experimental configuration. Source localization based on the best-fit model tracks the actual source positions well.

2.5.2 Inversion Results over Time

As a final example, separate inversions were carried out using the acoustic data at each range over the time interval from 20 to 40 minutes. The GA parameters and the

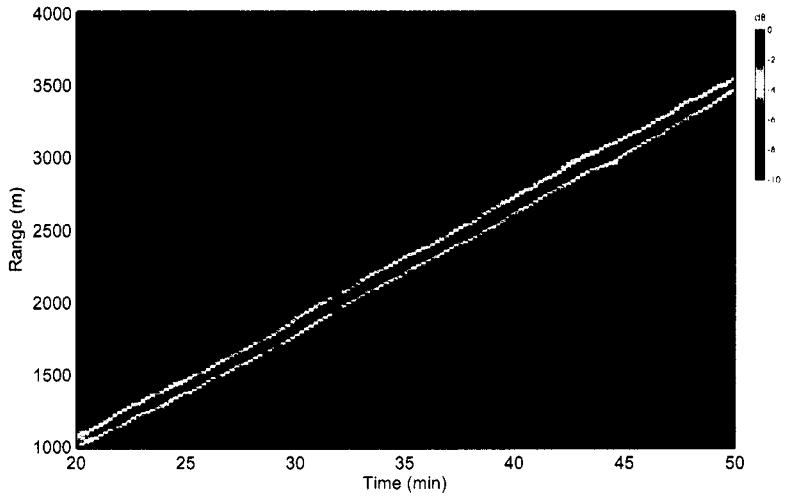

Figure 2.16: MF-derived source-receiver range over the time interval from 20 to 50 min.

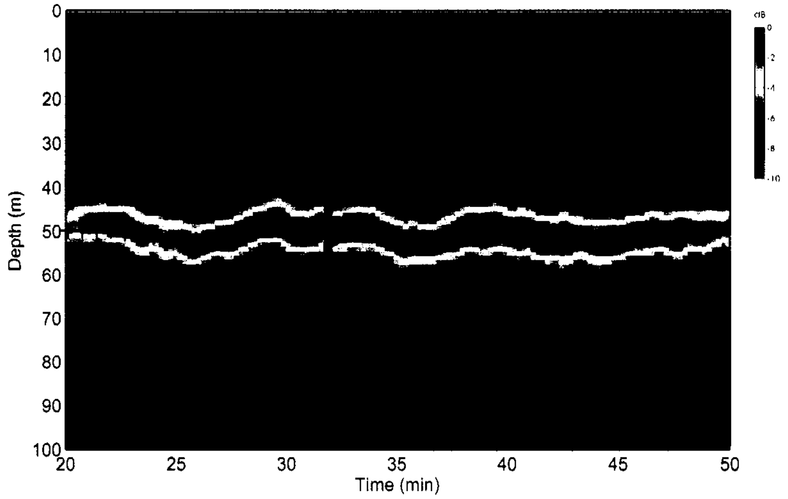

Figure 2.17: MF-derived source depth over the same time interval shown in Fig. 2.16. The plus signs indicate the true measured values.

search bounds were taken to be the same as the inversion conducted at T = 29 min except for SR. Approximately 10^7 forward models were computed for a total of 98 inversions.

The purpose of inverting the data at many ranges is to consider a large enough number of separate measurements to provide an indication of the consistency of the inversion results for the various model parameters. Figure 2.18 shows the lowest misfit objective function and the corresponding model parameters (best-fit model) determined in all inversions plotted as a function of time.

The best-fit model at each range was obtained by minimizing the misfit objective function ϕ between measured and modeled fields. The lowest misfits obtained by the SAGA inversions (the cross signs connected by a solid line) are shown in Fig. 2.18(a). The solid line represents the best possible value of misfit for the available SNR (i.e., $1 - P_{\mathrm{BT,\,max}}$, see Eq. (2.2)). We see that low misfit values were obtained for all ranges. The best-fit results for SR and SD (Figs. 2.18(b) and (c), respectively) closely track the source position. The estimated water depth (Fig. 2.18(d)) exhibits the mild variation from inversion to inversion. The estimated array bow (Fig. 2.18(e)) shows a small amount of variation. The reason is that the current essentially was constant in direction and magnitude over this 20-minute time interval. The inversion results for the array tilt shown in Fig. 2.18(f) are in good agreement with the tilts determined by searching over only three geometrical parameters: SR, SD, and θ using 295 Hz (Fig. 2.15). Figures 2.18(g)–(k) show the inversion results for the geoacoustic parameters: sediment sound speeds c_{sed}, Δc, and sediment thickness d, attenuation α_{sed}, and density ρ_{sed}. Consistent values were obtained for geometrical parameters and sediment sound speed, attenuation, and thickness. Figures 2.18(l)–(n) show the inversion results for the first three ocean sound speed EOF coefficients

The parameter uncertainty was estimated using the best-fit models determined at each range over the time interval from 20 to 40 minutes. The mean and standard deviation for each of the parameters is indicated by the solid and dashed lines, respectively. Compared with the SAGA parameter estimate at SR = 1.7 km, the mean and standard deviation for each of the parameters is in excellent agreement. Table 2.4 summarizes the results of the comparison.

Since separate inversions were carried out for the acoustic data at each range

Table 2.4: Comparison of the Parameter Uncertainty Estimates

Parameter	Multiple Range Inversions	Single Range Inversion	
	Mean ± STD	$\text{SAGA}_{\text{mean}} \pm \sigma$	$\text{SAGA}_{\text{best}}$
c_{sed} (m/s)	1582 ± 9	1588 ± 7	1585
Δc (m/s)	55 ± 32	43 ± 24	74
d (m)	11 ± 3	10 ± 3	10
α_{sed} (dB/λ)	0.2 ± 0.1	0.2 ± 0.1	0.28
ρ_{sed} (g/cm^3)	1.9 ± 0.2	1.8 ± 0.2	1.8
EOF 1	6.4 ± 1.1	6.1 ± 0.6	6.3
EOF 2	-2.2 ± 0.8	-2.0 ± 0.6	-2.2
EOF 3	-0.7 ± 0.9	-1.7 ± 0.7	-1.6

Multiple Range Inversions: the means and standard deviations (STD) of the inversion results of Fig. 2.18.

Single Range Inversion: the best-fit model, and the PPD mean and standard deviation estimated at SR = 1.7 km.

over the 20-minute duration, a comparison of the measured and modeled acoustic fields at selected array elements was made. Figure 2.19 demonstrates the agreement between the observed and modeled fields. The measured field (solid line) was normalized by the total power registered at VLA at each range and the modeled field (dashed line) was computed using the best-fit model at each range and similarly normalized. It shows that the model fields reproduce the major features of the measured field reasonably well.

The variation from inversion to inversion in each parameter is used to examine parameter coupling. The coupling between model parameters can be quantified using the correlation coefficient matrix $\boldsymbol{\rho}$, defined by

$$\rho_{ij} = \frac{C_{M_{ij}}}{\sqrt{C_{M_{ii}} C_{M_{jj}}}} \tag{2.12}$$

where the covariance matrix $\mathbf{C_M}$ is calculated by

$$\mathbf{C_M} = \langle (\mathbf{m}_{\text{best}} - \langle \mathbf{m}_{\text{best}} \rangle)(\mathbf{m}_{\text{best}} - \langle \mathbf{m}_{\text{best}} \rangle)^T \rangle \tag{2.13}$$

with $\mathbf{m}_{\text{best}}$ is the best-fit model found at each inversion. Values of ρ_{ij} are bounded between -1 and $+1$, with $-1(+1)$ indicating a perfect negative (positive) correlation between parameters i and j, and 0 indicating uncorrelated parameters. For the purpose of demonstrating parameter coupling, only the absolute value of the correlation coefficient is considered. Figure 2.20 presents the magnitude of the linear correlation coefficient computed using the inversion results shown in Fig. 2.18. A strong coupling was observed for the following parameter pairs (WD, d), (WD, c_{sed}), and (d, c_{sed}), which is consistent with the observations in Fig. 2.11.

2.6 Conclusions

This chapter reports the geoacoustic inversion results based upon source tow data obtained during the ASIAEX 2001 East China Sea experiment. The source tow data recorded on a VLA were used to estimate the geoacoustic properties of the seafloor. The waveguide was assumed to be range-independent, and the seafloor was modeled as a homogeneous sediment layer overlying a semi-infinite subbottom.

Matched-field geoacoustic inversions using frequencies 195, 295, and 395 Hz were carried out by a genetic-algorithm-based optimization approach. The environmental

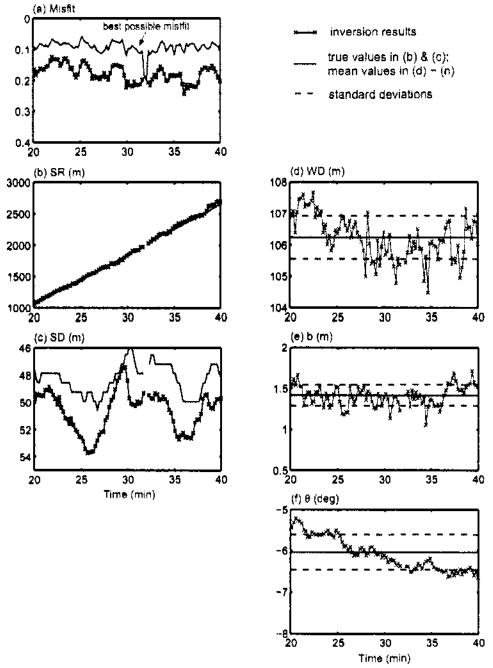

Figure 2.18: The inverted environmental parameter values versus time. (a) the solid line shows the best possible value for the available SNR and the cross signs connected by a solid line represents the lowest misfit attained by SAGA. (b)–(f) show the results for the geometrical parameters. The solid lines in (b) and (c) indicate the true measured values.

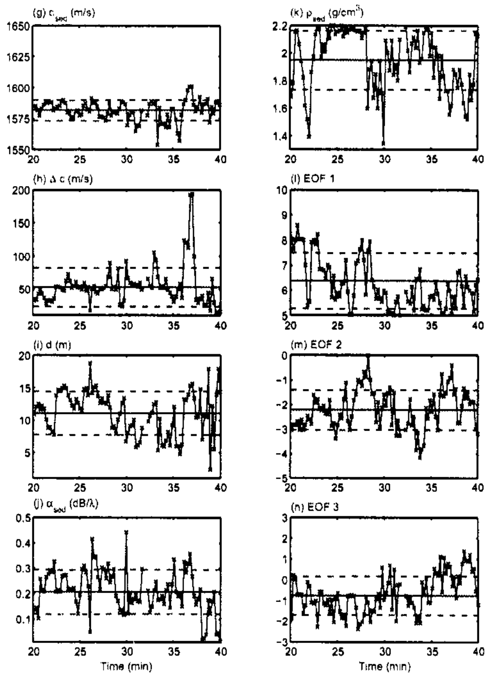

Figure 2.18: (cont'd) (g)–(k) show the results for the geoacoustic parameters; (l)–(n) show the results for the ocean sound speed EOF coefficients. The crosses connected by a solid line indicate the SAGA best-fit results. The solid and dashed lines indicate the mean and plus/minus one standard deviation of the mean, respectively. The vertical axis represents the search bounds.

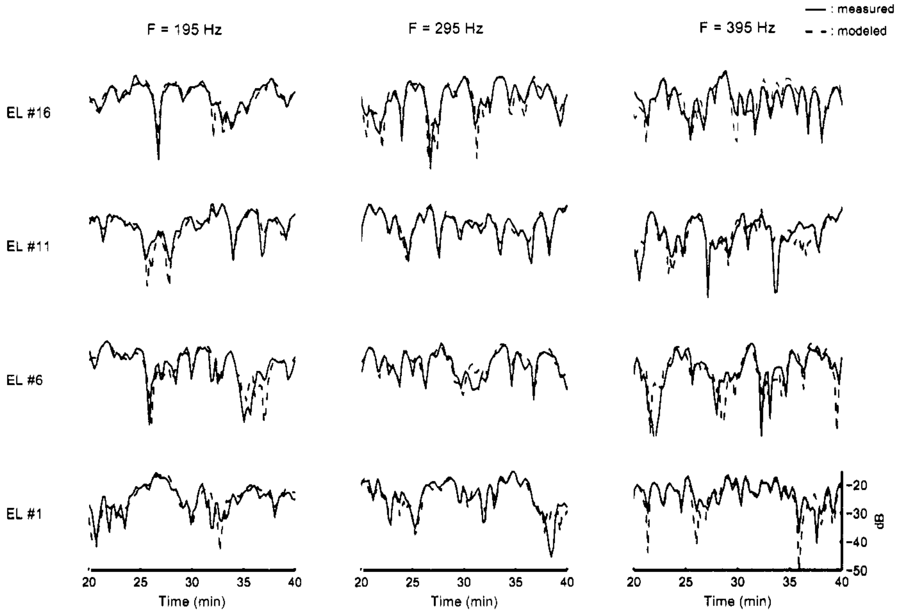

Figure 2.19: Normalized received levels for the measured (solid line) and normalized modeled (dashed line) fields as a function of time for the array elements 1, 6, 11, and 16 and for the frequencies 195, 295, and 395 Hz. The modeled fields were computed using the best-fit model found at each range.

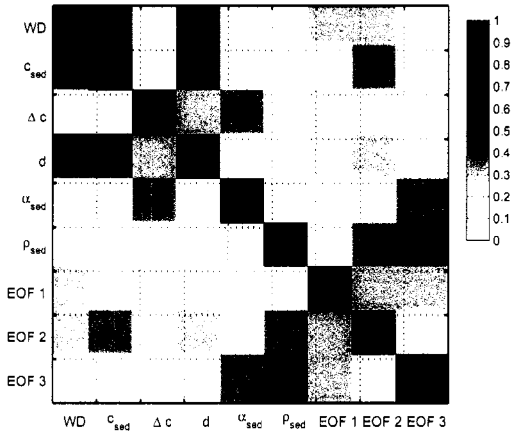

Figure 2.20: Correlation coefficient matrix for the environmental parameters computed using the inversion results shown in Fig. 2.18.

parameters were estimated by two different analyses to ensure the robustness of the inversion. These two analyses are summarized as follows:

1. The inversion was first performed with the set of data obtained at range of SR = 1.7 km. The accuracy of the inverted parameters was measured by the mean and the standard deviation of the posterior probability distribution. The results indicated a good agreement between the measured and the modeled sound fields. Furthermore, the inverted model quality was checked by using MF processing for source localization over the entire 30-min time interval. The predicted source positions track the measurements well.
2. A total of 98 separate inversions were carried out for the acoustic data at each range over the time interval from 20 to 40 minutes. The best-fit model at each range is the inversion result at that range. The data in this time interval covers a 1.5-km range. With the assumption that the seabed properties are range-independent, the resulting variations from inversion to inversion were used to analyze the parameter uncertainty. Low misfit values were obtained for all ranges, and consistent values were obtained for geometrical parameters and sediment sound speed, attenuation, and thickness. Also, a comparison of the measured and modeled fields was made and shows good agreement.

The parameter uncertainty (the mean and standard deviation) estimated from several inversions are in excellent agreement with the results at SR = 1.7 km. Parameter coupling was examined using the correlation coefficient matrix derived from the multi-range inversion results. The observed parameter correlations were consistent with our sensitivity results at SR = 1.7 km.

This chapter in part is a reprint of the material as it appears in Chen-Fen Huang and William S. Hodgkiss, “Matched field geoacoustic inversion of low frequency source tow data from the ASIAEX East China Sea experiment,” IEEE J. Oceanic Eng., Vol. 29, 952–963, 2004. The dissertation author was the primary researcher/author and the co-author listed in this publication directed and supervised the research which forms the basis for this chapter.

Chapter 3

Mid-Frequency Data Analysis

An environmental model in this study area initially was derived by matched-field (MF) geoacoustic inversion using low-frequency data (195, 295, and 395 Hz). The purpose of this chapter is to incorporate mid-frequency tonals (805, 850, and 905 Hz) into the geoacoustic inversion. First, the best-fit model found using the low frequency band, referred to as the low-frequency-derived best-fit model, is extended to the mid-frequency data in the application of MF processing source localization despite higher sidelobe levels. Second, in order to reduce the environmental uncertainties in the mid-frequency band, the data are incorporated into the MF inversion procedure. The quality of the refined model again is confirmed by time-continuous, source localization using mid-frequency data over the same time interval.

3.1 Sensitivity Analysis

To investigate the relative importance of the model parameters, a sensitivity study is carried out (see Sec. 2.4.4). By plotting the objective function (Eq. (2.6)) over the parameter interval, the relative importance of one parameter is evident. Figure 3.1 shows the parameter sensitivities for the low-frequency data (195, 295, and 395 Hz; dashed curves), mid-frequency data (805, 850, and 905 Hz; solid curves) and all 6 frequencies (dash-dotted curves). The nominal values of the estimated parameters are taken from the low-frequency-derived best-fit model (listed in Table 2.3), indicated by the dotted vertical lines.

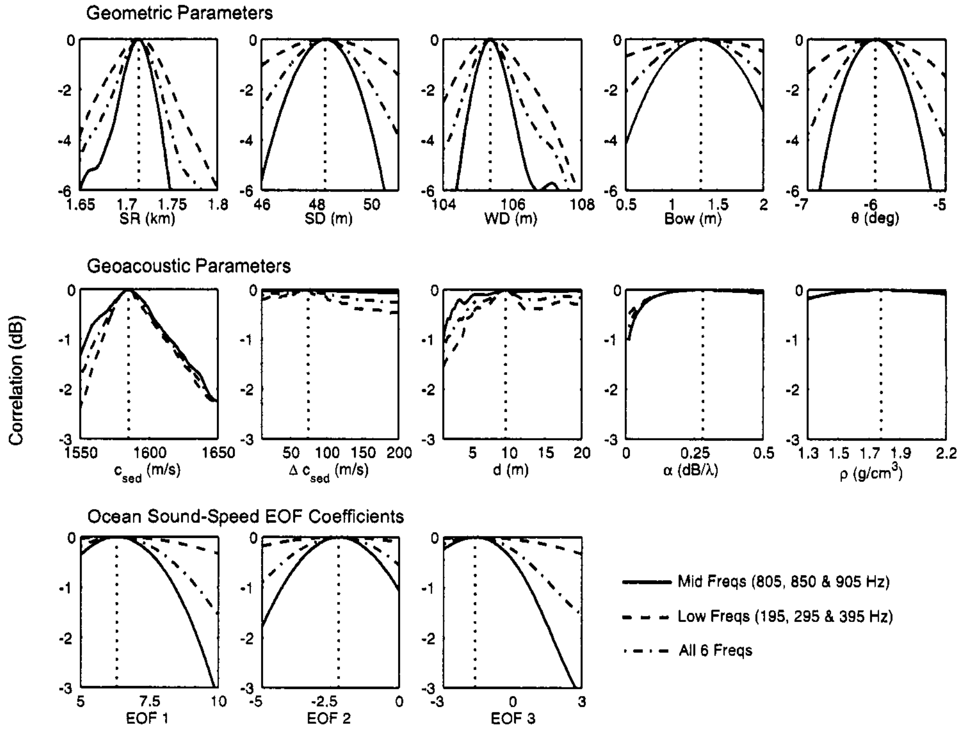

Figure 3.1: Sensitivity study of the model parameters for mid-frequency data analysis.

It shows that the geometrical parameters strongly influence the objective function value. In general, the geoacoustic parameters (c_{sed}, Δc and d) show rough (non-smooth) sensitivity curves. The non-smoothness of the curves is due to the number of propagating modes changing when varying the values of the parameter. The sensitivity of the basement sound speed increase (Δc) and the sediment thickness (d) mainly depends on how deep the signal can penetrate into the sediment. Therefore, to fathom the deep sediment properties, it is necessary to include lower frequency signals in the inversion. As for the density and attenuation of sediment, the results show that acoustic propagation is relatively insensitive to these parameters. The sensitivity of EOF coefficients has the same order as that of the geoacoustic parameters and their sensitivities increase with frequency.

Here is a summary of the observations: as frequency increases, (1) the acoustic field is more sensitive to geometric parameters, (2) is less sensitive to geoacoustic parameters, and (3) the ocean sound-speed profile becomes more important.

3.2 Model Parameter Estimation

Based upon the environmental parameter estimates obtained from the low frequency tonal data, the environmental models are re-optimized by incorporating the higher frequency data into the inversion.

Even though most of energy is in the first 3 sound speed structure EOF shape functions, the EOF reconstruction for the measured sound speed CTD0123 and CTD0547 indicates that EOFs 4 and 5 have significant energy as given in Table 2.1. (The time interval of the acoustic transmissions are bracketed by these two CTDs as shown in Fig. 3.2.) Therefore, we include these 2 additional EOF coefficients in the higher frequency inversion.

The total number of model parameters included in the geoacoustic inversion is now 15. The values of the GA parameters used here are as follows: the population size was set to 64, reproduction size was 0.5, crossover probability was 0.8, mutation probability was 0.05, number of iterations was 2500, and the number of parallel populations was set to 45. Approximately 112,500 forward models were run.

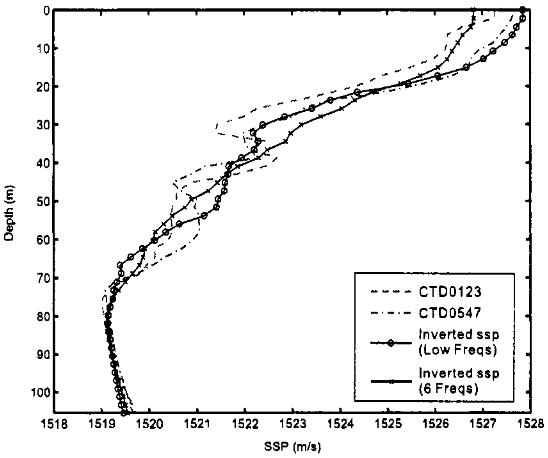

Figure 3.2: Comparison of the estimated sound-speed profiles from two inversions: using the low frequency signals (the circles connected by a solid line) and using all 6 frequencies (the crosses connected by a solid line). The dashed and dashed-dotted lines indicate the measured sound speed profiles on JD158.

3.3 Results and Discussion

Matched-field geoacoustic inversion using all 6 frequencies was carried out at the same source-receiver range (1.7 km) over the search space of 15 parameters. Table 3.1 tabulates the estimated parameter values. Compared with the inversion results obtained from the low frequency data (Table 2.3), it can be seen that the estimates of the geoacoustic parameters do not change much. However, it is likely that the estimated water depth is deeper than the true depth. (the measured water depth is 105 m with a margin of error of plus or minus 1 m). The biased estimation of water depth might result from accommodating possible deviations of other environmental parameters (for yielding the best matched-field response). The inverted ocean sound-speed profile from all 6 frequency data (the crosses connected by a solid line) is plotted in Fig. 3.2 along with the profile estimated from the low frequency data (the circles connected by a solid line).

Range-depth ambiguity surfaces are computed for each source frequency using the low-frequency-derived best-fit model and these are shown in Fig. 3.3(a). The bottom panels show the results of incoherently averaging Bartlett ambiguity surfaces using only

Table 3.1: Parameter Estimates at SR = 1.7 km using the frequencies of 195, 295, 395, 805, 850, and 905 Hz.

Parameter		SAGA$_{\text{best}}$
SR	(m)	1760
SD	(m)	49
WD	(m)	106.6
b	(m)	1.4
θ	(deg)	-6.06
c_{sed}	(m/s)	1581
Δc	(m/s)	73
d	(m)	10
α_{sed}	(dB/λ)	0.37
ρ_{sed}	(g/cm^3)	1.7
EOF 1		6.3
EOF 2		-1.0
EOF 3		-0.3
EOF 4		0.1
EOF 5		1.1

the low- (left) and only the mid- (right) frequency tonals. The ambiguity surfaces are normalized so that the peak level at each range is 0 dB. We see that incoherently averaging Bartlett ambiguity surfaces for the low frequency data suppresses the ambiguous sidelobes efficiently. For the mid-frequency data, no significant improvement is observed due to the relatively close frequency spacing of the signals (i.e., the structure of the sidelobes is similar across these frequencies). However, there is no ambiguity about the true source location. The results indicate that we can extend the best-fit model found using the lower frequency band to one-octave higher in the application of MFP source localization despite higher sidelobe levels.

Next, ambiguity surfaces are computed for each source frequency using the all-6-frequency-derived best-fit model and these are shown in Fig. 3.3(b). As shown in the second column of Fig. 3.3(b), the sidelobe level is decreased significantly. The reason is that by incorporating the mid-frequency data into the geoacoustic inversion, mismatch in the environmental parameters has been minimized as far as the selected frequencies are concerned. As a result, not only is higher maximum Bartlett power achieved, but also sidelobe level is suppressed.

As a test, we use the low-frequency-derived best-fit model for source localization using only the mid-frequency signals over the time interval from 20 to 50 minutes. Figure 3.4 (a) shows MF-derived source-receiver range (left panel) and source depth (right panel). Based upon the GPS measurements, the data in this time interval cover the range from 1 to 3.5 km. We see that the maximum Bartlett power is low (less than -3 dB) at each range and there is some source position ambiguity.

Figure 3.4 (b) demonstrates the performance of the all-6-frequency-derived best-fit model in source localization (using only the mid-frequency signals) over the same time interval. Relatively high maximum Bartlett power at each range is achieved and the resulting source position is consistent with the experimental configuration up to 45 minutes. Because environmental mismatch is reduced, there is little ambiguity in source position, resulting in the improvement in the performance of source localization.

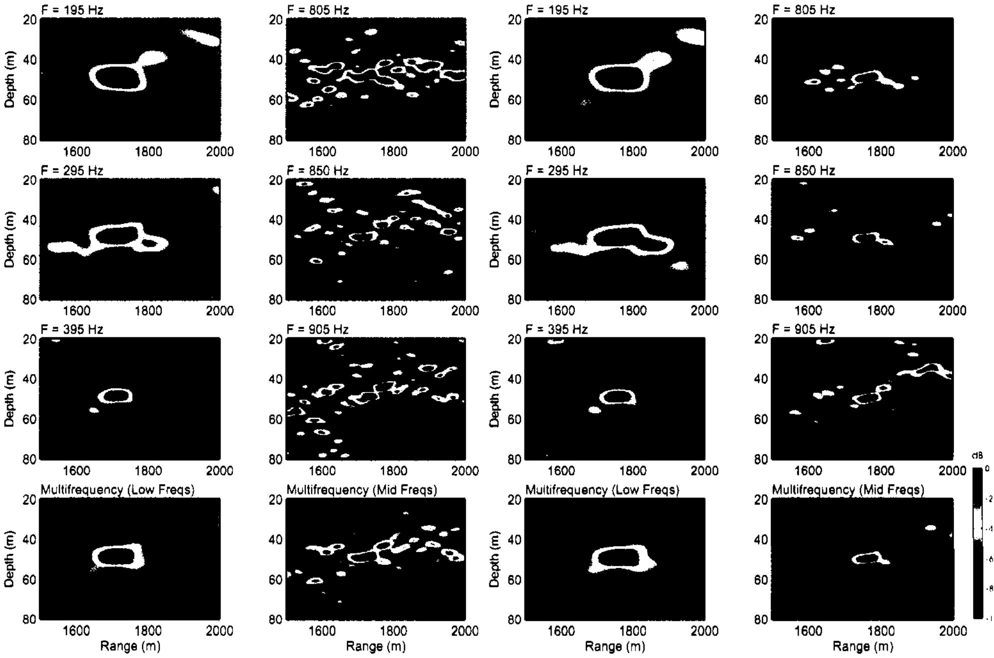

(a) Low-frequency-derived best-fit model

(b) All-6-frequency-derived best-fit model

Figure 3.3: Range-depth ambiguity surfaces at SR = 1.7 km for each source frequency and the multi-frequency average. (a) The replica pressure field is computed using the best-fit model derived from the low frequency signals (Table 2.3). (b) The replica pressure field is computed using the best-fit model derived from all 6 frequencies (Table 3.1). The estimated source position (SR and SD) and the Bartlett power obtained using the mid-frequency data are as follows: (a) (SR, SD) = (1722 m, 48.5 m) with Bartlett power = 0.415 and (b) (SR, SD) = (1761 m, 49.5 m) with Bartlett power = 0.626. On each ambiguity surface, the Bartlett power is normalized so that the peak level is 0 dB.

(a) Low-frequency-derived best-fit model

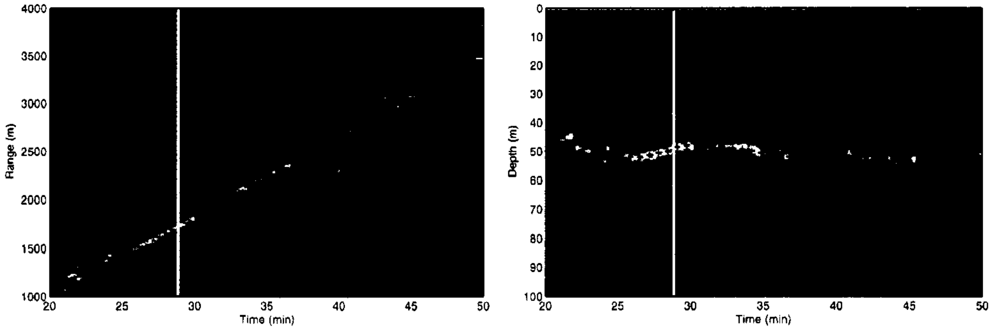

(b) All-6-frequency-derived best-fit model

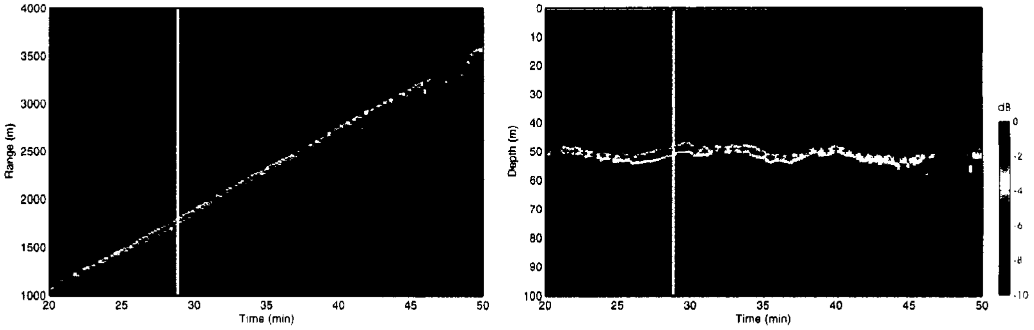

Figure 3.4: Comparison of MF-derived source-receiver range (left panels) and source depth (right panels) over the time interval from 20 to 50 min. (a) The replica pressure field is computed using the low-frequency-derived best-fit model. (b) The replica pressure field is computed using the best-fit model derived from all 6 frequencies. The white line on each plot indicates where the environmental model is estimated. The plus signs (right panels) indicate the true measured source depths. Here, the Bartlett ambiguity surfaces have not been normalized at each range.

3.4 Conclusions

This chapter has discussed geoacoustic inversion results based upon source tow data obtained during the ASIAEX 2001 East China Sea experiment. The source tow data recorded on a VLA were used to estimate the geoacoustic properties of the seafloor. The waveguide was assumed to be range-independent and the seafloor was modeled as a homogeneous sediment layer overlying a semi-infinite sub-bottom.

It was found that as frequency increases, the acoustic field is more sensitive to geometric parameters, less sensitive to geoacoustic parameters, and the ocean sound-speed profile becomes more important. Therefore, in addition to the original set of the environmental model parameters used in low-frequency data analysis, two more EOF coefficients were included. Matched-field geoacoustic inversions using 195, 295, 395, 805, 850, and 905 Hz were carried out by a genetic-algorithm-based optimization approach. The inversion was performed with the set of data obtained at range of SR = 1.7 km. The quality of the inverted model was confirmed by time-continuous, source localization using the mid-frequency data over a 30-min time interval.

This chapter in part is a reprint of the material as it appears in Chen-Fen Huang and William S. Hodgkiss, "Mid-frequency geoacoustic inversion of source tow data from the ASIAEX East China Sea experiment," Oceans2003 MTS/IEEE Conference Proceedings, San Diego, California, 576–581, 2003. The dissertation author was the primary researcher/author and the co-author listed in this publication directed and supervised the research which forms the basis for this chapter.

Chapter 4

Uncertainty Estimation

Quantifying uncertainty for parameter estimates obtained from matched-field geoacoustic inversions using a Bayesian approach requires estimation of the uncertainties in the data due to ambient noise as well as modeling errors. In this study, the variance parameter of the Gaussian error model, hereafter called error variance, is assumed to describe the data uncertainty. In practice, this parameter is not known *a priori*, and choosing a particular value is often problematic. Hence, to account for the uncertainty in error variance, several methods are introduced for implementing both the full and empirical Bayesian approaches. A full Bayesian approach that permits uncertainty of the error variance to propagate through the parameter estimation processes is a natural way of incorporating the uncertainty of error variance. Due to computational complexity of the full Bayesian approach, several methods which use the empirical Bayesian approach are developed, in which the posterior distributions of model parameters are conditioned on a point estimate of the error variance. Comparisons between the full and empirical Bayesian inferences of model parameters are presented using both synthetic and experimental data.

4.1 Introduction

Ocean acoustic data inversions typically have focused just on inverting the parameters for one environmental model [13,22,24,38,42], but some researchers have also considered selecting the best environmental parametrization over a family of geoacoustic models [6,64]. Under the Bayesian framework, all inferences are based on the posterior distribution $\mathrm{p}(\mathbf{m}|\mathbf{d}, \boldsymbol{\eta}_0)$ given by

$$\mathrm{p}(\mathbf{m}|\mathbf{d}, \boldsymbol{\eta}_0) \propto \mathrm{p}(\mathbf{d}|\mathbf{m}, \boldsymbol{\eta}_0)\mathrm{p}(\mathbf{m}|\boldsymbol{\eta}_0) \ , \tag{4.1}$$

where $\mathbf{m}$ represents the geoacoustic model parameter vector, $\mathbf{d}$ the data, and $\mathrm{p}(\mathbf{d}|\mathbf{m}, \boldsymbol{\eta}_0)$ and $\mathrm{p}(\mathbf{m}|\boldsymbol{\eta}_0)$ represent the likelihood and prior distribution conditioned on $\boldsymbol{\eta}_0$, respectively. The symbol $\boldsymbol{\eta}$ refers to other possible unknown quantities in our mathematical model, such as uncertainty in signal characteristics as well as uncertainty of other parameters not included in $\mathbf{m}$ (e.g., ocean water column sound speed parameters). As indicated above, it is customary to keep these quantities at fixed values $\boldsymbol{\eta}_0$.

Under the Bayesian approach, unless there is absolute certainty regarding the value of $\boldsymbol{\eta}$, inference of $\mathbf{m}$ should be made by integrating out the effect of $\boldsymbol{\eta}$ from the joint posterior probability $\mathrm{p}(\mathbf{m}, \boldsymbol{\eta}|\mathbf{d})$:

$$\begin{aligned} \mathrm{p}(\mathbf{m}|\mathbf{d}) &= \int \mathrm{p}(\mathbf{m}, \boldsymbol{\eta}|\mathbf{d})\, \mathrm{d}\boldsymbol{\eta} & (4.2) \\ &= \int \mathrm{p}(\mathbf{m}|\mathbf{d}, \boldsymbol{\eta})\mathrm{p}(\boldsymbol{\eta}|\mathbf{d})\, \mathrm{d}\boldsymbol{\eta}. & (4.3) \end{aligned}$$

The second representation shows that the posterior distribution of interest, $\mathrm{p}(\mathbf{m}|\mathbf{d})$, is a mixture of the conditional posterior distributions as shown in Eq. (4.1) given a fixed $\boldsymbol{\eta}$ where $\mathrm{p}(\boldsymbol{\eta}|\mathbf{d})$ is a weighting function for the different possible values of $\boldsymbol{\eta}$. This is referred to as a full Bayesian approach. A major problem with this approach is that the number of possible parameters to include in the uncertainty analysis might be quite large.

An alternative, the empirical Bayesian approach [11], is to replace $\boldsymbol{\eta}$ by a single estimate $\widehat{\boldsymbol{\eta}}$ obtained from the data. Inference of $\mathbf{m}$ is now based on the estimated posterior distribution

$$\mathrm{p}(\mathbf{m}|\mathbf{d}, \widehat{\boldsymbol{\eta}}). \tag{4.4}$$

This simplified approach essentially replaces the integration in Eq. (4.2) by an estimation step. Since the full Bayesian approach accounts explicitly for the uncertainty in $\boldsymbol{\eta}$, the inference of $\mathbf{m}$ based on Eq. (4.2) should produce a more correct distribution than that based on Eq. (4.4). For the linear forward model case adjustments to account for the uncertainty induced by estimating η, especially to produce valid parameter variances, can be found in Ref. [11].

This study discusses several methods for implementing both the full and empirical Bayesian approaches with a focus on one important parameter usually not included in the Bayesian analysis: the error variance ν in a Gaussian error model. However, our methods are applicable to any nuisance parameter. The error variance is influenced by both errors in the data and systematic errors in modeling the data. While error in the data, also known as noise, usually can be determined directly from the data (e.g., in the absence of signal), the systematic error is more difficult to assess. The error variance is important because incorrect choices for this parameter can seriously skew the posterior probability density (PPD) for the model parameters of interest.

The full Bayesian approach requires integrating out the nuisance parameters in Eq. (4.2) and either numerical or analytical *integration* can be used. Numerical integration is the most general approach as it can be carried out for any likelihood or prior distribution (see Sec. 4.3.1). Analytical integration is only possible for certain parameters with specific likelihood functions and prior distributions. For the error variance parameter in a Gaussian model, integrating out the error variance analytically (Sec. 4.3.2) makes this an attractive approach from both a computational and an analytical point of view.

For the empirical Bayesian approach, inferences are conditional on point estimates of the nuisance parameters in Eq. (4.4) and these can be estimated by either numerical or analytical *optimization* (as opposed to the integration used in the full Bayesian approach). Numerical optimization of the posterior probability with respect to both nuisance parameters and model parameters can easily be applied to most parameters and likelihood functions using standard optimization procedures [23,66] (Sec. 4.3.3). Analytic optimization is only feasible for certain combinations of likelihood functions and prior distributions. Assuming a Gaussian error model, it is possible to estimate the error variance analytically [38] (Sec. 4.3.4) and thus it is not necessary to use numerical optimization.

When estimating the error variance an interesting alternative to the point estimate (fixing the error variance at some specified value) is to use the analytic estimator of the error variance for each value of the model parameter vector [63]. This gives the same form of the posterior distribution as the full Bayesian approach (Sec. 4.3.4).

An objective of this study is the analysis of error variance. Since the computational expenses are of little concern for the example, an exhaustive evaluation of $p(\mathbf{m}|\mathbf{d})$ over a grid of parameter space combined with ordinary numerical integration is employed. This is a robust and accurate approach and is recommended for inverse problems with only a few parameters (e.g., less than eight parameters). However, if the number of parameters is large, Monte-Carlo methods of numerical integration [6,22] should be used.

For the exhaustive integration, it is easier to assess the convergence than for the complex Monte Carlo methods. The convergence was assured by running the exhaustive search with a certain discretization and then comparing the result to a down sampled result. The integration is done by simply summing the enumerated values over the grid, since the parameters near the edge of the parameter space usually has less contribution to the integral.

The remainder of this chapter is organized as follows. In the next section, the formulation of the inverse problem using the Bayesian approach is reviewed briefly. Section 4.3 outlines the approaches for handling error variance. Section 4.4 provides an analytic expression for PPD of error variance. Section 4.5 presents the results and compares the model parameter posterior probability distributions using both synthetic and experimental data. Lastly, a few concluding remarks are made in Sec. 4.6.

4.2 Formulation of the Inverse Problem

In a Bayesian approach for geoacoustic inversions, inferences about the model parameter vector $\mathbf{m}$ based upon an observed data vector $\mathbf{d}$ are made in terms of probability density functions (pdfs). The basic formula for Bayesian parameter estimation is represented by the posterior probability density function, $p(\mathbf{m}|\mathbf{d})$, which by Bayes' theorem is given by:

$$p(\mathbf{m}|\mathbf{d}) = \frac{p(\mathbf{d}|\mathbf{m})p(\mathbf{m})}{p(\mathbf{d})}, \tag{4.5}$$

where $\mathrm{p}(\mathbf{m})$ is the pdf associated with our *a priori* understanding of $\mathbf{m}$ before having access to the data $\mathbf{d}$.

The posterior probability density provides the full description of the state of knowledge about model parameters after observing the data. To interpret the multidimensional PPD, marginalization is used to summarize the PPD for a single parameter m_i by integrating over the remaining parameters $\mathbf{m}'$

$$\mathrm{p}(m_i|\mathbf{d}) = \int \mathrm{p}(m_i, \mathbf{m}'|\mathbf{d})\, \mathrm{d}\mathbf{m}'. \tag{4.6}$$

Also, 2-D marginal probability distributions of paired parameters can be obtained in a similar way. Further, the structure of the marginal posterior distribution is captured by the highest posterior density (HPD) interval (or region in the 2-D marginal) at a specified level of probability [8](Sec. 4.5.1).

4.2.1 Single frequency matched-field likelihood function

For matched-field geoacoustic inversions, the relationship between the observed complex-valued pressure field at a single frequency sampled at an N-element array and the predicted pressure field, at the frequency of interest, is described by the data model:

$$\mathbf{d} = \mathbf{D}(\mathbf{m}) + \mathbf{n}, \tag{4.7}$$

where $\mathbf{d}$ is the observed data and $\mathbf{D}(\mathbf{m})$ is the modeled data based upon a parameterized environmental model. In general, the modeled data is nonlinear with respect to the model parameter vector $\mathbf{m}$. The residual vector $\mathbf{n}$ represents the error terms. Typically, the residual vector is ambient noise but here the interpretation of $\mathbf{n}$ is broadened to include modeling errors.

If we assume that the error vector $\mathbf{n}$ is zero-mean complex Gaussian with covariance matrix $\mathbf{C}_\mathrm{D}$, i.e., $\mathbf{n} \sim \mathcal{CN}(0, \mathbf{C}_\mathrm{D})$, then the likelihood function $\mathrm{p}(\mathbf{d}|\mathbf{m})$ may be expressed as:

$$\begin{aligned}\mathrm{p}(\mathbf{d}|\mathbf{m}, \mathbf{C}_\mathrm{D}) = {} & \pi^{-N}|\mathbf{C}_\mathrm{D}|^{-1} \\ & \times \exp\Big[-(\mathbf{d}-\mathbf{D}(\mathbf{m}))^\dagger\, \mathbf{C}_\mathrm{D}^{-1}(\mathbf{d}-\mathbf{D}(\mathbf{m}))\Big],\end{aligned} \tag{4.8}$$

where N is the number of elements in the array and superscript † denotes the complex conjugate transpose. Here, for simplicity, we also assume that the error terms may be described by independent and identically distributed (IID) complex Gaussian random variables with common variance ν, i.e., $\mathbf{C}_{\mathrm{D}} = \nu\mathbf{I}$. This IID type of assumption is useful for convenience, but it may not completely model all the errors of interest. In what follows we shall always refer to the variable ν as the variance of the data errors.

The likelihood of the model parameter vector $\mathbf{m}$ for a given set of data may be written as:

$$\begin{aligned}\mathcal{L}(\mathbf{m}, \nu, s) &\equiv \mathrm{p}(\mathbf{d}|\mathbf{m}, \nu, s) \\ &= \frac{1}{\pi^N \nu^N} \exp\left(-\frac{\|\mathbf{d} - \mathbf{d}(\mathbf{m})s\|^2}{\nu}\right),\end{aligned} \tag{4.9}$$

in which the modeled data $\mathbf{D}(\mathbf{m})$ is represented by $\mathbf{D}(\mathbf{m}) = \mathbf{d}(\mathbf{m})s$, where $\mathbf{d}(\mathbf{m})$ is the replica field vector (or normalized signal field) computed using an acoustic propagation model for the model parameters $\mathbf{m}$, and s is the complex-valued source signature at the frequency of interest.

The source signature can be estimated either by the maximum-likelihood (ML) estimator, i.e., finding the value of s that maximizes the likelihood function [38], or, should we have no interest in its value, by treating s as a nuisance parameter and eliminating it by integration (as will be discussed in Sec. 4.3). Here we adopt the former method and obtain the ML estimate of the source parameter s as: $s_{\mathrm{ML}} = \mathbf{d}^{\dagger}(\mathbf{m})\mathbf{d}/\|\mathbf{d}(\mathbf{m})\|^2$. Substituting this relationship into Eq. (4.9) yields [38]:

$$\mathcal{L}(\mathbf{m}, \nu) = \frac{1}{\pi^N \nu^N} \exp\left(-\frac{\phi(\mathbf{m})}{\nu}\right), \tag{4.10}$$

where $\phi(\mathbf{m})$ denotes an objective function defined as:

$$\phi(\mathbf{m}) = \|\mathbf{d}\|^2 \left[1 - \frac{|\mathbf{d}(\mathbf{m})^{\dagger}\mathbf{d}|^2}{\|\mathbf{d}\|^2 \|\mathbf{d}(\mathbf{m})\|^2}\right] \tag{4.11}$$

in which the second term in the bracket is the normalized Bartlett power objective function [5] measuring the correlation between the data and the replica vectors. The objective function in Eq. (4.11) can be generalized [38] when multiple data snapshots are available.

4.2.2 Multi-frequency matched-field likelihood function

Assuming that the data errors are statistically independent across frequencies, then the multi-frequency matched-field likelihood function is the product of the single frequency counterparts:

$$\mathcal{L}(\mathbf{m}, \nu_1, \ldots, \nu_J) = \prod_j^J \mathcal{L}_j(\mathbf{m}, \nu_j) \tag{4.12}$$

where J indicates the number of the processed frequencies and $\mathcal{L}_j(\mathbf{m}, \nu_j)$ is the j-th frequency likelihood with the error variance denoted by ν_j as in Eq. (4.10). To illuminate the significance of ν_j, Eq. (4.10) is rewritten as

$$\mathcal{L}_j(\mathbf{m}, \nu_j) \propto \exp\left(-\frac{\phi_j(\mathbf{m})}{\nu_j} - N \ln \nu_j\right) \tag{4.13}$$

in which $1/\nu_j^N$ has been expressed as $\exp(-N \ln \nu_j)$ and the constant π^{-N} is omitted.

Frequency-dependent error variance

Error variance is frequency dependent. Not only does ambient noise vary across frequency but the error due to modeling mismatch also varies across frequency. With the assumption that errors are independent across frequencies, as in Eq. (4.12), the likelihood of $\mathbf{m}$ for multi-frequency cases is the product of the marginal likelihoods of $\mathbf{m}$ for each frequency, with ν_j being integrated out:

$$\mathcal{L}(\mathbf{m}) = \prod_j^J \int_{\nu_j} \mathcal{L}_j(\mathbf{m}, \nu_j)\, \mathrm{p}(\nu_j)\, \mathrm{d}\nu_j \tag{4.14}$$

where $\mathrm{p}(\nu_j)$ is the prior distribution of ν_j which will be specified in Sec. 4.2.3.

A single global error variance

A common approach is to assume the variation of the data error variances ν_j over the selected frequencies is negligible and model them by a single variable ν_0, i.e.,

$$\nu_j = \nu_0, \text{ for } j = 1, \ldots, J. \tag{4.15}$$

The likelihood for the selected frequencies with a common error variance ν_0 can be written as:

$$\mathcal{L}(\mathbf{m}, \nu_0) \propto \exp\left(-\frac{J}{\nu_0}\overline{\phi}^a(\mathbf{m}) - JN \ln \nu_0\right) \tag{4.16}$$

where $\overline{\phi}^a(\mathbf{m}) = \frac{1}{J}\sum \phi_j(\mathbf{m})$ is the arithmetic mean of the objective function over frequencies.

Equations (4.14) and (4.16) hold under the assumption that the errors are independent for each frequency. However, when the errors due to frequency-dependent modeling mismatch are the dominant source of error, the modeling error may not be independent across the frequencies used. Therefore, the number of frequencies J must be replaced with an effective number of frequencies J_{eff}.

4.2.3 Noninformative priors

Before applying Bayes' theorem to make inference of model parameters, one needs to specify their prior distributions. In situations where one does not have a strong prior belief, it is of use to have a natural reference prior. A noninformative prior is so called because it is noninformative with respect to the information in the data. For the model parameters $\mathbf{m}$, one may have prior knowledge from either historical data or the other measurements. Based on the prior knowledge, we assume that the values of the parameters are within lower bounds l_i and upper bounds u_i and are equally likely. Then a uniform distribution over that range is a practical choice for the prior,

$$\mathrm{p}(m_i) = \frac{1}{u_i - l_i}, \quad l_i < m_i < u_i. \tag{4.17}$$

For the error variance parameter, all one knows about this parameter *a priori* is that it is always positive but possibly of unknown order of magnitude (e.g., a standard deviation or a variance). It was suggested by Jeffreys [51] that based on invariance principles the noninformative distribution can be approximated by a uniform prior on $\ln \nu$ yielding :

$$\mathrm{p}(\nu) \propto \frac{1}{\nu}. \tag{4.18}$$

For further discussion, see Jaynes [49], Tarantola and Valette [78], and Box and Tiao [8].

With the additional assumption that all model parameters $(m_1, \ldots, m_M)$ and ν are mutually independent, the prior distribution is the product of the prior distributions for each parameter:

$$\mathrm{p}(\mathbf{m}, \nu) = \mathrm{p}(\mathbf{m})\mathrm{p}(\nu) = \prod_i^M \mathrm{p}(m_i)\mathrm{p}(\nu) \propto \frac{1}{\nu}, \tag{4.19}$$

over the interval where prior probability of $\mathbf{m}$ is nonzero. Then, based upon Bayes' theorem, the posterior distribution is as follows:

$$\begin{aligned} \mathrm{p}(\mathbf{m},\nu|\mathbf{d}) &\propto \mathrm{p}(\mathbf{d}|\mathbf{m},\nu)\mathrm{p}(\mathbf{m},\nu) \\ &\propto \mathcal{L}(\mathbf{m},\nu)\tfrac{1}{\nu} \\ &\propto \exp\left(-\tfrac{\phi(\mathbf{m})}{\nu} - (N+1)\ln\nu\right) \end{aligned} \tag{4.20}$$

with the scale factor that makes the posterior distribution integrate to one being omitted. The final representation of Eq. (4.20) will be extensively used in this analysis.

Note that the posterior distribution for a uniform prior on ν or for a uniform prior on $\ln\nu$ differs only in an N or $N+1$ in front of $\ln\nu$ (Eq. (4.20)). This suggests that for reasonably large N their respective PPDs are similar.

4.3 Error Variance as a Nuisance Parameter

In this section, we shall treat the error variance in a Gaussian error model as a nuisance parameter and discuss both the full and empirical Bayesian methods from an implementation perspective. For convenience of comparison, the approaches discussed below are summarized in Table 4.1.

4.3.1 Full Bayesian estimation – numerical integration

The full Bayesian approach is a natural way of incorporating the uncertainty of error variance in the analysis. The approach does not assume the error variance at a particular value, rather, it regards the error variance as an unknown in the parameter space. In this way, the approach allows the data uncertainty to propagate through the parameter estimation processes, and at the end, reflect uncertainty in the error variance in the resulting parameter estimation.

Therefore, the true posterior distribution of the model parameters is obtained by integrating out ν from the joint posterior distribution of $\mathbf{m}$ and ν:

$$\mathrm{p}(\mathbf{m}|\mathbf{d}) = \int \mathrm{p}(\mathbf{m},\nu|\mathbf{d})\,\mathrm{d}\nu. \tag{4.21}$$

4.3.2 Full Bayesian estimation – analytic integration

In this approach, the error variance is considered as a nuisance parameter and is eliminated by integrating the likelihood function weighted by the prior distribution of

ν over the entire range [2]:

$$\begin{aligned} \mathrm{p}(\mathbf{m}|\mathbf{d}) &= \int_0^\infty \mathrm{p}(\mathbf{m},\nu|\mathbf{d})\mathrm{d}\nu \\ &\propto \mathrm{p}(\mathbf{m}) \underbrace{\int_0^\infty \mathrm{p}(\mathbf{d}|\mathbf{m},\nu)\mathrm{p}(\nu)\,\mathrm{d}\nu}_{\mathrm{p}(\mathbf{d}|\mathbf{m})}. \end{aligned} \tag{4.22}$$

Incorporating the noninformative prior of ν in Eq. (4.18), the exact expression of $\mathrm{p}(\mathbf{d}|\mathbf{m})$ can be shown to be of the form[‡‡]:

$$\mathrm{p}(\mathbf{d}|\mathbf{m}) = \frac{1}{\pi^N}\frac{(N-1)!}{\phi^N(\mathbf{m})}. \tag{4.23}$$

This likelihood function is preferable in estimating PPD of model parameters for two reasons. Theoretically, this formula is derived based on a full Bayesian methodology. Computationally, this method is faster than a computer-based numerical integration of the full Bayesian procedure.

The above analytic solution, Eq. (4.23), can be extended straightforwardly to the multi-frequency data set. From Eq. (4.14), the multi-frequency likelihood function can be written in a concise form:

$$\mathcal{L}(\mathbf{m}) \propto \left(\frac{1}{\overline{\phi}^g(\mathbf{m})}\right)^{NJ} \tag{4.24}$$

where $\overline{\phi}^g(\mathbf{m}) = \sqrt[J]{\Pi\phi_j(\mathbf{m})}$ is the geometric mean of the objective function over frequency when the error variance is frequency dependent. However, for the case where the error variance is assumed to be constant over the processed frequencies, the arithmetic mean $\overline{\phi}^a(\mathbf{m})$ is used instead of $\overline{\phi}^g(\mathbf{m})$ in Eq. (4.24) in a manner analogous to that used by Ref. [63].

[‡‡] The derivation of the following formulas (4.23) requires substituting Eq. (4.10) and Eq. (4.18) into Eq. (4.22) and completing the integrand by the use of Gamma integral of the form:

$$\int_0^\infty x^{m-1}\exp(-ax)\,\mathrm{d}x = a^{-m}\Gamma(m).$$

Strictly speaking, the limits of the integration do not have to go form zero to infinity, since this prior is multiplied by a Gaussian likelihood function which dies away rapidly as $\nu \to 0$ and $\nu \to \infty$ (e.g., Refs. [2] and [9])

4.3.3 Empirical Bayesian estimation – optimizing error variance jointly with model parameters

The main idea behind this approach is to consider the error variance on the same level as the model parameters and optimize the joint posterior probability $\mathrm{p}(\mathbf{m}, \nu|\mathbf{d})$ to find the estimate of ν

$$\nu_{\mathrm{MAP}} = \arg\max_{\nu} \mathrm{p}(\mathbf{m}, \nu|\mathbf{d}). \tag{4.25}$$

Then, the posterior distribution of the model parameters is approximated by fixing the error variance at ν_{MAP}:

$$\mathrm{p}(\mathbf{m}|\mathbf{d}) \approx \mathrm{p}(\mathbf{m}|\mathbf{d}, \nu_{\mathrm{MAP}}) \propto \exp\left[-\frac{\phi(\mathbf{m})}{\nu_{\mathrm{MAP}}}\right]. \tag{4.26}$$

This approach is easier to implement numerically compared to the full Bayesian approach because the value of the error variance can be found by any efficient optimization procedure, such as simulated annealing or genetic algorithms [34].

4.3.4 Empirical Bayesian estimation – maximum likelihood estimate

The maximum likelihood estimator for the error variance can be obtained analytically

$$\nu_{\mathrm{ML}}(\mathbf{m}) = \frac{\phi(\mathbf{m})}{N}. \tag{4.27}$$

Two approaches for implementing this estimator in ocean acoustic inversions have been proposed by Mecklenbräuker and Gerstoft [63].

Following an empirical Bayesian methodology, one requires only an estimate of the error variance. First, the ML solution of model parameter vector, $\widehat{\mathbf{m}}$, is found (by minimizing the objective function, Eq. (4.11) over all $\mathbf{m}$). Second, an estimate of error variance is obtained [38]

$$\nu_{\mathrm{ML}}(\widehat{\mathbf{m}}) = \frac{\phi(\widehat{\mathbf{m}})}{N}. \tag{4.28}$$

Then, the PPD of $\mathbf{m}$ is approximated by fixing ν at $\nu_{\mathrm{ML}}(\widehat{\mathbf{m}})$:

$$\mathrm{p}(\mathbf{m}|\mathbf{d}, \nu_{\mathrm{ML}}(\widehat{\mathbf{m}})) \propto \exp\left[-\frac{\phi(\mathbf{m})}{\nu_{\mathrm{ML}}}\right]. \tag{4.29}$$

The error variance estimated from either ν_{MAP} (Eq. (4.25)) or ν_{ML} (Eq. (4.28)) often results in overly optimistic posterior distributions of the model parameters since a single value of the error variance may not be representative.

The other approach proposed in Ref. [63] is to substitute Eq. (4.27) into the likelihood formula (Eq. (4.10)) without fixing a value for ν. With the noninformative prior for $\mathbf{m}$, the PPD of $\mathbf{m}$ is proportional to the likelihood function

$$\begin{aligned} \mathrm{p}(\mathbf{m}|\mathbf{d}, \nu_{\mathrm{ML}}(\mathbf{m})) &\propto \mathrm{p}(\mathbf{m})\mathcal{L}(\mathbf{m}, \nu_{\mathrm{ML}}(\mathbf{m})) \\ &\propto \mathcal{L}(\mathbf{m}, \nu_{\mathrm{ML}}(\mathbf{m})) \\ &\propto \frac{1}{\phi^N(\mathbf{m})}. \end{aligned} \tag{4.30}$$

Note that the likelihood formula derived in Sec. 4.3.2 (Eq. (4.23)) and the result derived above (the third representation of Eq. (4.30)) possess the same functional form.

4.4 PPD of the Error Variance

The posterior distribution of ν is obtained by integrating the joint PPD over the model parameter vector:

$$\mathrm{p}(\nu|\mathbf{d}) = \int \mathrm{p}(\mathbf{m}, \nu|\mathbf{d})\, \mathrm{d}\mathbf{m} \tag{4.31}$$

One could always evaluate the integral in Eq. (4.31) numerically, but an analytic expression can be obtained under the simplifying Gaussian approximation for the PPD of the model parameters. This approach is known as Laplace's method, a family of asymptotic techniques used to approximate integrals. [7]

Inspired by Malinverno [61], let us assume that, for any value of ν, the PPD of the model parameter vector is approximated by a Gaussian function of $\mathbf{m}$ centered on the MAP solution $\widehat{\mathbf{m}}$ [§] with the posterior covariance matrix of model parameters $\widehat{\mathbf{C}}_{\mathrm{M}}$ (The hat is used to denote the quantity inferred *a posteriori*),

$$\mathrm{p}(\mathbf{m}, \nu|\mathbf{d}) \approx \mathrm{p}(\widehat{\mathbf{m}}, \nu|\mathbf{d}) \exp\left(-\frac{(\mathbf{m} - \widehat{\mathbf{m}})^T \widehat{\mathbf{C}}_{\mathrm{M}}^{-1} (\mathbf{m} - \widehat{\mathbf{m}})}{2} \right). \tag{4.32}$$

Since an unnormalized Gaussian pdf has the following constant

$$\int \exp\left(-\frac{\mathbf{m}^T \widehat{\mathbf{C}}_{\mathrm{M}}^{-1} \mathbf{m}}{2} \right) \mathrm{d}\mathbf{m} = (2\pi)^{M/2} \sqrt{|\widehat{\mathbf{C}}_{\mathrm{M}}|}, \tag{4.33}$$

[§] Note that the symbol $\widehat{\mathbf{m}}$ refers to both MAP and ML estimates of $\mathbf{m}$. In the absence of prior information on $\mathbf{m}$, the $\mathbf{m}$ that maximizes the likelihood function, the ML solution, is the same as the MAP solution that maximizes the posterior pdf $\mathrm{p}(\mathbf{m}|\mathbf{d})$.

substituting Eq. (4.20) into $p(\widehat{\mathbf{m}},\nu|\mathbf{d})$ yields the approximation to the marginal PPD of ν:

$$p(\nu|\mathbf{d}) \approx \frac{a}{\nu^{N+1}} \exp\left(-\frac{\phi(\widehat{\mathbf{m}})}{\nu}\right) \sqrt{|\widehat{\mathbf{C}}_{\mathrm{M}}|}, \tag{4.34}$$

where a is a scale factor that makes $p(\nu|\mathbf{d})$ integrate to one.

To evaluate the posterior covariance matrix of model parameters $\widehat{\mathbf{C}}_{\mathrm{M}}$, the forward model is linearized with respect to the best-fit model vector

$$\mathbf{D}(\mathbf{m}) \approx \mathbf{K}\,(\mathbf{m}-\widehat{\mathbf{m}}) + \mathbf{D}(\widehat{\mathbf{m}}), \tag{4.35}$$

where $\mathbf{K} = \frac{\partial \mathbf{D}(\mathbf{m})}{\partial \mathbf{m}}\big|_{\mathbf{m}=\widehat{\mathbf{m}}}$ is an $N \times M$ matrix of Fréchet derivatives evaluated at the best-fit model solution $\widehat{\mathbf{m}}$. Comparing the exponent of Eq. (4.32) with Eq. (4.8) in which the nonlinear forward model is substituted by Eq. (4.35) gives

$$\widehat{\mathbf{C}}_{\mathrm{M}} = \left(2\mathbf{K}^{\dagger}\mathbf{C}_{\mathrm{D}}^{-1}\mathbf{K}\right)^{-1}. \tag{4.36}$$

Since the data errors are expected *a priori* to be IID with variance ν ($\mathbf{C}_{\mathrm{D}} = \nu\mathbf{I}$) and with the further assumption that the model parameters are resolved by the data set, the determinant of $\widehat{\mathbf{C}}_{\mathrm{M}}$ is

$$|\widehat{\mathbf{C}}_{\mathrm{M}}| = \left|\frac{\nu}{2}\left(\mathbf{K}^{\dagger}\mathbf{K}\right)^{-1}\right| \propto |\nu\mathbf{I}_{M^*}| \propto \nu^{M^*}, \tag{4.37}$$

where M^* is the number of model parameters resolved by the data. Generally speaking, M^* is determined by the number of elements in the model parameter vector when $\mathbf{K}$ has full rank (all the model parameters are constrained by $\mathbf{K}$). However, due to the presence of noise, the parameter sensitivity and the possibility of linear dependence between the model parameters, not all of these may be estimated to a useful accuracy. Therefore, $M^* \leq M$. Then, substituting Eq. (4.37) into Eq. (4.34), we obtain the following approximation

$$p(\nu|\mathbf{d}) \propto \nu^{-[(2N-M^*)/2+1]} \exp\left(-\frac{\phi(\widehat{\mathbf{m}})}{\nu}\right). \tag{4.38}$$

This approximation to the marginal PPD of ν is the so-called inverse chi-square distribution used in Bayesian analysis (see Ref. [8], Sec. 2.3.1). However, the inverse chi-square distribution presented in Ref. [8] is based on real-valued Gaussian random

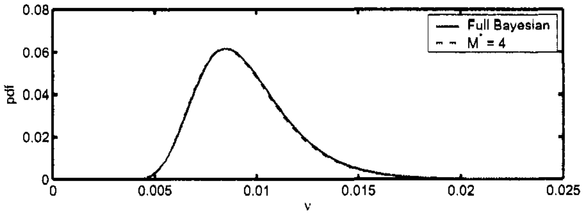

Figure 4.1: Posterior distribution of ν with a log-uniform prior on ν. solid curve: the numerical integration result from the full Bayesian approach. Dashed curve: the analytic result with $M^* = 4$.

variables. For the complex-valued Gaussian random variables, the scaled error variance $\nu/(2\phi(\widehat{\mathbf{m}}))$ has the inverse chi-square probability density with $2N - M^*$ degrees of freedom.

Figure 4.1 shows the posterior distribution of error variance taken from the synthetic data case where we inverted for 4 non-linear model parameters (details are given in Sec. 4.5.1 and Fig. 4.4). The solid curve is the numerical integration result obtained from the full Bayesian method. We approximate this full Bayesian result with the analytic expression in Eq. (4.38) by adjusting the parameter M^* and found that with $M^* = 4$ (dashed curve in Fig. 4.1) it has excellent agreement with the true PPD of ν. In this example, for the nonlinear forward model, the analytic expression of the posterior distribution of ν agrees well with the full Bayesian result, given the number of well determined parameters is used. As discussed later, setting $M^* = 4$ is reasonable since in this case all 4 parameters are well determined. Note that even though the PPDs of the geoacoustic parameters are only very approximately Gaussian, the PPD of ν follows an inverse chi-squared density.

4.5 Results and Discussion

4.5.1 Synthetic data

To illustrate the various approaches presented in Sec. 4.3, a data set is synthesized using the environmental model employed in the Geo-Acoustic Inversion Workshop 1997 [81]. Figure 4.2 shows the baseline model that consists of a downward refracting

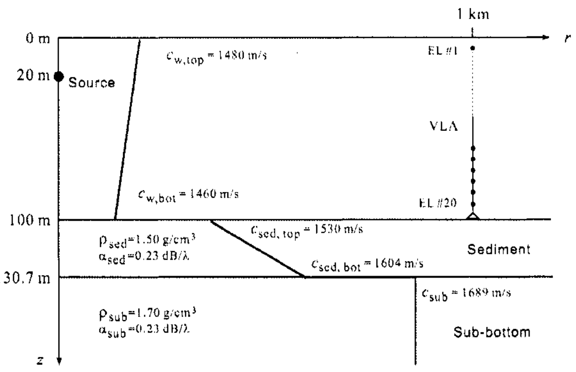

Figure 4.2: The **sdc** environment from the Geo-Acoustic Inversion Workshop 1997 [81] shown here for the parameters corresponding to ground true.

sound speed profile overlying a positive-gradient sediment layer atop of a homogeneous subbottom layer. The vertical array consists of 20 hydrophones equally-spaced over a 95 m interval with the first phone at 5-m depth, and the source located at 1-km range and 20-m depth, transmitting CW tones at 100 and 200 Hz. The calculations of acoustic fields are performed by the normal-mode propagation model ORCA [82]. To understand the interaction of acoustic fields with the environment, the range-depth acoustic fields for these two frequencies are plotted in Fig. 4.3.

In order to demonstrate the effect of error variance on the parameter estimation, the amount of noise corresponding to 20-dB SNR (equivalent to $\nu_{\text{true}} = 0.0083$, see Eq. (4.45) in the Appendix) is purposely added to the data. The parameters to be estimated are the geoacoustic parameters, including sediment thickness d, top and bottom sediment sound speeds $c_{\text{sed,top}}$, $c_{\text{sed,bot}}$, and subbottom sound speed c_{sub}, and the error variance ν. Figure 4.4 shows the parameter estimate using the full Bayesian approach for a frequency of 100 Hz. The line subplots along the diagonal are the one-dimensional (1-D) marginal PPDs for each parameter, $\text{p}(m_i|\mathbf{d})$, and the contour subplots in the upper triangle are the 2-D marginal PPDs corresponding to the paired parameters in the bottom-most and left-most line subplots, $\text{p}(m_b, m_l|\mathbf{d})$. In each contour plot, the gray-scale coloring from darkest to lightest represents 50%, 75%, and 95% highest posterior density (HPD). The β% HPD describes a region which contains β% of the total probability [8]. Due to the nonlinearity of the forward model, the PPD of model parameters is no longer Gaussian.

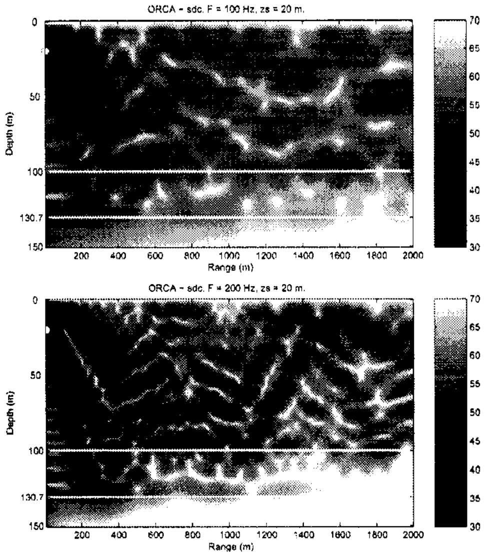

Figure 4.3: Range-depth transmission loss for $F = 100$ and 200 Hz, respectively using the **sdc** environment. The two white lines mark the water-sediment (top) and sediment-subbottom (bottom) interfaces.

Therefore, the best-fit model (cross signs in 2-D contours or arrow lines in 1-D plots) is not necessarily coincident with those from the mode of the marginal (plus signs in 2-D).

The 1-D and 2-D marginal PPDs reveal the uncertainty of the parameter estimation but in addition the 2-D PPDs also show the correlations between the paired parameters. For example, the contour subplot on row 1 and column 3 shows the correlation between bottom sediment sound speed $c_{\text{sed,bot}}$ and sediment thickness d. The result suggests that there is a strong positive coupling between these two parameters. Therefore, the inter-parameter correlation results in a relatively flat distribution in the 1-D marginal PPDs for the parameters $c_{\text{sed,bot}}$ and d. If more information about one of these two parameters could be obtained, then the 1-D marginal of the other could be sharpened. Likewise, the parameters of $c_{\text{sed,bot}}$ and $c_{\text{sed,top}}$ are strongly correlated in a negative manner. However, the 2-D PPDs for each pair of m_i and ν show that the error variance ν has little correlation with any other geoacoustic parameters, i.e., $\text{p}(m_i, \nu|\mathbf{d}) = \text{p}(m_i|\mathbf{d})\text{p}(\nu|\mathbf{d})$.

The error variances estimated from various approaches are summarized in Fig. 4.5. It shows the marginal PPD for the error variance using the full Bayesian approach,

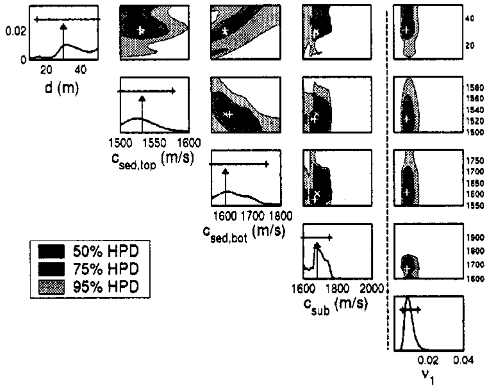

Figure 4.4: Marginal posterior probability densities (PPDs) of the geoacoustic parameters as well as the error variance for $F = 100$ Hz. In each 1-D marginal, the horizontal error bar shows 95% highest posterior density (HPD) interval.

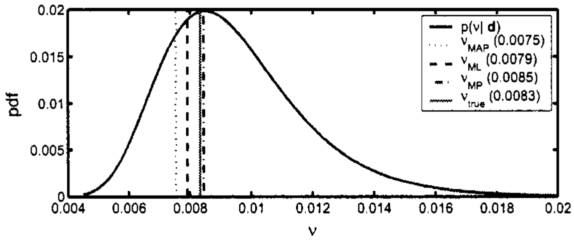

Figure 4.5: The enlarged version of the marginal posterior distribution of the error variance in Fig. 4.4. The vertical lines indicate the estimated error variances and the actual value of the error variance added to the data ($\nu_{\text{true}} = 0.0083$). Note that ν_{MMAP} is the MAP estimate of the marginal PPD of ν; it is not to be confused with the MAP estimate of the multidimensional joint PPD, ν_{MAP}.

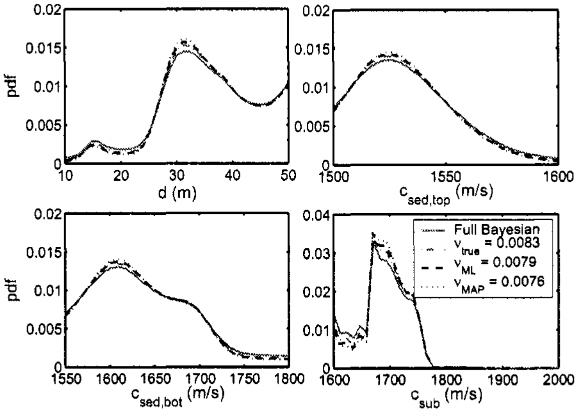

Figure 4.6: Comparison of the marginal PPDs for the geoacoustic parameters using different approaches in handling the error variance. ($F = 100$ Hz)

along with the estimates from the other approaches. In Sec. 4.4, it was shown that the error variance is distributed *a posteriori* as an inverse chi-square with $(2N - M^*)$ degrees of freedom, where here $M^* = 4$. One may consider the peak of this marginal posterior distribution as an estimate of the error variance, named as the marginal MAP (MMAP) value of error variance, ν_{MMAP}. The solid line shows the actual value of the error variance added to the data (0.0083). The ML (dashed), MAP (dot) and MMAP (dashed-dot) estimates of error variance are also shown. Among the various point estimates of error variance, ν_{MMAP} is the largest since it automatically takes into account the reduction in the degrees of freedom (for the inverse chi-square distribution) in the process of integration over the model parameters. The difference between the MAP and ML estimates of the error variance is due to the $1/\nu$ prior being used. Since the only uncertainty is the random error added to the data, there is not much difference in the estimated error variances among the various approaches.

The comparison of the marginal PPDs for each of the geoacoustic parameters is given in Fig. 4.6. The 1-D PPDs are estimated using full Bayesian treatment of error variance via numerical integration (solid; Sec. 4.3.1) and these using the empirical Bayesian methods based on the true value (dashed-dot), the ML (dashed) and MAP (dot) estimates of the error variance. In addition, the PPDs using the analytic integration of the full Bayesian approach (Sec. 4.3.2) are identical to these using numerical integration

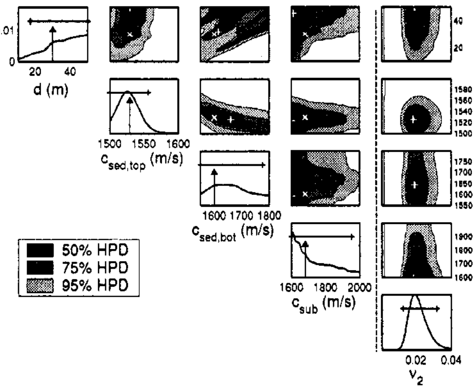

Figure 4.7: Full Bayesian approach. 1-D and 2-D marginal PPDs of the geoacoustic parameters as well as the error variance for 200 Hz. The actual value of the error variance added to the data is equivalent to 15-dB SNR ($\nu_{\text{true}} = 0.0194$). The format is the same as in Fig. 4.4.

(solid). From the simulations, the empirical Bayesian method using an ML or MAP estimate of the error variance is a good approximation to the full Bayesian approach.

$$\mathrm{p}(\mathbf{m}|\mathbf{d}) \approx \mathrm{p}(\mathbf{m}|\mathbf{d}, \nu) \tag{4.39}$$

However, the difference would become more distinguishable when the number of inverted parameters is similar to the number of the data points.

Figure 4.7 shows the marginal PPDs for the same parameter set using 200-Hz frequency data with the additive noise corresponding to 15-dB SNR ($\nu_{\text{true}} = 0.0194$) in contrast to the 20-dB SNR noise added to the 100-Hz data. Except for $c_{\text{sed,top}}$, the geoacoustic parameters are poorly estimated in comparison of Fig. 4.4. Since the higher frequency has higher resolution in the upper sediment (more structure in the acoustic field at the water-sediment, as seen in Fig. 4.3) but shorter penetration depth, only $c_{\text{sed,top}}$ is better resolved at this frequency.

Having estimated the marginal PPDs using data at 100- and 200-Hz frequencies separately, we then estimate the PPDs using data from both frequencies which have different error variances. Figure 4.8 demonstrates the multi-frequency case: (a) the error variance are appropriately accounted for (modeled by ν_1 and ν_2) and (b) the error variance are assumed the same over these two frequencies (modeled by ν_0). In addition, the

1-D PPDs using the analytic integration of full Bayesian method, Eq. (4.24), are shown in both figures; where the geometric mean is used for Fig. 4.8(a) and the arithmetic mean for (b). The results are not distinguishable from those using the numerical integration.

Comparing Figs. 4.8(a) with (b), we see there is slight difference between the two treatments of error variance. The uncertainties of the geoacoustic parameters using two frequencies (Fig. 4.8) are reduced significantly in contrast to those using single frequency (Figs. 4.4 and 4.7), in agreement with Refs. [13, 22, 38, 42].

4.5.2 Experimental data

Data acquired during the 2001 East China sea experiment (see Ref. [46]) are used to illustrate the approaches. A 16-element vertical line array was deployed in 105-m deep water (Element #4 failed during deployment). The source was towed at a depth of about 48.5 m. A general bathymetric and geological survey has indicated that in the neighborhood of the experimental site, the environment is nearly range-independent. Therefore, the ocean environment is modeled as an ocean layer overlying a uniform sediment layer atop of a basement. All layers are assumed to be range independent.

In our previous study [46], matched-field geoacoustic inversion using the frequencies 195, 295, and 395 Hz was carried out to invert for the seafloor parameters. Based upon the GPS position of R/V *Melville*, the observed data **d** was approximately 1.7 km away from the source. To reduce mismatch in water depth, source position, array geometry and ocean sound-speed profile, we have inverted for total 13 model parameters. In order to estimate the model parameters, a global optimization method, based on genetic algorithms, along with the normal-mode propagation model SNAP [52] was used.

We inspect here the posterior probability densities of the following 5 model parameters: water depth (WD), sediment sound speed (c_{sed}), basement sound speed increase (Δc), sediment thickness (d) and sediment attenuation (α_{sed}), with all other parameters fixed at their optimal values (using the empirical Bayesian treatment). The same data set is used in this analysis but with the selected frequencies of 195 and 395 Hz.

Figure 4.9 shows the full Bayesian approach for the multi-frequency case: (a)

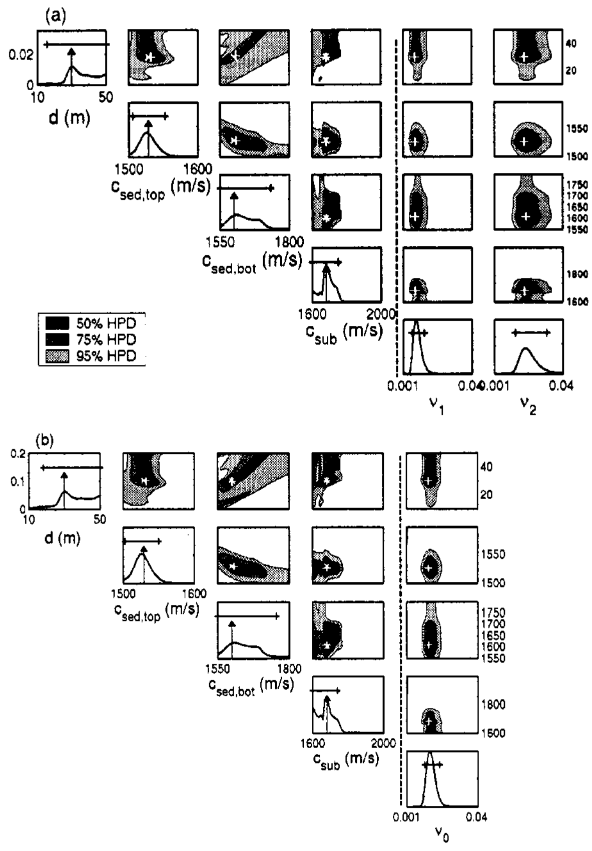

Figure 4.8: Full Bayesian approach for the multi-frequency case. (a) 1-D and 2-D marginal PPDs of the geoacoustic parameters as well as the error variances for frequency of 100 and 200 Hz. (b) The marginal PPDs of geoacoustic parameters as well as the global error variance. The format is the same as in Fig. 4.4.

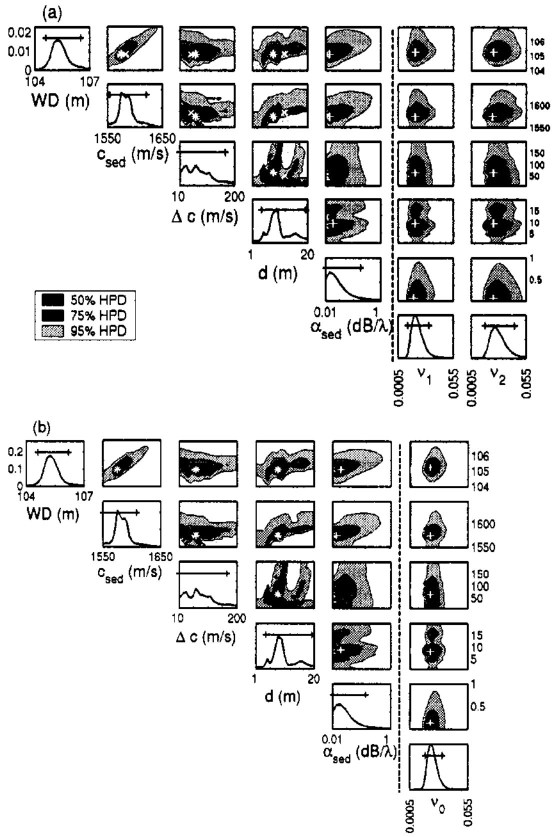

Figure 4.9: Full Bayesian approach for the multi-frequency case. (a) 1-D and 2-D marginal PPDs of the geoacoustic parameters as well as the error variances for the frequencies 195 and 395 Hz. (b) 1-D and 2-D marginal PPDs of the geoacoustic parameters as well as the global error variance. The format is the same as in Fig. 4.4.

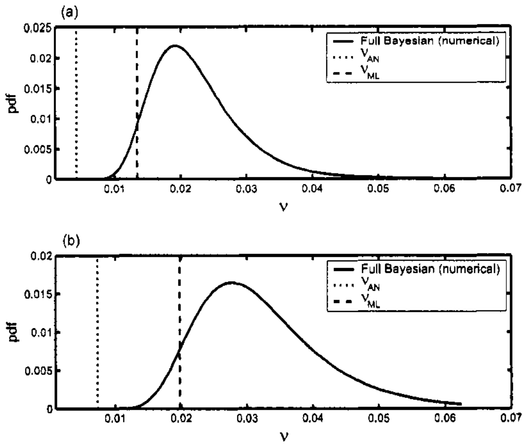

Figure 4.10: Posterior marginal distribution of the error variance obtained from the numerical integration. (a) $F = 195$ Hz and (b) $F = 395$ Hz. The vertical lines show the different estimates of error variance.

the frequency-dependent error variances are considered and (b) the error variances are assumed constant over frequencies. The error variances do not vary too much across the processed frequencies, therefore, the PPDs of the model parameters do not have significant difference between the two treatments of error variances.

Figure 4.10 shows the posterior marginal distributions of error variance obtained from the numerical integration: (a) $F = 195$ Hz and (b) $F = 395$ Hz. The error estimates from the other examined approaches are superimposed on the PPD of ν; the dotted line represents the ambient noise estimated directly from the data (corresponding to SNR = 23 and 21 dB, respectively) and the dashed line denotes the ML estimate of the error variance. The marginal distribution of the error variance captures that the effective error variance may be larger than the ambient noise estimate.

In the experimental data, with the high SNR, the modeling error in the parameterized environment is the dominant source of error in the estimation procedure. Because the modeling error may not be independent across the receivers, the IID assumption in the likelihood function is no longer appropriate; a full data uncertainty covariance matrix $\mathbf{C}_\mathrm{D}$ is needed. Therefore, to describe the data uncertainty for N complex-valued measurements, a huge number of quantities, N^2, needs to be estimated. A way to fix the defect of the likelihood function is to down sample the observations as adopted by

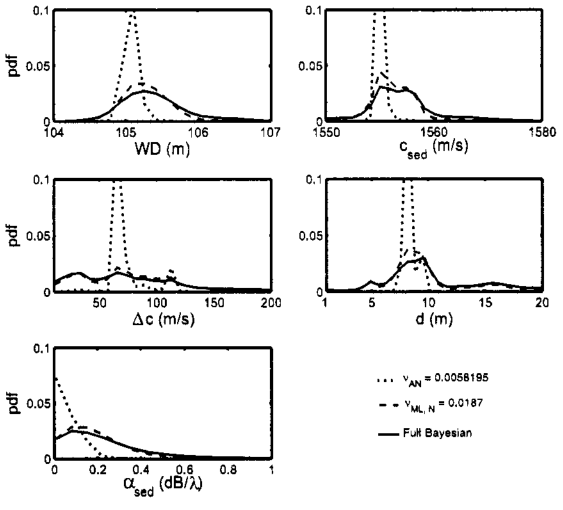

Figure 4.11: Comparison of the marginal PPDs for the model parameters.

Ref. [83].

Finally, the comparison of PPDs for the model parameters using different error variance estimates is shown in Fig. 4.11. The PPD of the model parameters using the ambient noise variance (dotted) yields too optimistic an uncertainty estimate. The PPD based on the ML estimate of error variance (dashed) is similar to the one obtained by the full Bayesian approach (solid). It is noteworthy that, in the 1-D marginal PPDs of WD and c_{sed}, the location of the peaks varies with different values of error variance. The reason is that there exists nonsymmetrically-distributed HPD contours in the joint marginal PPD, and when using a lower value of the error variance, the lower probability density in the 2-D marginal contributes more into the 1-D marginal distribution.

4.6 Conclusions

This chapter describes several methods for handling the nuisance parameters based on both the full and empirical Bayesian approaches. In a full Bayesian approach, the inference is made from the joint posterior probability distribution (PPD) of the model parameters and the nuisance parameters, whereas in an empirical Bayesian approach the PPD of the model parameters is conditioned on a point estimate of the nuisance parameters. The full Bayesian approach takes more complete accounting of uncertainty in nuisance parameters, but it is computationally expensive. The applications of the approaches to the error variance parameters in a Gaussian error model were examined.

Following a full Bayesian methodology, the analytic expression of PPD of the model parameters was derived for both single frequency (Eq. (4.23)) and multi-frequency data (Eq. (4.24)). The results (the discussions of Figs. 4.4, 4.7, and 4.8) show that the PPD of the model parameters using this analytic formula cannot be distinguished from that using numerical integration of the full Bayesian approach. Therefore, the analytic integration of the full Bayesian approach is theoretically and computationally preferred.

The analytic expression for the PPD of the error variance was derived. This analytic result agrees well with the distribution obtained using numerical integration, provided that the number of well-determined model parameters is used.

The empirical Bayesian approach using either the maximum likelihood or the maximum *a posteriori* estimate of the error variance was implemented. For the examples presented here, the 1-D PPDs of the model parameters using both the empirical and full Bayesian approaches yield similar results, but this is most likely not true in general.

4.7 Appendix: Additive noise

For the case that the observed data is written in the form of cross spectral density matrix (CSDM), the noise-contaminated data with error variance ν_0 is synthesized, based on true data $\mathbf{d}$, by

$$\mathbf{R} = \mathbf{d}\mathbf{d}^\dagger + \nu_0 \mathbf{I}. \tag{4.40}$$

The *array* signal-to-noise ratio (SNR) is the ratio of signal and noise powers

$$\mathrm{SNR} = 10 \log \frac{\mathbf{d}^\dagger \mathbf{d}}{\nu_0}. \tag{4.41}$$

Equation (4.11) can be generalized as

$$\phi_0(\mathbf{m}) \; = \mathrm{Tr}\mathbf{R} \left[1 - \frac{\mathbf{d}(\mathbf{m})^\dagger \mathbf{R} \mathbf{d}(\mathbf{m})}{\mathrm{Tr}\mathbf{R}} \right]. \tag{4.42}$$

Note that the replica field vector $\mathbf{d}(\mathbf{m})$ is computed from an acoustic model for the vector of unknown parameters $\mathbf{m}$ and is normalized to have unit length. If we normalize the objective function by the trace of the CSDM, denoted by $\mathrm{Tr}\mathbf{R}$, (the total intensity of the acoustic field recorded at the receivers):

$$\phi_n(\mathbf{m}) = \frac{\phi_0(\mathbf{m})}{\mathrm{Tr}\mathbf{R}}, \tag{4.43}$$

the noise estimate needs to be scaled by $\mathrm{Tr}\mathbf{R}$

$$\nu_n = \frac{\nu_0}{\mathrm{Tr}\mathbf{R}} = \frac{\nu_0}{\mathbf{d}^\dagger\mathbf{d} + N\nu_0}, \tag{4.44}$$

and is written in terms of the *array* SNR

$$\nu_n = \frac{1}{10^{\,\mathrm{SNR}/10} + N}. \tag{4.45}$$

Table 4.1: Summary of the Approaches (single frequency)

Approach	PPD of $\mathbf{m}$	Error Variance	Remark
4.3.1 Full Bayesian (numerical)	$\int \mathrm{p}(\mathbf{m}, \nu \vert \mathbf{d})\, \mathrm{d}\nu$	$\mathrm{p}(\nu \vert \mathbf{d})$	Computationally expensive
4.3.2 Full Bayesian (analytic)	$\frac{1}{\phi^N(\mathbf{m})}$	$\nu^{-[(2N-M^*)/2+1]} \exp\left(-\frac{\phi(\widehat{\mathbf{m}})}{\nu}\right)$	Theoretically & computationally preferred
4.3.3 Empirical Bayesian (numerical)	$\mathrm{p}(\mathbf{m} \vert \mathbf{d}, \nu_{\mathrm{MAP}})$	$\nu_{\mathrm{MAP}} = \arg\max_{\nu} \mathrm{p}(\mathbf{m}, \nu \vert \mathbf{d})$	Computationally efficient
4.3.4 Empirical Bayesian (analytic)	$\mathrm{p}(\mathbf{m} \vert \mathbf{d}, \nu_{\mathrm{ML}})$	$\nu_{\mathrm{ML}} = \frac{\phi(\widehat{\mathbf{m}})}{N}$	Computationally preferred

Chapter 5

Estimation of Transmission Loss: *A Posteriori* Analysis

A common problem in sonar system prediction is that the ocean environment is not well known. Utilizing probabilistic based results from geoacoustic inversions we characterize parameters relevant to sonar performance.

This chapter develops an approach for predicting transmission loss and its statistical properties based on posterior parameter probabilities obtained from inversion of ocean acoustic array data. This problem is solved by first finding an ensemble of relevant environmental model parameters and the associated posterior probability using a likelihood based inversion of the acoustic array data. In a second step, each realization of these model parameters is weighted with their posterior probability to map into the transmission loss domain.

This approach is illustrated using vertical-array data using a recent benchmarking data set and from data acquired during the ASIAEX 2001 East China Sea experiment. The environmental parameters are first estimated using a probabilistic-based geoacoustic inversion technique. Based on the posterior probability that each of these environmental models fits the ocean acoustic array data, each model is mapped into transmission loss. This enables us to compute a full probability distribution for the transmission loss at selected frequencies, ranges and depths, which potentially could be used for sonar performance prediction.

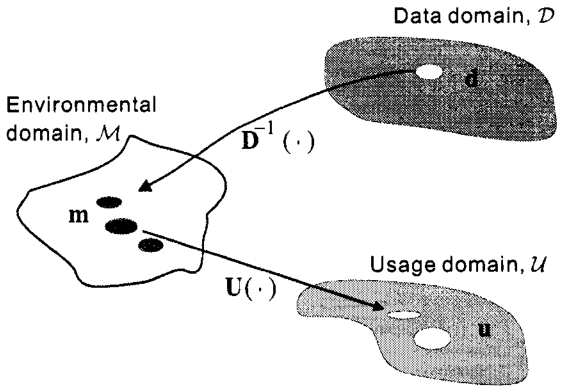

Figure 5.1: An observation $\mathbf{d}$ ($\in \mathcal{D}$) is mapped into a distribution of environmental parameters $\mathbf{m}$ ($\in \mathcal{M}$) that potentially could have generated it. These environmental parameters are then mapped into the usage domain $\mathcal{U}$.

5.1 Introduction

A weakness in sonar performance prediction has been the lack of means for quantifying the impact of uncertainty in estimates of the ocean environment. In the last decade there has been much work on inversion of geoacoustic parameters and their associated uncertainty, see Refs. [22, 32, 38, 48, 57, 71, 79]. An important problem is how to translate these parameters and their associated uncertainty into other domains where information can be used. In this chapter we will develop and show a method for translating this uncertainty into a utility domain, the transmission loss (TL) domain. The transmission loss domain is important as it can be used in connection with sonar performance prediction (e.g., Ref. [54] and in particular the paper by Abbot and Dyer [1]).

Figure 5.1 summarizes the estimation of TL (usage domain) from ocean acoustic data observed on a vertical or horizontal array (data domain). The geoacoustic inverse problem is solved as an intermediate step to find the posterior distribution of environmental parameters $p(\mathbf{m}|\mathbf{d})$ (environmental domain). We are not directly interested in the environment itself but rather better statistical estimation of the TL field, the usage domain $\mathbf{u}$. Based on the posterior distribution $p(\mathbf{m}|\mathbf{d})$, the probability distribution of the transmission loss $p(\mathbf{u})$ is obtained via Monte Carlo simulation. From this TL probability distribution, all relevant statistics of the TL can be obtained, such as the median and percentiles.

Both the experimental data $\mathbf{d}$ and the usage domain model $\mathbf{u}$ are related to $\mathbf{m}$ via forward models $\mathbf{D}(\mathbf{m})$ and $\mathbf{U}(\mathbf{m})$, respectively. Thus formally we have $\mathbf{u} = \mathbf{U}(\mathbf{D}^{-1}(\mathbf{d}))$. However, this direct mapping is ill-posed and is instead interpreted probabilistically where we also can include prior information. It is assumed that the mappings $\mathbf{D}(\mathbf{m})$ and $\mathbf{U}(\mathbf{m})$ are deterministic, so that all uncertainties are in the data and environmental parameters. However, in Mosegaard and Tarantola [69] and Rogers *et al.* [72], the forward mapping is assumed to be probabilistic.

Overview of Algorithm

The principle of the inversion is indicated in Fig. 5.1. Based on the ocean acoustic data $\mathbf{d}$ we statistically characterize TL (the usage domain $\mathbf{u}$). The vector $\mathbf{d}$ represents the acoustic data observed at N hydrophones and the vector $\mathbf{u}$ represents TL at several ranges and depths. As shown in Fig. 5.1, this is mapped via a set of M environmental parameters $\mathbf{m}$. The approach involves a number of steps as outlined below:

1. Determine an environmental parametrization for the ocean acoustic environment and select an appropriate propagation model. This defines the mapping $\mathbf{D}(\mathbf{m})$ from the environmental domain $\mathbf{m}$ to the data domain $\mathbf{d}$.
2. Determine the mapping $\mathbf{U}(\mathbf{m})$ from the environmental domain $\mathbf{m}$ to usage domain $\mathbf{u}$. Except for a change in geometry, here this is similar to the mapping used to determine $\mathbf{D}(\mathbf{m})$, but could be any other mapping.
3. Find acceptable model parameters $\mathbf{m}$ from the acoustic array data. As indicated in Fig. 5.1, a region around the data can map into several acceptable solutions in the environmental model domain.
4. Map the acceptable models $\mathbf{m}$ into the usage domain $\mathbf{u}$. Several environmental models can map into the same usage region.

As indicated in Fig. 5.1, the mapping from data to usage domain is non-unique. There are many environmental models that give about the same fitness to the observed data. Among those models, the maximum likelihood (ML) estimate of the environmental model gives the most likely fit. Instead of using just one estimated environment, it is proposed to describe the environmental solution probabilistically. This probability is then mapped into the usage domain. Knowing the posterior probability distribution in the usage domain is preferable to having a single point estimate, such as the usage domain result corresponding to the ML solution.

5.2 Inverse Problem Framework

In the Bayesian paradigm, the solution to determining parameters of interest $\mathbf{m}$ given an observation $\mathbf{d}$ is characterized by the posterior probability $\mathrm{p}(\mathbf{m}|\mathbf{d})$. First, the prior information about the model parameter vector is quantified by the probability density function $\mathrm{p}(\mathbf{m})$. Then, this information is combined with the likelihood function $\mathrm{p}(\mathbf{d}|\mathbf{m})$ provided by the combination of data and the physical model to give the posterior information of the model parameters $\mathrm{p}(\mathbf{m}|\mathbf{d})$. A complete discussion of inverse theory from a probabilistic point of view may be found in the recent textbooks by Tarantola [77]. Additional details of Monte Carlo sampling of posterior distributions can be found in Refs. [22, 38, 60, 68, 69, 74]. The solution to the inverse problem is then

$$\begin{aligned} \mathrm{p}(\mathbf{m}|\mathbf{d}) &= \frac{\mathrm{p}(\mathbf{d}|\mathbf{m})\mathrm{p}(\mathbf{m})}{\mathrm{p}(\mathbf{d})}, \\ &\propto \mathcal{L}(\mathbf{m})\mathrm{p}(\mathbf{m}) \end{aligned} \tag{5.1}$$

where $\mathrm{p}(\mathbf{d})$ is a normalizing factor that makes the posterior probability density $\mathrm{p}(\mathbf{m}|\mathbf{d})$ integrate to one; since it does not depend on environmental model $\mathbf{m}$, it is typically ignored in parameter estimation. Hence, as shown in the second representation, the normalization constant $\mathrm{p}(\mathbf{d})$ is omitted and a brief notation $\mathcal{L}(\mathbf{m})$ is used to denote the likelihood function $\mathrm{p}(\mathbf{d}|\mathbf{m})$. The posterior distribution $\mathrm{p}(\mathbf{m}|\mathbf{d})$ carries all information available on models originating from the data and from data-independent prior information. From this distribution all relevant features of the environmental model can be found such as the maximum *a posteriori* (MAP) estimator.

The posterior probability distribution $\mathrm{p}(\mathbf{m}|\mathbf{d})$ is M-dimensional, where M is the dimension of $\mathbf{m}$. How to compute the posterior distribution $\mathrm{p}(\mathbf{m}|\mathbf{d})$ depends on the dimension M. For small scale problems, $M \leq 8$, evaluating the likelihood function over a grid of parameter values seems most efficient. For medium scale problems, utilizing sequences of random numbers sampling from the posterior distribution, as known as

Markov chain Monte Carlo methods [6, 22], is most efficient. For large scale problems obtaining samples from the posterior distribution is impractical, it is necessary to make a Gaussian approximation to the posterior distribution which do not require extensive sampling of the posterior distribution, see e.g., Ref. [60, 78].

In order to develop the present method, we focus on small scale problems and thus the posterior distribution $\mathrm{p}(\mathbf{m}|\mathbf{d})$ is evaluated by computing the distribution over a grid of parameter values.

5.2.1 Probability of u

We are not only interested in the environment itself but also better estimates in the information usage domain $\mathbf{u}$. Based on the posterior distribution $\mathrm{p}(\mathbf{m}|\mathbf{d})$, the distribution $\mathrm{p}(\mathbf{u})$ is obtained and from this distribution all relevant statistics of the usage domain can be obtained. In the present application, the usage domain is transmission loss.

For either the posterior or prior probability distribution of the environmental parameters, the probability distribution of $\mathbf{u}$ is obtained

$$\mathrm{p}(\mathbf{u}) = \int_{\mathcal{M}} \delta[\mathbf{U}(\mathbf{m}) - \mathbf{u}]\mathrm{p}(\mathbf{m})\,\mathrm{d}\mathbf{m} \tag{5.2}$$

where $\mathcal{M}$ represents the environmental model domain. This integral is implemented numerically by using samples from the model domain $\mathbf{m}$ based on the probability distribution $\mathrm{p}(\mathbf{m})$ and then binning $\mathbf{U}(\mathbf{m})$. For the posterior it is implemented by first doing an inversion to determine $\mathrm{p}(\mathbf{m}|\mathbf{d})$ and storing the environmental samples $\mathbf{m}_i$ found in the inversion. These samples are then reused to compute the TL.

As the full probability distributions are available and are not necessarily Gaussian, it is preferable to characterize the distributions with medians and percentiles instead of means and standard deviations. Since the distributions are not symmetric around the medians, neither are the percentiles.

5.2.2 Likelihood and Objective Function

This section derives a likelihood function to be used in the probabilistic inversion following the same approach as described in Gerstoft and Mecklenbräuker [38, 63].

The relation between the observed complex-valued data vector $\mathbf{d}(\omega_l)$ on an N-element hydrophone antenna array and the predicted data $\mathbf{D}(\mathbf{m},\omega_l)$ at an angular frequency ω_l is described by the model

$$\mathbf{d}(\omega_l) = \mathbf{D}(\mathbf{m},\omega_l) + \mathbf{n}(\omega_l) \tag{5.3}$$

where $\mathbf{n}(\omega_l)$ represents the error term. The predicted data is given by $\mathbf{D}(\mathbf{m},\omega_l) = \mathbf{d}(\mathbf{m},\omega_l)s(\omega_l)$, where the complex deterministic source term $s(\omega_l)$ is unknown. The transfer function $\mathbf{d}(\mathbf{m},\omega_l)$ is obtained using an acoustic propagation model and an environmental model $\mathbf{m}$ [52]. For simplicity, data from only one frequency is assumed. However, the theory for multifrequency is also described in Refs. [38, 63].

Assume the errors $\mathbf{n}$ to be Gaussian distributed with zero mean and covariance $\mathbf{C}_\mathrm{D}$. The errors represent all features that are not modeled in the data such as noise, theoretical errors, and modeling errors. Hence, the likelihood function is

$$\begin{aligned}\mathcal{L}(\mathbf{m},\mathbf{C}_\mathrm{D},s) &= \pi^{-N}|\mathbf{C}_\mathrm{D}|^{-1} \\ &\quad \exp\Big(-[\mathbf{d}-s\mathbf{d}(\mathbf{m})]^\dagger {\mathbf{C}_\mathrm{D}}^{-1}[\mathbf{d}-s\mathbf{d}(\mathbf{m})]\Big)\end{aligned} \tag{5.4}$$

where N is the number of data points and superscript $\dagger$ denotes the complex conjugate transpose. Although strictly speaking not true, for convenience we assume $\mathbf{C}_\mathrm{D} = \nu\mathbf{I}$. The source term s can be estimated in closed form by requiring $\frac{\partial \log \mathcal{L}}{\partial s} = 0$, whereby

$$s_\mathrm{ML} = \frac{\mathbf{d}^\dagger\mathbf{d}(\mathbf{m})}{\|\mathbf{d}(\mathbf{m})\|^2} \,. \tag{5.5}$$

It is seen that s depends on $\mathbf{m}$ but not on ν. After substituting s_ML back into Eq. (5.4), the likelihood function is then

$$\mathcal{L}(\mathbf{m},\nu) = \frac{1}{\pi^N\nu^N}\exp\left(-\frac{\phi(\mathbf{m})}{\nu}\right) \tag{5.6}$$

where

$$\phi(\mathbf{m}) = \|\mathbf{d}\|^2 - \frac{|\mathbf{d}^\dagger\mathbf{d}(\mathbf{m})|^2}{\|\mathbf{d}(\mathbf{m})\|^2} \tag{5.7}$$

is the objective function. The maximum likelihood estimate of the noise ν_ML can be estimated in closed form by solving $\frac{\partial \log \mathcal{L}}{\partial \nu} = 0$,

$$\nu_\mathrm{ML} = \frac{\phi(\mathbf{m})}{N} \,. \tag{5.8}$$

The ML solution of the model parameter vector $\mathbf{m}_{\text{ML}}$ is obtained by maximizing the objective function over all $\mathbf{m}$. Finally, an overall estimate for the error power ν is obtained from Eq. (5.8) at the environmental ML solution: $\nu_{\text{ML}}(\mathbf{m}_{\text{ML}})$ and can be re-inserted into the likelihood function. For simplicity, we consider the error as known and only keep the free argument $\mathbf{m}$ of the objective function ϕ. This approach leads to [38]

$$\mathcal{L}(\mathbf{m}) = \left[\frac{N}{\pi\phi(\mathbf{m}_{\text{ML}})}\right]^N \exp\left[-N\frac{\phi(\mathbf{m})}{\phi(\mathbf{m}_{\text{ML}})}\right] . \tag{5.9}$$

The above derivation assumes that the error in each sample is uncorrelated with the next sample. In practice these are strongly correlated because the independent information is limited by the number of propagating modes. Therefore the number of samples N in the above equations must be replaced with the effective number of samples, N_{eff}.

5.3 Examples

Two examples are used to illustrate the approach. The first example (described in Sections 5.3.1 and 5.3.2) is based on Test Case 1 (TC1) of the geoacoustic inversion workshop [12] sponsored jointly by the Office of Naval Research (ONR) and the Space and Naval Warfare Systems Command (SPAWAR). The second example (Sections 5.3.3 and 5.3.4) is based on real data taken from the ASIAEX 2001 East China Sea experiment [46]. For both examples, we first carry out an inversion to obtain the posterior probability $p(\mathbf{m}|\mathbf{d})$ as discussed in Section 5.2.2 and then estimate the probability of the TL using Eq. (5.2).

As described in Sections 5.3.1 and 5.3.3, we first do a full inversion and then an exhaustive inversion for a few of the more important parameters. The reason for the two-step inversion procedure is to be sure that the posterior probabilities $p(\mathbf{m}|\mathbf{d})$ is sampled sufficiently dense so the transmission loss probability is correct. Ideally, these two inversions could be combined into one step.

Both examples were solved using the standard inversion package SAGA [32,34]. SAGA is a software package that helps the user determines the best set of parameters to match a given data set. SAGA has integrated some of the best ocean acoustic and electromagnetic forward model codes into the inversion and can handle many types of data, as documented in papers. As its main thrust it uses genetic algorithms, but also can handle simulated annealing, very fast simulated annealing, Cramer-Rao bounds, and Monte Carlo Metropolis sampling.

5.3.1 TC1 – Inversion

In the recent geoacoustic inversion workshop, several range dependent bottoms with a complicated geoacoustic structure were supplied. Here we focus on TC1. TC1 represents a monotonic downslope propagation with the bathymetry ranging from 90 m (0-km range) to 150 m (5-km range). The ocean sound speed profile is downward refracting and is given by $c_w(z) = 1495 - 0.4z$, where z is the water depth in meters. The source depth is 20 m. The data were generated by the fidelity parabolic equation RAMGEO code [16]. There was no uncertainty in recording geometry and both amplitude and phase were provided. For the present application, we use the vertical array data at 0.5-km range at frequencies 50 and 300 Hz to do the inversion. The bottom is modeled as a 3-layered sediment overlying a basement where the thickness and the sound speeds of each layer are the unknown model parameters. It should be pointed out that the true bottom is considerably more complicated than the 3-layered sediment model we are using. The inverted environmental parameters and their search bounds are indicated in Fig. 5.2 (e).

Figure 5.2 summarizes the whole inversion process (which is repeated from Ref. [36]). Detailed comments for each panel are provided below:

(a) A contour plot of the TL (dB) derived from the most likely (best-fit) environmental model.

(b) The comparison of observed TL (solid) and predicted TL (dashed) at 250 Hz for both the 20 m and 85 m deep array (the TL at 85 m has been offset downward 25 dB). Note that data from this frequency has not been used in the inversion and is thus a test of how well the inversion performed on the vertical array data.

(c) The match of the observed data (solid) and inverted field (dashed) on the vertical array at the frequencies (50 and 300 Hz) used in the inversion.

(d) The obtained (dashed) and true (solid) bottom sound speed profiles.

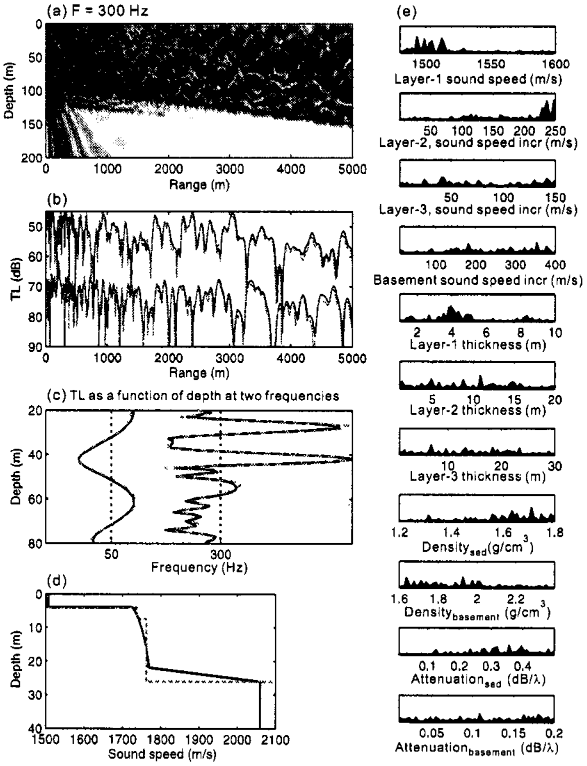

Figure 5.2: Inversion results for Test Case 1 (TC1) using vertical array data at 0.5 km (see the text for the details).

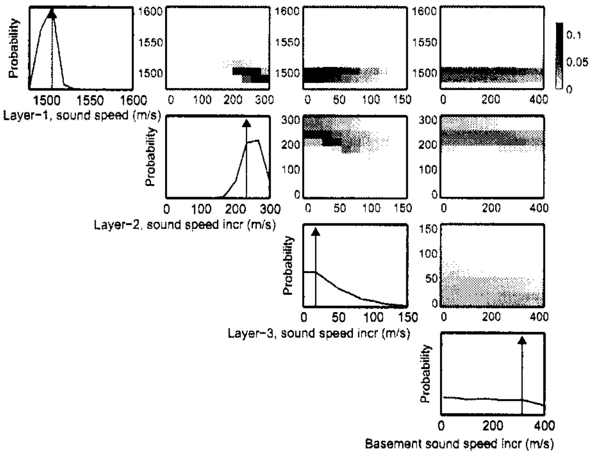

Figure 5.3: 1-D and 2-D marginal probability distributions for TC1 bottom sound speed profile. The vertical arrow indicates the ML solution (SAGA best-fit). Note that the maximum in the marginal distribution might not correspond to the ML estimate.

(e) The posterior distributions for the inverted model parameters.

Having found a good environmental parametrization and a model parameter estimate, a second inversion run is carried out to estimate the posterior distribution of the bottom sound speed profile, as shown in Fig. 5.3. All other parameters are kept at their optimal values found in the first inversion. Note that here we select arbitrarily a three-layered model for the bottom profile, but a more systematic approach would be to use evidence testing to find the most likely environmental parametrization [6]. The inverted parameters in the second inversion are the layer-1 sound speed, the increase in sound speed for layer-2 (from layer-1), the increase in sound speed for layer-3 (from layer-2) and the basement sound speed increase (from layer-3). For each parameter the search interval is discretized by 20 values. The upper and lower bounds of the search interval are indicated in Fig. 5.3. The likelihood function is evaluated exhaustively over the entire grid of 160,000 (20^4) samples.

5.3.2 TC1 – TL Estimation

All of the 160,000 samples are used for estimating the statistics of transmission loss at 250 Hz, 0 – 5 km in range, and 0 – 200 m in depth. For computing the prior field,

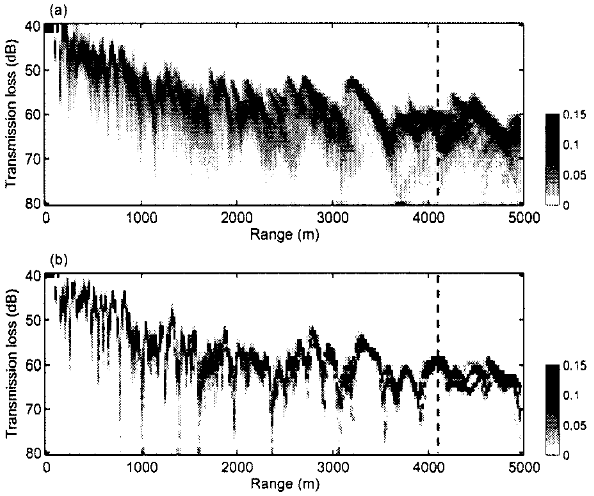

Figure 5.4: (a) Prior and (b) posterior probability distributions for TL versus range at 80-m depth for TC1.

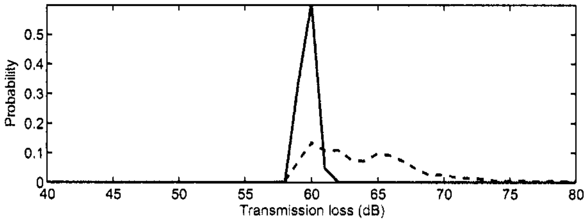

Figure 5.5: Posterior (solid) and prior (dashed) probabilities of TL at 4200-m range and 80-m depth. These correspond to a cut (vertical dashed lines) though the contours in Fig. 5.4.

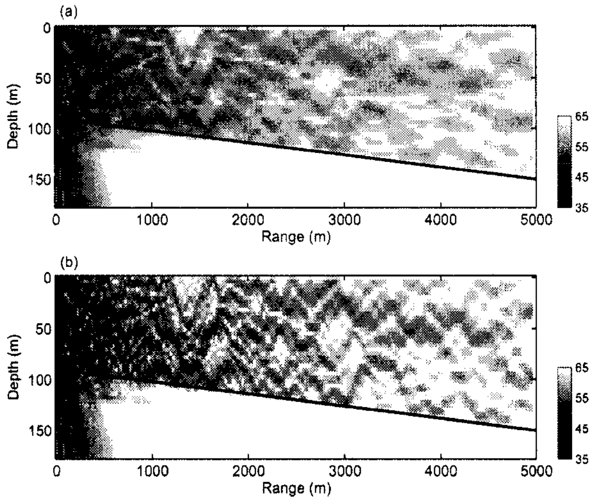

Figure 5.6: Median TL (dB) obtained from (a) prior and (b) posterior distributions of environmental parameters.

each parameter is weighted uniformly with bounds as indicated in Fig. 5.3. While for the posterior field, each model parameter is weighted according to its posterior distribution in Fig. 5.3.

Using these 160,000 samples, the probability distribution for the TL is computed at 80-m depth as a function of range, Fig. 5.4. The prior distribution is wider and the nulls are less sharp than the nulls for the posterior distribution. This can easily be seen by making a line plot (Fig. 5.5) of the prior (dashed) and posterior (solid) probabilities of TL at a range of 4200 m.

The prior and posterior median TL-fields are computed, Fig. 5.6. There is less structure in the prior TL field than in the posterior field. This is because the main parameters are more constrained. The spread in the prior and posterior fields is defined as the range between the 5th and 95th percentiles and is plotted in Fig. 5.7. It is seen that the spread in the water column for the posterior TL is much less than that for the prior TL. At shorter ranges (less than 1 km), the posterior field shows a large spread in the bottom. This may be a consequence of the choice of the bottom model, which is much more simple than the true bottom.

However, as seen in Fig. 5.7, this modeling error has limited influence on the

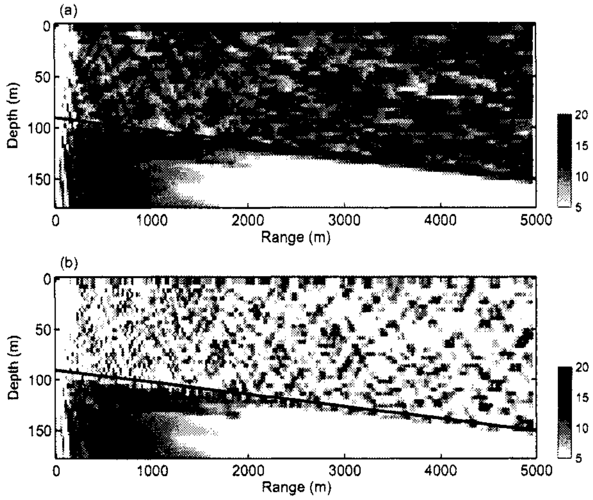

Figure 5.7: Range (dB) between 5th and 95th percentiles of the TL for (a) prior and (b) posterior probabilities.

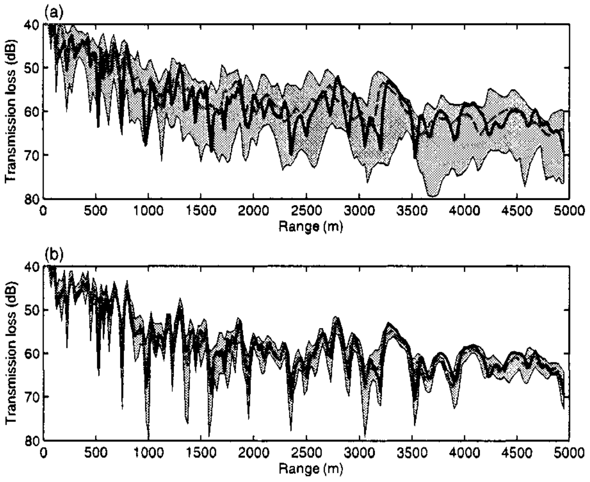

Figure 5.8: Median TL (dashed) and the true TL (solid) at 80-m depth obtained from (a) prior samples and (b) posterior samples. The gray area indicates the range between the 5th and 95th percentiles.

predicted wave field in the far-field bottom or near-field water column. At shorter ranges the sound field in the water column has fewer interactions with the bottom, due to the higher attenuation for the higher angle rays (higher-order modes). At longer ranges, the resolving power of the surviving low-order modes is consistent with the simple bottom model.

A practical way to display the uncertainty is to plot the median TL (dashed) combined with the 5th and 95th percentiles (represented by the gray area), as shown in Fig. 5.8. Clearly, the posterior spread is decreased significantly. Based on the true environment [12] the true TL (solid) is computed. Because the environmental model used in the inversion is a simplification over the true model, it is not clear how the true TL curve should relate to the median or spread of the posterior TL distribution. However, most of the true TL (solid) is within the spread (gray area) of the TL distribution.

It is interesting to notice that the range of the posterior probability (gray area) in Fig. 5.8 is larger than the prior at certain points in range. These points correspond to the ranges where the field is close to a null, causing large variations in the field.

5.3.3 ASIAEX – Inversion

Data from the 2001 East China sea experiment (see Ref. [46]) also are used to illustrate the method. A 16-element vertical line array (VLA) was deployed in 105-m deep water. The source was towed at a depth of about 48.5 m. The seafloor model consists of an ocean layer overlying a sediment layer atop of a basement. All layers are assumed to be range independent. Matched-field geoacoustic inversion using the selected frequencies 195, 295, and 395 Hz was carried out at T = 29 min. Based upon the GPS position of R/V *Melville*, the source was approximately 1.7 km away from the VLA. An environmental domain of 13 parameters, as indicated in Fig. 5.9 (with their search bounds), including geometrical, geoacoustic, and ocean sound speed EOF coefficients is inverted for.

Figure 5.9 shows the marginal dot diagrams for the model parameters. The vertical axis is the achieved misfit using a Bartlett objective function with respect to the parameter sampled during the SAGA optimization [32]. For each parameter, a simple parameter sensitivity (solid curve) was computed by keeping the other parameters fixed

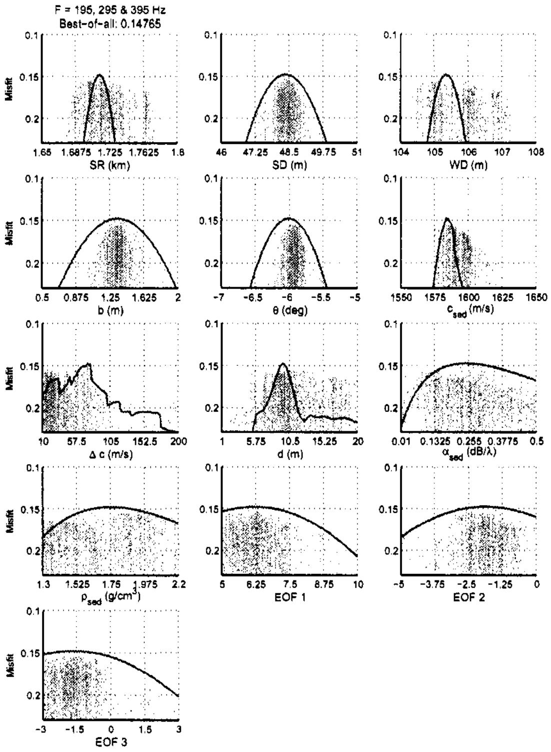

Figure 5.9: Marginal scatter diagrams of the SAGA search for the model parameters.

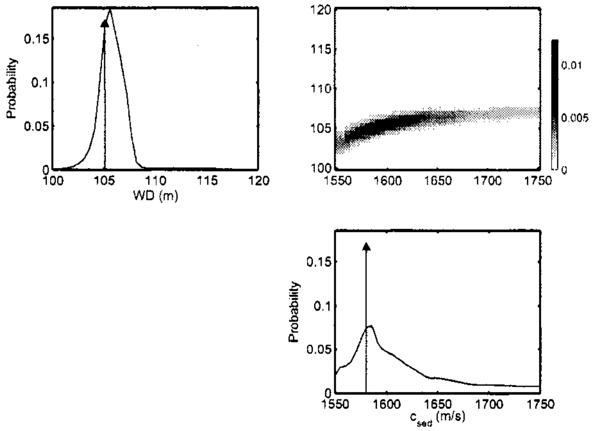

Figure 5.10: Marginal probabilities for water depth (WD) and sediment sound speed (c_{sed}). The contour plot shows the 2D distribution. The vertical arrow indicates the ML solution (SAGA best-fit). Note that the maximum in the marginal distribution might not correspond to the ML estimate.

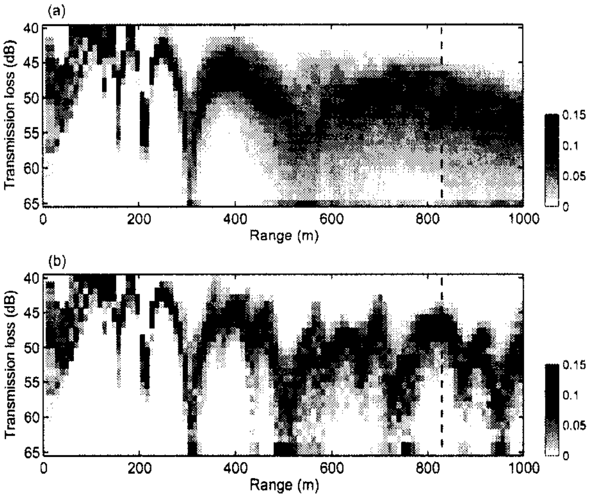

Figure 5.11: (a) Prior and (b) posterior probability distributions for TL versus range at 50-m depth.

at the optimal point and just varying the one parameter. We see that the sampled values for the array bow and tilt parameters (b and θ) are spread mainly inside the sensitivity curve and align mostly with the best-fit values. A similar behavior is observed for the ocean sound speed EOF coefficients but with a wider span. The consistency between the local (solid curve) and global (dots) searches shows that this set of parameters is weakly correlated with the other parameters. For the geoacoustic parameters, most sampled values wander outside the parameter sensitivity (solid curve). This reveals the more complicated structure of the multi-dimensional search space. Note that the sampled values for the source range (SR) and the water depth (WD) are spread uniformly throughout the range of the parameter interval. This is due to the strong coupling between these two parameters as could be observed by computing the 2D marginal distribution between these two parameters.

A second inversion is now carried out to determine the uncertainty for two of the most important model parameters. For simplicity, we assume that only water depth (WD) and sediment sound speed (c_{sed}) have any associated uncertainty. All other parameters are fixed at the optimal values found in the inversion detailed above. Varying only the above two parameters gives posterior probability indicated in Fig. 5.10. It is

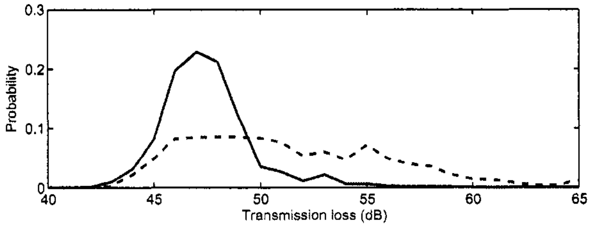

Figure 5.12: Posterior (solid) and prior (dashed) probabilities of TL at 830-m range and 50-m depth. These correspond to a cut (vertical dashed lines) though the contours in Fig. 5.11.

based on the likelihood formulation (Eq. (5.9)) and using the same data as in the full inversion.

5.3.4 ASIAEX – TL Estimation

The posterior probability (Fig. 5.10) is used to compute the posterior probability $\mathbf{u}$ using a frequency of 500 Hz and a source depth of 20 m. Except for water depth (bounds 100 to 120 m) and bottom sound speed (bounds 1550 to 1750 m/s), we keep the environment fixed at the values found in the inversion. In the present application, we evaluate this using grid integration. First the probability for TL at mid-water depth (50 m) is evaluated, Fig. 5.11. The prior probability assumes evenly weighting of all the explored environmental models with the same bounds as above. The prior distribution (a) is spread out over a wide range but the posterior distribution (b) is more narrow. For the first 200 m, the transmission loss is only little influenced by the waveguide parameters and thus there is little difference between posterior and prior distributions. We then examine the probability at one point (50-m depth and 830-m range). This is done by taking a cut through the contour plots in Fig. 5.11 at 830-m range (indicated by a vertical dashed line, corresponding to a peak in TL curve), as shown in Fig. 5.12. The posterior (solid) is much more concentrated than the prior (dashed).

Contours of the median TL then are computed for the prior and posterior fields, Fig. 5.13. A good way to understand the uncertainty is to plot the 5th to 95th percentile ranges (gray area) of the prior and posterior fields, Fig. 5.14. Close to the source, there is little uncertainty for both prior and posterior fields as the sound field is not influenced

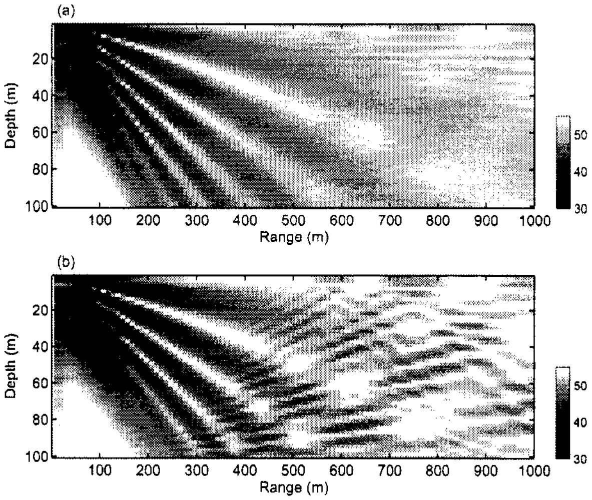

Figure 5.13: Median TL (dB) obtained from (a) prior and (b) posterior distributions of the environmental parameters.

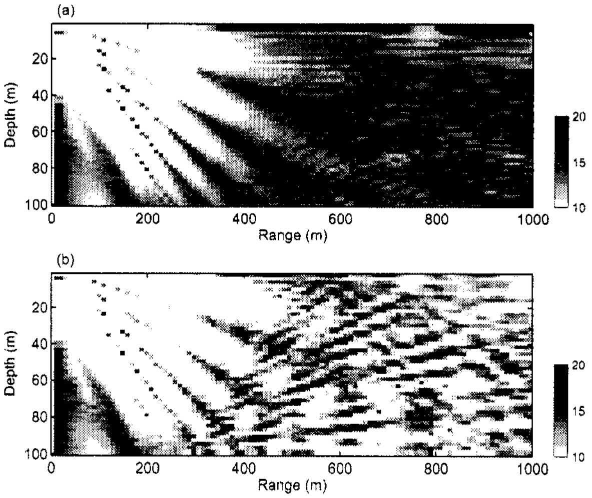

Figure 5.14: Range (dB) between 5th and 95th percentiles of the TL for (a) prior and (b) posterior probabilities.

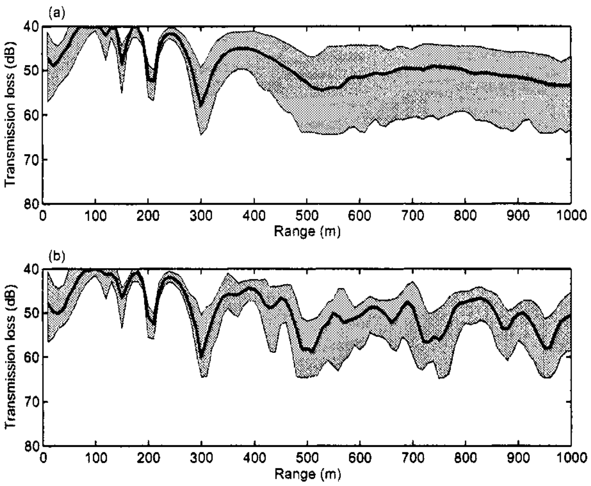

Figure 5.15: Median TL (solid) at 50-m depth obtained from (a) prior and (b) posterior samples. The gray area indicates the range between the 5th and 95th percentiles.

by the waveguide parameters. Further away from the source, the prior uncertainty increases earlier in range than the posterior does, as the waveguide parameters are less well determined. It also is seen that around the nulls of the median fields, Fig. 5.13, the variations in the fields are the largest, Fig. 5.14.

The uncertainty is easily conveyed by plotting the median TL (solid) combined with the 5th and 95th percentiles (represented by the gray area), see Fig. 5.15. Similar to the results for TC1, Section 5.3.2, it is observed that the posterior probabilities have the largest spread around the nulls of the median field. Overall, the posterior spread has decreased significantly.

5.4 Conclusions

An approach for estimating the statistical properties of transmission loss in the presence of uncertainty embedded in geoacoustic inversion has been developed using a likelihood formulation. The likelihood function assumes the error in the observed data is Gaussian. Examples presented used acoustic data on vertical arrays for the inversion, but any data could be used. The result of this inversion is a probabilistic-based description of the environmental parameters. The environmental parameters are mapped via their probability distributions into a probability distribution of transmission loss.

In the transmission loss domain, we can compute the full posterior distribution at all frequencies, ranges and depths. In the examples, we demonstrated how to use the full transmission loss probability distribution and extracted characteristic features such as median and lower/upper percentiles from this distribution.

Chapter 6

Conclusions

6.1 Conclusions

In this dissertation, I have developed a Bayesian framework for making quantitative statistical inferences about seabed properties from ocean acoustic data using matched-field processing techniques. Several important issues such as quantifying uncertainties due to measurement noise and modeling errors as well as estimating the statistical properties of transmission loss have been investigated. A few important accomplishments and conclusions of this study can be summarized as follows:

- An analysis of matched-field geoacoustic inversion based on data acquired during the ASIAEX 2001 East China Sea experiment was carried out. The source tow data (CW tones at 195, 295, 395, 805, 850 and 905 Hz) were used to infer the the geoacoustic properties in the area. The waveguide was assumed to be range-independent and consisting of an ocean layer overlying a uniform sediment layer on top of a subbottom.
- The environmental characteristics of the experimental site were identified. A sensitivity analysis was conducted to investigate the effects of geoacoustic and geometric parameters as well as the ocean sound-speed profile on the acoustic fields. It was found that the degree of influence of the environmental parameters on the acoustic fields depends on frequency. As frequency increases, the acoustic field is more sensitive to geometric parameters, less sensitive to geoacoustic parameters, and the ocean sound-speed profile be-

comes more important.

- The quality of the inverted model was checked using matched-field processing for source localization. It was found that, in the less than 1 kHz frequency band, the effect of environmental mismatch on source tracking can be reduced by using matched-field inversion techniques, resulting in improved source localization performance.
- The parameter uncertainty (in terms of the mean and standard deviation) given by the Bayesian approach was validated by comparing the variabilities of the estimated parameters inverted from multiple independent data sets.
- An extension of the Bayesian parameter uncertainty analysis to include uncertainty of data errors was carried out by two Bayesian approaches, i.e., full Bayesian and empirical Bayesian. In general, a full Bayesian approach is preferred, because it fully accounts for the posterior uncertainty of the data error, but an empirical Bayesian approach may be implemented more efficiently. The two Bayesian approaches were examined from the numerical and the analytical points of view.
- Following a full Bayesian methodology, we have derived the analytic expressions for the posterior probability distribution of the model parameters for single and multi-frequency data. The computational cost of implementing the full Bayesian approach is reduced significantly.
- The impact of uncertainty embedded in the geoacoustic inversion results on the estimation of transmission loss was investigated. An approach for estimating the statistical properties of transmission loss was developed using information on the model parameters obtained from the inversion. The utility of this approach is that one can compute the probability distributions of transmission loss at all frequencies, ranges and depths. Examples demonstrate the use of transmission loss probability density functions to extract characteristic features such as median and lower/upper percentiles.

6.2 Suggestions for Future Research

Throughout this study, we have assumed that data errors were independent and identically distributed complex Gaussian for the sake of simplicity. However, in reality, the errors may possess certain degree of correlation, especially those due to the modeling errors. Neglecting significant error correlations may lead to representing the data as more informative than they actually are, resulting in under-estimating the parameter uncertainties. Thus, estimating the data error matrix deserves further investigation.

Furthermore, in a Bayesian approach, the solution to the geoacoustic inversion problems always depend on the parametrization of the seabed. Information from the seismic measurements, sediment coring, *etc.*, is often used to build the environmental model at the outset. However, the proposed model might be more or less complex than that warranted by the measured data. A Bayesian approach to the model selection, as adopted by Battle *et al.* [6], may be used to find the most favorable environmental parametrization over a family of geoacoustic models.

An initial investigation has been made to apply matched-field geoacoustic inversion techniques to the higher frequency source tow data (CW tones at 1.6, 2.4, 3.5 and 4.4 kHz), but the estimated geoacoustic model performed poorly for matched-field source tracking. Matched-field processing/matched-field geoacoustic inversion utilizes the relative phase information of the observation and is very sensitive to the geometric parameters and the dynamics of the water column as frequency increases. In the study area, significant ocean sound speed fluctuations (about 15-m vertical shift of the thermocline) were observed in the CTD measurements made before and after the high frequency transmissions. Time dependent motion of the sea surface also gives rise to heaving of the towed source, thus introducing additional temporal variability in the acoustic field. Both of these, in addition to range dependent seafloor characteristics, lead to a fluctuating and complex spatial structure in the acoustic field that must be accommodated.

Further theoretical research in this area may include devising signal processing techniques included with the inversion procedure that are robust to the fluctuating component of the acoustic field. Also, transmitting broadband signals may be considered in the future experiments. Integrating across frequency might provide additional stability and would facilitate implementing a broadband matched-field processing or envelope approach as done in Hursky *et al.* [47].

Appendix A

Parabolic-Shape Array

— in which Eq. (2.5) is derived.

The shape of array may be deviated from a straight line due to the drag force resulted from nonuniformly-distributed currents. The bent array is computed in the xz-plane with the axis of the array located along the z-axis and the deviation in the x-axis. The parabolic array has be assumed and specified in terms of the bow b at the mid-point of the array and the length of the straight array L_s. The standard equation of a parabola that opens to the left with the vertex at $(b, \frac{L_p}{2})$ is

$$\left(z_p - \frac{L_p}{2}\right)^2 = -4p\,(x_p - b) \tag{A.1}$$

where x_p and z_p are the local x- and z-coordinates, respectively, L_p is the length of the parabolic-shape array along the z-axis, and the length $4p$ can be replaced by $\frac{L_p^2}{4b}$ because the first element is located on the origin. Then, Eq. (A.1) can be rewritten by

$$x_p = \frac{4b}{L_p^2}(L_p - z_p)z_p. \tag{A.2}$$

The arc length L_s of the parabola from $z_p = 0$ to $z_p = L_p$ is

$$\begin{aligned} L_s &= \int_0^{L_p} \sqrt{1 + \left(\frac{\partial x_p}{\partial z_p}\right)^2}\, dz_p && \text{(A.3)} \\ &= \frac{L_p}{2}\left[\sqrt{1+c^2} + \frac{1}{2c}\ln\frac{\sqrt{1+c^2}+c}{\sqrt{1+c^2}-c}\right] && \text{(A.4)} \\ &= L_p\left(1 + \frac{8}{3}\frac{b^2}{L_p^2} - \frac{32}{5}\frac{b^4}{L_p^4} + \ldots\right) && \text{(A.5)} \end{aligned}$$

where $c = \frac{4|b|}{L_p}$. By solving Eq. (A.5), the length of the parabolic-shape array along the z-axis can be approximated by

$$L_p \approx L_s \left(1 - \frac{8}{3}\frac{b^2}{L_s^2}\right) \tag{A.6}$$

Due to the bow of the array, the displacement and depth of each array element are modified by

$$(x_p, z_p) = \left(\frac{4b}{L_s^2}\left(L_s - z_s\right) z_s,\ \left(1 - \frac{8}{3}\frac{b^2}{L_s^2}\right) z_s\right). \tag{A.7}$$

where z_s is z-coordinate of the straight array.

Figure A.1 shows the bowed-array shape and the depth deviation of the uppermost element for 0.5-m bow increment.

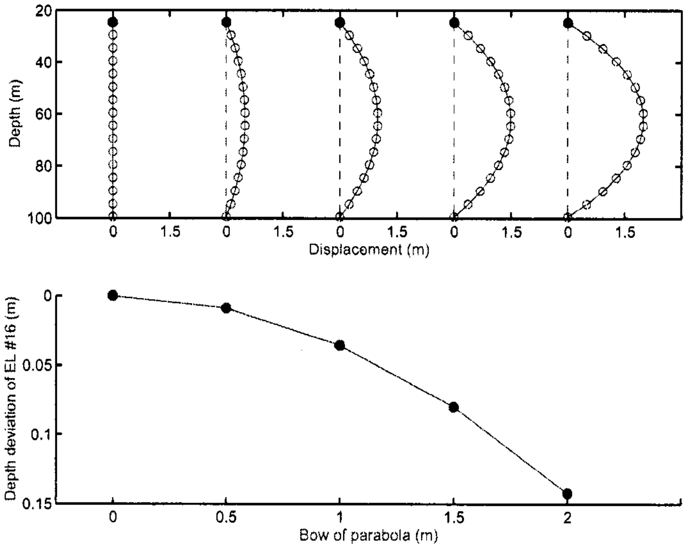

Figure A.1: Bowed-array shape in xz-plane and the depth deviation of the uppermost element for different bows: 0 m, 0.5 m, 1 m, 1.5 m and 2 m.

Appendix B

Empirical Orthogonal Functions

— *in which the details of EOF analysis are documented.*

One of the most ubiquitous uses of eigen analysis in data analysis is the construction of empirical orthogonal functions (EOFs) [20, 58]. EOFs are a transform of the data into a set of orthogonal basis vectors. In this sense the EOF transform is similar to other transforms such as the Fourier or Laplace transform: we project the original data onto a set of orthogonal functions, thus replacing the original data with the set of projection coefficients on the basis vectors. In EOF analysis, we also project the original data on a set of orthogonal basis vectors. However, the basis vectors of the EOF transform are determined by the data themselves, and therefore characterize the co-variability of the data records for a set of grid points in a more compact way.

Note that the number of EOFs is one less than the minimum of the number of records and grid size. The reason is that the sample mean vector has been extracted from the original data for constructing the covariance matrix.

B.1 Recipes

The EOF simulation algorithm can be summarized in the following steps: Given the measured data $\mathbf{C} = [\mathbf{c}_1, \mathbf{c}_2, \ldots, \mathbf{c}_n, \ldots, \mathbf{c}_N]$ where $\mathbf{c}_n$ is the n-th measured profile.

1. Re-sample each sound speed profile $\mathbf{c}_n$ on the given depth points $[z_1, z_2, \ldots, z_D]^T$.

2. Estimate the mean sound speed profile

$$\bar{\mathbf{c}} = \frac{1}{N}\sum_{n=1}^{N}\mathbf{c}_n. \tag{B.1}$$

3. Estimate the covariance matrix $\mathbf{R}$ of the CTD castings

$$\mathbf{R} = \frac{1}{N-1}\sum_{n=1}^{N}\left(\mathbf{c}_n - \bar{\mathbf{c}}\right)\left(\mathbf{c}_n - \bar{\mathbf{c}}\right)^T. \tag{B.2}$$

4. Eigenvalue decompose $\mathbf{R}$ into the eigenvectors and the corresponding eigenvalues.

$$\mathbf{R} = \mathbf{V}\mathbf{\Lambda}\mathbf{V}^T = \sum_{n=1}^{N}\lambda_n\mathbf{v}_n\mathbf{v}_n^T. \tag{B.3}$$

Given any one of the $\mathbf{c}_k$ and the eigenvectors $\mathbf{v}_i, i \in 1, ..., J$, where J is the number of the significant eigenvectors.

1. Subtract the mean from that profile: $\mathbf{c}'_k = \mathbf{c}_k - \bar{\mathbf{c}}$.
2. Project onto eigenvector space $\mathbf{a} = \mathbf{A}\mathbf{c}'_k$ where

$$\mathbf{A} = \left[\mathbf{v}_1|\mathbf{v}_2|\ldots|\mathbf{v}_J\right]^T \tag{B.4}$$

Therefore, a measured profile $\mathbf{c}_k$ can be written by a series representation of the first J eigenvectors:

$$\mathbf{c}_k = \bar{\mathbf{c}} + \sum_{j=1}^{J}a_j\mathbf{v}_j \tag{B.5}$$

where the coefficients a_j are given by the vector inner product

$$a_j = \mathbf{v}_j^T(\mathbf{c}_k - \bar{\mathbf{c}}). \tag{B.6}$$

B.2 Example: EOF Analysis on ASIAEX CTD Data

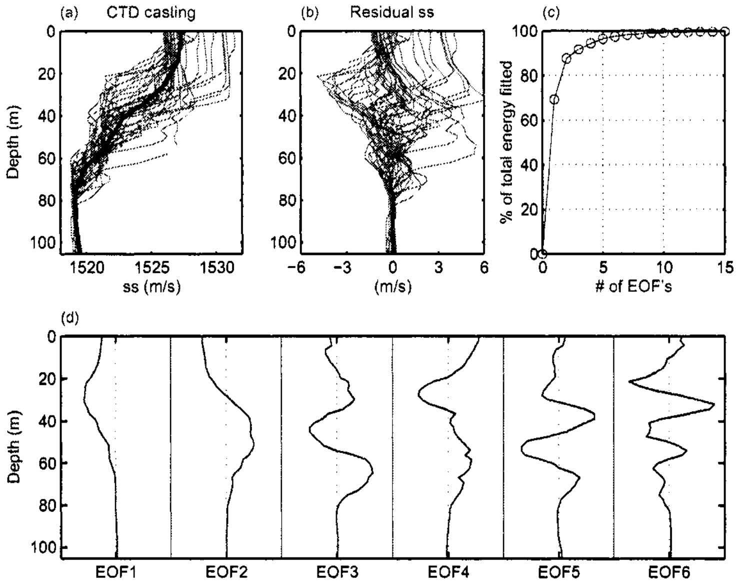

Figure B.1: Empirical Orthogonal Function (EOF) analysis for the 2001 ASIAEX CTD casts. (a) sound-speed profiles measured from R/V *Melville* and the average sound-speed profile (thick black line); (b) Residual sound-speed profiles; (c) Percent of total fit energy with limited sets of EOF's; (d) First 6 EOF's.

Table B.1: The EOF coefficients for the ocean sound-speed profiles measured during the acoustic transmissions (Fig. 2.4).

Measured SSP	EOF1	EOF2	EOF3	EOF4	EOF5	EOF6
CTD0123	9.39	−0.63	−0.80	1.97	2.20	−0.27
CTD0547	6.77	−2.50	0.52	2.79	0.03	−0.28
CTD0820	11.95	−4.04	−2.73	1.45	0.21	0.68

EOF i denotes the i-th EOF coefficient.

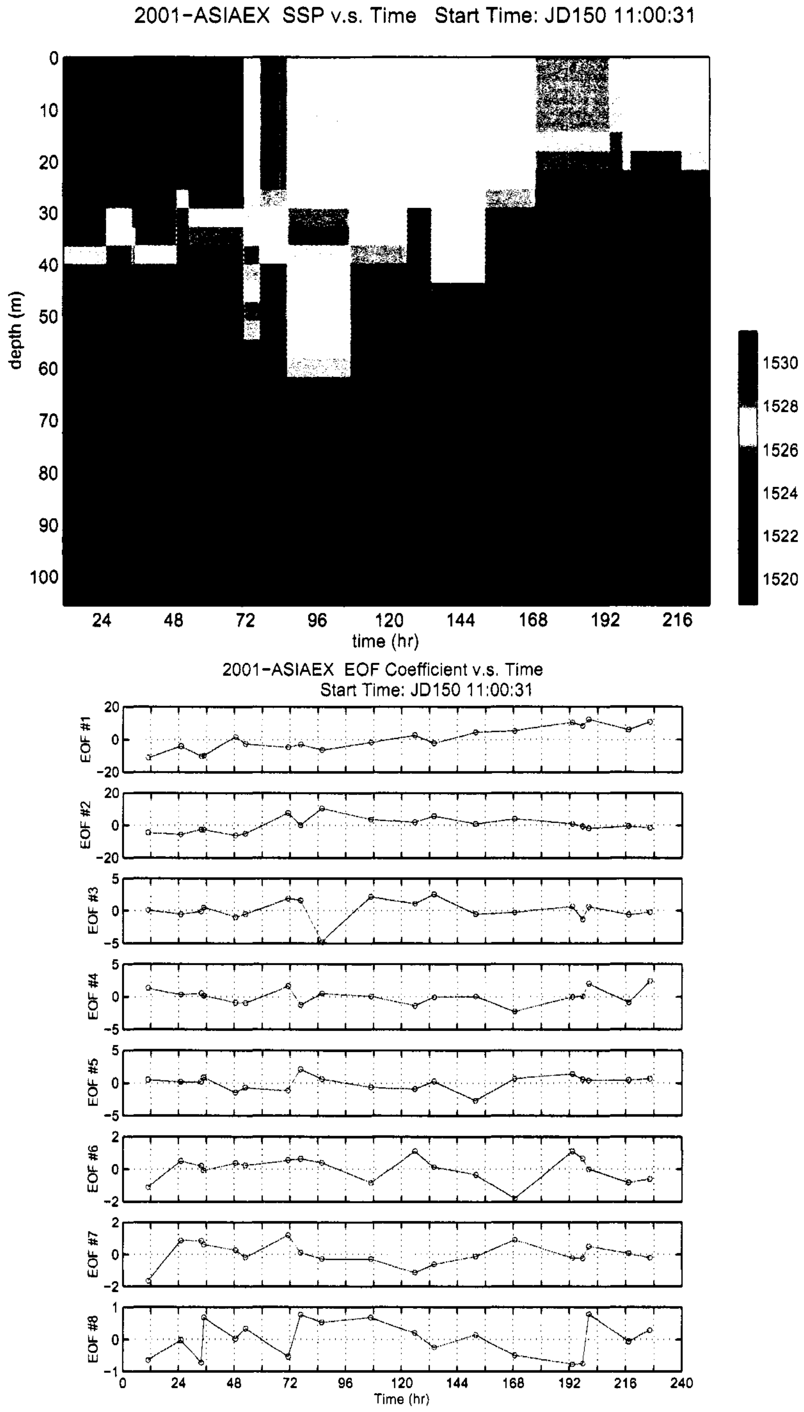

Figure B.2: Upper panel: measured sound-speed profiles as a function of time. Lower panel: time series of the estimated EOF coefficients of the above measured sound-speed profiles.

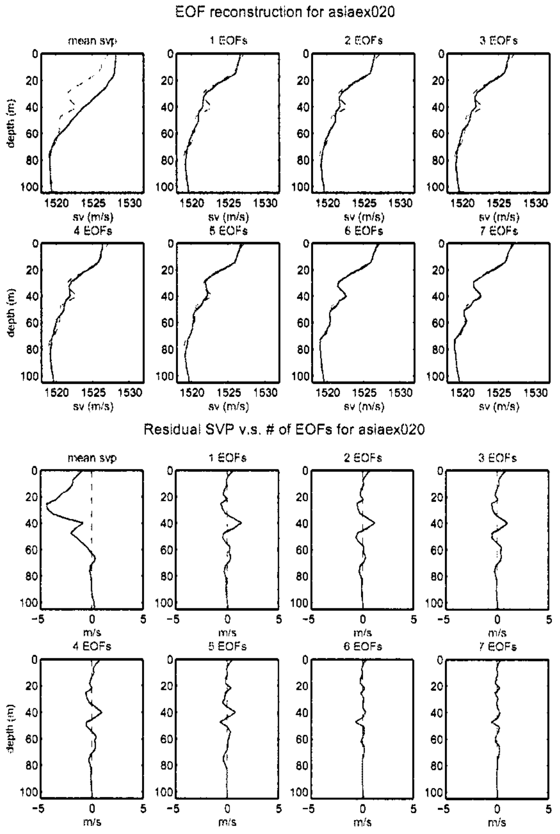

Figure B.3: Upper panel: reconstructed CTD0123 SSPs (solid line) using the mean plus different numbers of EOFs. Dashed line indicates CTD0123. Lower panel: residual SSP versus number of EOFs.

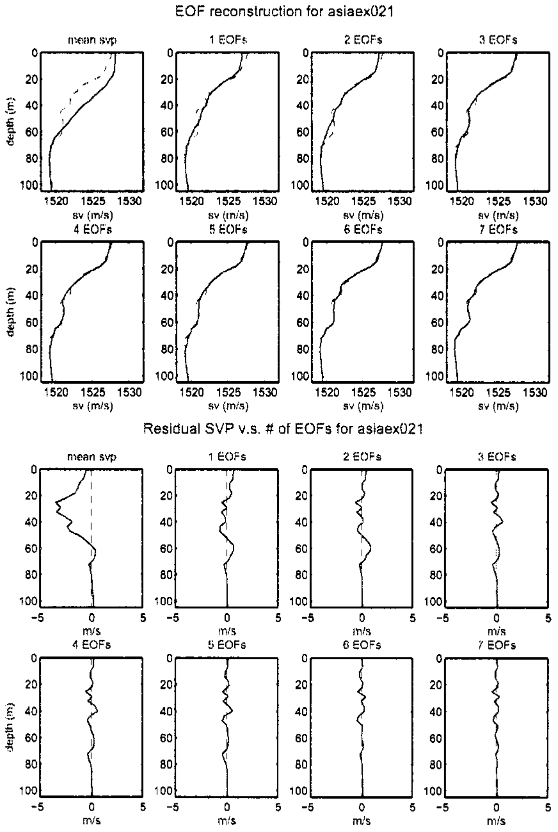

Figure B.4: Upper panel: reconstructed CTD0547 SSPs (solid line) using the mean plus different numbers of EOFs. Dashed line indicates CTD0547. Lower panel: residual SSP versus number of EOFs.

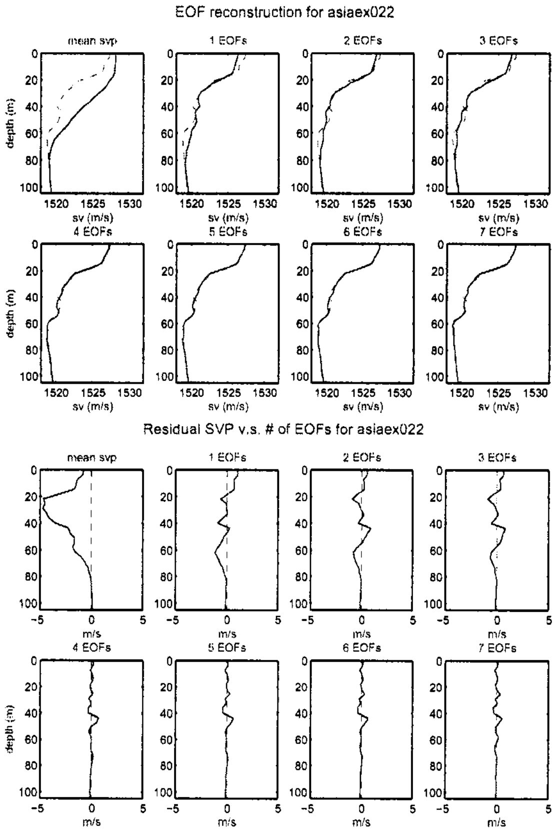

Figure B.5: Upper panel: reconstructed CTD0820 SSPs (solid line) using the mean plus different numbers of EOFs. Dashed line indicates CTD0820. Lower panel: residual SSP versus number of EOFs.

Appendix C

Monte Carlo Sampling Algorithm

— in which the Monte Carlo integration is described briefly,
and the algorithm implemented in SAGA is documented.

Under the Bayesian approach the solution to inverse problems is the posterior probability distribution (PPD) of model parameters, $\mathrm{p}(\mathbf{m}|\mathbf{d})$. Due to multi-dimensionality the PPD is not susceptible to graphic display, and mainly integral properties of the distribution are of interest. From the PPD, all the desired statistical quantities such as the means, variances and the marginal 1D/2D PPDs will be extracted to describe the solution. These quantities can be written as expectations of relevant functions $f(\mathbf{m})$[‡] under $\mathrm{p}(\mathbf{m}|\mathbf{d})$, as follows:

$$I = \mathrm{E}[f(\mathbf{m})] = \int f(\mathbf{m})\mathrm{p}(\mathbf{m}|\mathbf{d})\mathrm{d}\mathbf{m}. \tag{C.1}$$

When the dimension of the model parameters is very small, a grid integration over the model space is a practical way of solving the above integration. When the dimension of the parameter space is high, this can be very difficult to obtain. Monte Carlo integration using MCMC is one answer to this problem.

[‡] For example, if the desired statistical quantity is the mean of the parameters, then $f(\mathbf{m}) = \mathbf{m}$. As for the marginal PPD of the i-th parameter, i.e., $I = \mathrm{p}(m_i|\mathbf{d})$, then

$$f(\mathbf{m}) = \delta(\mathbf{m} - m_i).$$

Monte Carlo integration estimates the integral of Eq. (C.1) by obtaining samples $\mathbf{m}_t$, $t = 1, \ldots, n$, from the distribution $\mathrm{p}(\mathbf{m}|\mathbf{d})$ and calculating

$$I \approx \frac{1}{n} \sum_{t=1}^{n} f(\mathbf{m}_t) \tag{C.2}$$

Section C.1 describes deterministic methods of numerical integration and followed by a discussion of Monte Carlo integration. Section C.1.1 presents a class of MCMC sampling algorithms: Metropolis-Hastings sampler to obtain the samples that approximate the PPD. Section C.2 summarizes the Monte Carlo sampling algorithm implemented in SAGA. Finally, a list of the SAGA options is tabulated.

C.1 Numerical Integration

Deterministic methods

Deterministic methods of numerical integration operate by defining a grid over the model space and computing $\mathrm{p}(\mathbf{m}|\mathbf{d})$ everywhere in the grid and directly use these results to calculate the desired quantities. Although the most precise and direct method, numerical integration is extremely computationally intensive. For M model parameters each discretized to k values, it requires k^M forward model evaluations. For example, $k = 100$ and $M = 10$, this is a prohibitively large number 100^{10}, as for each of these points, a forward model that takes about one CPU-second must be evaluated. This approach is practical only for a very small number of parameters, e.g., $M \leq 8$.

Monte Carlo methods

Monte Carlo methods provide a way out of this exponential time-increase. In Monte Carlo integration the integration points are selected at random from a uniform distribution. It is not necessary to evaluate the integral at all points as in a grid search. In contrast to deterministic computing methods, the efficiency of Monte Carlo integration depends only weakly on the dimension and geometric details of the problem. Thus, even for high dimensions and complicated boundaries of the parameter set $\mathcal{M}$, the numerical effort remains moderate. The integral is evaluated at randomly selected points from a uniform distribution. The disadvantage is that many of these points will be located in areas contributing little to the integral.

A refinement of the Monte Carlo integration method is to somehow make the points random, but more likely to come from regions of high contribution to the integral than from regions of low contribution. MCMC sampling algorithms provide a way to obtain the samples that approximate the PPD.

C.1.1 Metropolis-Hastings Sampler

The Metropolis-Hastings algorithm described here is strongly inspired by Martinez and Martinez [62]. The algorithm consists of two repeated steps. In the exploration step, the current parameter vector $\mathbf{m}$ is modified at random to obtain a "candidate" vector $\mathbf{m}'$. This candidate is drawn from a "proposal" distribution $q(\mathbf{m}'|\mathbf{m})$, where the choice of $\mathbf{m}'$ depends on the current vector $\mathbf{m}$. In the exploitation step, the parameter vector is changed to $\mathbf{m}'$ with an "acceptance probability"

$$\alpha(\mathbf{m}'|\mathbf{m}) = \min\left[1, \frac{\pi(\mathbf{m}')}{\pi(\mathbf{m})}\frac{q(\mathbf{m}|\mathbf{m}')}{q(\mathbf{m}'|\mathbf{m})}\right] \tag{C.3}$$

where the target distribution $\pi(\mathbf{m})$ represents the PPD of $\mathbf{m}$. Note that the target distribution does not have to be normalized, since what matters is the ratio of the distributions. The acceptance probability in Eq. (C.3) effectively guides the random walk toward regions of parameter space that have higher posterior probabilities. It can be proven that this algorithm will asymptotically sample the posterior pdf (see Chib and Greenberg [15]).

The Metropolis sampler (the original method of Metropolis *et al.* [65]) is a special case of the Metropolis-Hastings methods, where symmetric distributions are considered for the proposal distribution. Thus we have

$$q(\mathbf{m}'|\mathbf{m}) = q(\mathbf{m}|\mathbf{m}'). \tag{C.4}$$

Then those terms cancel out in the acceptance probability yielding

$$\alpha(\mathbf{m}'|\mathbf{m}) = \min\left[1, \frac{\pi(\mathbf{m}')}{\pi(\mathbf{m})}\right]. \tag{C.5}$$

Usually the Boltzmann probability distribution is used for the likelihood function and a uniform prior is assumed for each parameter. Then, the target function is

$$\pi(\mathbf{m}) = \mathrm{p}(\mathbf{m}|\mathbf{d}) \propto \exp\left(-\frac{\phi(\mathbf{m})}{\mathrm{T}}\right) \tag{C.6}$$

where $\phi(\mathbf{m})$ is the objective function and T is the temperature or the error variance. Here, an analytical consideration of the likelihood function, in which the error variance is integrated out analytically (see discussion in Chapter 4 and Eq. (4.23)), is used and it yields

$$\pi(\mathbf{m}) = \mathrm{p}(\mathbf{m}|\mathbf{d}) \propto \phi(\mathbf{m})^{-\mathrm{N}}. \tag{C.7}$$

Therefore, the acceptance function can be rewritten as:

$$\alpha(\mathbf{m}'|\mathbf{m}) = \min\left\{1, \left[\frac{\phi(\mathbf{m}')}{\phi(\mathbf{m})}\right]^{-N}\right\}. \tag{C.8}$$

Procedure – Metropolis-Hastings/Metropolis Sampler

One starts from an arbitrary points $\mathbf{m}_0$ and generates the sequence by repeating the following cycle, with $\mathbf{m}_t$ being the previously selected point at each iteration:

1. The exploration step. Select a new candidate point $\mathbf{m}'$ chosen according to a symmetric proposal distribution $q(\mathbf{m}'|\mathbf{m}_t)$.
2. The exploitation step. Decide if the candidate point should be accepted as the next point. Calculate the acceptance probability Eq. (C.3). Accept $\mathbf{m}'$ with probability $\alpha(\mathbf{m}'|\mathbf{m}_t)$, *i.e.*
    (a) if $\pi(\mathbf{m}')q(\mathbf{m}_t|\mathbf{m}') \geq \pi(\mathbf{m}_t)q(\mathbf{m}'|\mathbf{m}_t)$, then accept $\mathbf{m}'$;
    (b) if $\pi(\mathbf{m}')q(\mathbf{m}_t|\mathbf{m}') < \pi(\mathbf{m}_t)q(\mathbf{m}'|\mathbf{m}_t)$, extract a uniform random number between 0 and 1 and accept $\mathbf{m}'$ if the random number is less than $\frac{\pi(\mathbf{m}')}{\pi(\mathbf{m})}\frac{q(\mathbf{m}|\mathbf{m}')}{q(\mathbf{m}'|\mathbf{m})}$.

   If the point is accepted, then $\mathbf{m}_{t+1} = \mathbf{m}'$. Otherwise $\mathbf{m}_{t+1} = \mathbf{m}_t$.

Repeat the above n times where n sufficiently beyond point of convergence to target distribution and sufficiently large to achieve desired precision for estimate of interest.

C.2 Monte Carlo Sampling Algorithm Implemented in SAGA

The Monte Carlo sampling algorithm implemented in SAGA consists of the following components: 1) a burn-in period, 2) sampling PPD of **m**, 3) convergence monitoring.

C.2.1 Burn-in Period

The purpose of the burn-in period is to have a good starting point, near a point where the likelihood is maximum, thus we avoid heavy sampling in non-important areas of the model space. For this purpose, a optimization algorithm such as simulating annealing or genetic algorithms can be used to find a point in a high-posterior probability region.

C.2.2 Sampling PPD of m

The choice of the proposal distribution $q(\mathbf{m}'|\mathbf{m})$ will have a large effect on the efficiency of the algorithm. For example, suppose that the current parameter vector $\mathbf{m}$ is in a high-posterior probability region. If the proposed modifications to $\mathbf{m}$ are large compared to the spread of the posterior distribution, $\mathbf{m}'$ will typically have a low posterior probability, α in Eq. (C.3) will be small, and it will take many iterations before a proposed move is accepted. At the other extreme, if the changes proposed are too small, α will be large, but many iterations will be needed to cover the high-posterior probability region of the parameter space [15]. The best choice for $q(\mathbf{m}'|\mathbf{m})$ would be a pdf that approximates as closely as possible the posterior distribution of $\mathbf{m}$.

Sampling interval

For a Metropolis sampler, the next model $\mathbf{m}_{t+1}$ is selected based the current model $\mathbf{m}_t$.

$$\mathbf{m}_{t+1} = \mathbf{m}_t + \Delta\mathbf{m}_t \tag{C.9}$$

where $\Delta\mathbf{m}_t$ is a random move selected from the distribution $q(I_t)$ and I_t is the search interval. This is often referred to as the move class in simulating annealing vocabulary.

For a Metropolis sampler the move class q should be a uniform distribution from the whole sampling interval for each parameter. This will ensure an unbiased convergence to the posterior distribution.

However, this can be quite slow in practice. Improvement might involve either a reduction of the search interval, or using a non-uniform distribution. In essence, both approaches are similar as they both attempt to modify the uniform distribution $q(I_t)$.

The default is to assume a uniform distribution over the whole search space, as this assures convergence. If there is only one main minimum overlaying with small ripples, then a smaller move class can be used with a significant saving in computation time. Inspired by Dosso [22], the following algorithm is used

$$I_t = \max(I_{t-1}, k_{\text{grow}} * \Delta_{\text{obs}}) * f_{\text{decay}} \tag{C.10}$$

subject to $I_{t+1} > I_0$, so that the interval cannot become too small. Δ_{obs} is the size of the current accepted move. Typically $I_0 = 0.01\%$ of the search interval, $f_{\text{decay}} = 0.99$, and $k_{\text{grow}} = 2$.

Parameter Coordinate Rotation

In ocean acoustics, parameter correlations are frequently encountered [26] and a parameter covariance matrix computed from field derivatives contains information about parameter coupling [17]. As noted by Collins and Fishman [17] and others, a simulating annealing algorithm benefits from the coordinate rotation, when sampling strongly correlated parameter spaces. Collins and Fishman [17] originally suggested using the covariance matrix of the derivative field. However, to compute the gradient of the pressure vector does in general require $M + 1$ forward model evaluations for an M-parameter problem, thus it can be computational demanding, and further it does not fit well into a Metropolis sampler which does not use gradient information.

Instead, Dosso [22] has suggested to use the covariance matrix of the accepted sampled vectors as $\mathbf{C}_{\text{M}}$. He found that often this covariance matrix works as well as using the gradient covariance matrix.

Here, the covariance matrix estimated from the accepted sampled vectors $\mathbf{m}$ is used for determining the coordinate rotations. By using the eigenvalue decomposition expression of $\mathbf{C}_{\mathrm{M}} = \mathbf{U}\mathbf{\Lambda}\mathbf{U}^{\mathrm{T}}$, the parameter coordinate is rotated via the following transformation

$$\Delta\tilde{\mathbf{m}} = \mathbf{U}^{\mathrm{T}}\Delta\mathbf{m}. \tag{C.11}$$

Then, the transformed coordinate is aligned with the parameter landscape

$$\begin{aligned} \mathsf{E}[\Delta\tilde{\mathbf{m}}\Delta\tilde{\mathbf{m}}^{\mathrm{T}}] &= \mathsf{E}[\mathbf{U}^{\mathrm{T}}\Delta\mathbf{m}\Delta\mathbf{m}^{\mathrm{T}}\mathbf{U}] \\ &= \mathbf{U}^{\mathrm{T}}\mathsf{E}[\Delta\mathbf{m}\Delta\mathbf{m}^{\mathrm{T}}]\mathbf{U} \\ &= \mathbf{U}^{\mathrm{T}}\mathbf{C}_{\mathrm{M}}\mathbf{U} \\ &= \mathbf{\Lambda}, \end{aligned} \tag{C.12}$$

The parameter coordinate may be different for different parts of the parameter space. In SAGA, the parameter coordinate is rotated when the maximum difference of the two covariance matrices estimated from parallel chains for the previous m iterations is larger than a prescribed threshold ϵ_{rot}, typically with $\epsilon_{\mathsf{rot}} = 0.1$.

C.2.3 Convergence Monitoring

As we were mainly interested in marginal PPDs, we use a dual-population convergence criteria [22], i.e., the total difference between the marginal distributions for all parameters is less than a prescribed threshold ϵ_{stop}, typically with $\epsilon_{\mathsf{stop}} = 0.1$. Since each chain is run independently, any convergence problems are more likely to appear with dispersed starting points.

C.3 Options in SAGA

The Monte Carlo sampling is started using option `S` (iopt(4)=0). On a new line below the GA parameters the user must specify

```
nu e_stop e_rot k_grow N_eff
```

where

`nu` is the error variance in Eq. (4.45).

`e_stop` is the convergence criteria (recommended value 0.1).

`e_rot` is the criteria for accuracy of the matrix before rotating (recommended value 0.1).

`k_grow` is the factor in Eq. (C.10).

`N_eff` is the parameter in Eq. (4.23).

Options

`S0`	(default) (isubopt(4)=0) perturbs one parameter at a time.
`S1`	(isubopt(4)=1) perturbs all parameters at once. For some cases this can cause premature convergence. Often it is faster.
`Sx1`	(isubopt(35)=1) Use the adaptive search interval.
`S2`	enumerative integration for $M \leq 8$.
`*`	(isubopt(36)=2) uses the acceptance distribution in Eq. (C.8). Either `S`, `S1` or `Sx1` should always be specified. When this option is used, the error variance is integrated out *a priori*, and the parameter `N_eff` is required.

Graphic

For the Monte Carlo integrations, marginal PPD for each parameter can be obtained using MATLAB

```
>> plotgibbs('filename')
```

For the enumerative integration, marginal PPDs can also be plotted

```
>> plotenum('filename')
```

Bibliography

[1] P. Abbot and I. Dyer. Sonar performance predictions based on environmental variability. In N. G. Pace and F. B. Jensen, editors, *Impact of Littoral Environmental Variability on Acoustic Predictions and Sonar Performance*, pages 611–618. Kluwer, The Netherlands, 2002.

[2] J. J. K. Ó Ruanaidh and W. J. Fitzgerald. *Numerical Bayesian methods applied to signal processing.* Statistics and Computing Series. Springer, New York, 1996.

[3] G. E. Backus and F. J. Gilbert. The resolving power of gross earth data. *Geophys. J. Roy. Astron. Soc.*, 16:169–205, 1968.

[4] G. E. Backus and F. J. Gilbert. Uniqueness in the inversion of inaccurate gross earth data. *Philos. Trans. Roy. Soc. London Ser. A*, 266(1173):123–192, 1970.

[5] A. B. Baggeroer, W. A. Kuperman, and H. Schmidt. Matched field processing: Source localization in correlated noise as an optimum estimation problem. *J. Acoust. Soc. Amer.*, 83(2):571–587, Feb. 1988.

[6] D. Battle, P. Gerstoft, W. S. Hodgkiss, W. A. Kuperman, and P. Nielsen. Bayesian model selection applied to self-noise geoacoustic inversion. *J. Acoust. Soc. Amer.*, 116:2043–2056, 2004.

[7] C. M. Bender and S. A. Orszag. *Advanced Mathematical Methods for Scientists and Engineers: Asymptotic methods and perturbation theory.* Springer-Verlag, New York, 1999.

[8] G. E. P. Box and G. C. Tiao. *Bayesian inference in statistical analysis.* Addison–Wesley, New York, 1992.

[9] G. L. Bretthorst. *Bayesian spectrum analysis and parameter estimation.* Springer-Verlag, New York, 1988.

[10] H. P. Bucker. Use of calculated sound field and matched-field detection to locate sound sources in shallow water. *J. Acoust. Soc. Amer.*, 59:368373, 1976.

[11] B. P. Carlin and T. A. Louis. *Bayes and Empirical Bayes methods for data analysis.* Chapman and Hall, London, 2nd edition, 2000.

[12] N. R. Chapman, S. Chi-Bing, D. King, and R. B. Evans. Benchmarking geoacoustic inversion methods in range dependent waveguides. *IEEE J. Oceanic Eng.*, 28:320–330, 2003.

[13] N. R. Chapman and C. E. Lindsay. Matched-field inversion for geoacoustic model parameters in shallow water. *IEEE J. Oceanic Eng.*, 21(4):347–354, Oct 1996.

[14] N. R. Chapman, K. S. Ozard, and M. L. Yeremy. Error bounds in matched-field inversion for geoacoustic properties. *J. Comp. Acoust.*, 7:1–13, 1999.

[15] S. Chib and E. Greenberg. Understanding the Metropolis-Hastings algorithm. *The American Statistician*, 49:327–335, 1995.

[16] M. D. Collins. A split-step Padé solution for the parabolic equation method. *J. Acoust. Soc. Amer.*, 93:1736–1742, 1993.

[17] M. D. Collins and L. Fishman. Efficient navigation of parameter landscapes. *J. Acoust. Soc. Amer.*, 98(3):1637–1644, 1995.

[18] M. D. Collins and W. A. Kuperman. Focalization: Environmental focusing and source localization. *J. Acoust. Soc. Amer.*, 90:1410–1422, 1991.

[19] M. D. Collins, W. A. Kuperman, and H. Schmidt. Nonlinear inversion for ocean-bottom properties. *J. Acoust. Soc. Amer.*, 92:2770–2783, 1992.

[20] R. E. Davis. Predictability of sea surface temperature and sea level pressure anomalies over the north pacific ocean. *Journal of Physical Oceanography*, 6(3):249–266, May 1976.

[21] D. R. DelBalzo, C. Feuillade, and M. Rowe. Effects of water-depth mismatch on matched-field localization in shallow water. *J. Acoust. Soc. Amer.*, 83:2180–2185, 1988.

[22] S. E. Dosso. Quantifying uncertainty in geoacoustic inversion I: A fast Gibbs sampler approach. *J. Acoust. Soc. Amer.*, 111:129–142, 2002.

[23] S. E. Dosso. Probabilistic geoacoustic inversion. *J. Acoust. Soc. Amer.*, 113(4):2189–2190, 2003.

[24] S. E. Dosso and P. L. Nielsen. Quantifying uncertainty in geoacoustic inversion II: Application to broadband, shallow-water data. *J. Acoust. Soc. Amer.*, 111:143–159, 2002.

[25] S. E. Dosso, M. L. Yeremy, J. M. Ozard, and N. R. Chapman. Estimation of ocean-bottom properties by matched-field inversion of acoustic field data. *IEEE J. Oceanic Eng.*, 18:232–239, 1993.

[26] G. L. D'Spain, J. J. Murray, W. S. Hodgkiss, N. O. Booth, and P. W. Schey. Mirages in shallow water matched field processing. *J. Acoust. Soc. Amer.*, 105:3245–3265, 1999.

[27] M. R. Fallat and S. E. Dosso. Geoacoustic inversion for the Workshop'97 benchmark test cases using simulated annealing. *J. Comp. Acoust.*, 6:29–44, 1998.

[28] M. R. Fallat and S. E. Dosso. Geoacoustic inversion via local, global and hybrid algorithms. *J. Acoust. Soc. Amer.*, 105:3219–3230, 1999.

[29] M. R. Fallat, P. L. Nielsen, and S. E. Dosso. Hybrid geoacoustic inversion of broadband Mediterranean sea data. *J. Acoust. Soc. Amer.*, 107:1967–1977, 2000.

[30] C. Feuillade, D. R. DelBalzo, and M. M. Rowe. Environmental mismatch in shallow-water matched-field processing: geoacoustic parameter variability. *J. Acoust. Soc. Amer.*, 85:2354–2364, 1989.

[31] P. Gerstoft. Global inversion by genetic algorithms for both source position and environmental parameters. *J. of Computational Acoustics*, 2:251–266, 1994.

[32] P. Gerstoft. Inversion of seismoacoustic data using genetic algorithms and *a posteriori* probability distributions. *J. Acoust. Soc. Amer.*, 95:770–782, 1994.

[33] P. Gerstoft. Inversion of acoustic data using a combination of genetic algorithms and the Gauss-Newton approach. *J. Acoust. Soc. Amer.*, 97:2181–2190, 1995.

[34] P. Gerstoft. *SAGA Users guide 5.0, an inversion software package.* An updated version of "SAGA Users guide 2.0, an inversion software package," SACLANT Undersea Research Centre, SM–333, La Spezia, Italy, 1997.

[35] P. Gerstoft and D. F. Gingras. Parameter estimation using multifrequency range-dependent acoustic data in shallow water. *J. Acoust. Soc. Amer.*, 99:2839–2850, 1996.

[36] P. Gerstoft, W. S. Hodgkiss, W. A. Kuperman, and H. Song. Phenomenological and global optimization inversion. *IEEE J. Oceanic Eng.*, 28:342–354, 2003.

[37] P. Gerstoft, C.-F. Huang, and W. S. Hodgkiss. Estimation of transmission loss in the presence of geoacoustic inversion uncertainty. *IEEE J. Oceanic Eng.*, in press, 2005.

[38] P. Gerstoft and C. F. Mecklenbräuker. Ocean acoustic inversion with estimation of *a posteriori* probability distributions. *J. Acoust. Soc. Amer.*, 104:808–819, 1998.

[39] D. F. Gingras. Methods for predicting the sensitivity of matched-field processors to mismatch. *J. Acoust. Soc. Amer.*, 86:1940–1949, 1989.

[40] D. F. Gingras and P. Gerstoft. Inversion for geometric and geoacoustic parameters in shallow water: experimental results. *J. Acoust. Soc. Amer.*, 97:3589–3598, 1995.

[41] R. M. Hamson and R. M. Heitmeyer. Environmental and system effects on source localiztion in shallow water by the matched-field processing of a vertical array. *J. Acoust. Soc. Amer.*, 86:1951–1959, 1989.

[42] J. P. Hermand and P. Gerstoft. Inversion of broadband multi-tone acoustic data from the YELLOW SHARK summer experiment. *IEEE J. Oceanic Eng.*, 21:324–346, 1996.

[43] W. S. Hodgkiss, D. E. Ensberg, J. J. Murray, G. L. D'Spain, N. O. Booth, and P. W. Schey. Direct measurement and matched-field inversion approaches to array shape estimation. *IEEE J. Oceanic Eng.*, 21:393–401, 1996.

[44] C.-F. Huang, P. Gerstoft, and W. S. Hodgkiss. Uncertainty analysis in matched-field geoacoustic inversions. *J. Acoust. Soc. Amer.*, accepted upon revision, 2005.

[45] C.-F. Huang and W. S. Hodgkiss. Mid-frequency geoacoustic inversion of source tow data from the ASIAEX East China Sea experiment. *Oceans2003 MTS/IEEE*, pages 576–581, 2003.

[46] C.-F. Huang and W. S. Hodgkiss. Matched field geoacoustic inversion of low frequency source tow data from the ASIAEX East China Sea experiment. *IEEE J. Oceanic Eng.*, 29:952–963, October 2004.

[47] P. Hursky, M. B. Porter, M. Siderius, and V. K. McDonald. High-frequency (8–16 kHz) model-based source localization. *J. Acoust. Soc. Amer.*, 115(6):3021–3032, 2004.

[48] L. Jaschke and N. R. Chapman. Matched field inversion of broadband data using the freeze bath method. *J. Acoust. Soc. Amer.*, 106:1838–1851, 1999.

[49] E. Jaynes. Prior probabilities. *IEEE transactions on systems science and cybernetics*, SSC-4:227–241, 1968.

[50] E. T. Jaynes. *Probability Theory: The Logic of Science.* Cambridge University Press, New York, 2003.

[51] H. Jeffreys. *Theory of probability.* Oxford University Press, New York, 1939.

[52] F. B. Jensen and M. C. Ferla. *SNAP: the SACLANTCEN normal-mode acoustic propagation model.* SACLANT Undersea Research Centre, SM–121, La Spezia, Italy, 1979.

[53] F. B. Jensen, W. A. Kuperman, M. B. Porter, and H. Schmidt. *Computational Ocean Acoustics.* Springer-Verlag, New York, 2000.

[54] F. B. Jensen and N. Pace. *Impact of Littoral Environmental Variability on Acoustic Predictions and Sonar Performance.* Kluwer, The Netherlands, 2002.

[55] S. M. Jesus and A. Caiti. Estimating geoacoustic bottom properties from towed array data. *J. of Computational Acoustics*, 4(3):273–290, 1996.

[56] R. T. Kessel and N. R. Chapman. Search grid mismatch in matched field processing (MFP) for source localization. In *Proc. of the fifth European conference on underwater acoustics*, pages 959–964, Lyon, France, 2000.

[57] D. P. Knobles, R. A. Koch, L. A. Thompson, K. C. Focke, and P. E. Eisman. Broadband sound propagation in shallow water and geoacoustic inversion. *J. Acoust. Soc. Amer.*, 113:205–222, 2003.

[58] L. R. LeBlanc and F. H. Middleton. An underwater acoustic sound velocity data model. *J. Acoust. Soc. Amer.*, 67:2055–2062, 1980.

[59] J. F. Lynch and P. H. Dahl, editors. *IEEE Journal of Oceanic Engineering Special Issue on the Asian Marginal Seas*, volume 29. IEEE, 2004.

[60] D. J. C. MacKay. *Information Theory, Inference and Learning Algorithms.* Cambridge University Press, 2003.

[61] A. Malinverno. A Bayesian criterion for simplicity in inverse problem parametrization. *Geophy. J. Int.*, 140:267–285, 2000.

[62] W. L. Martinez and A. R. Martinez. *Computational Statistics Handbook with MATLAB.* Chapman & Hall/CRC, Boca Raton, 2002.

[63] C. F. Mecklenbräuker and P. Gerstoft. Objective functions for ocean acoustic inversion derived by likelihood methods. *J. Comp. Acoust.*, 8:259–270, 2000.

[64] C. F. Mecklenbräuker, P. Gerstoft, J. Bohme, and P. Chung. Hypothesis testing for geoacoustic environmental models using likelihood ratio. *J. Acoust. Soc. Amer.*, 105:1738–1748, 1999.

[65] N. Metropolis, A. W. Rosenbluth, M. N. Rosenbluth, A. H. Teller, and E. Teller. Equation of state calculations by fast computing machines. *Journal of Chemistry and Physics*, 21:1087–1092, 1953.

[66] Z.-H. Michalopoulou and M. Picarelli. A Gibbs sampling approach to maximum *a posteriori* time delay and amplitude estimation. In *Proceedings of IEEE ICASSP '02*, volume 3, pages 3001–3004. IEEE Press, 2002.

[67] J. H. Miller, L. R. Bartek, G. R. Potty, D. Tang, J. Na, and Y. Qi. Sediments in the East China Sea. *IEEE J. Oceanic Eng.*, 29:940–951, 2004.

[68] K. Mosegaard and M. Sambridge. Monte Carlo analysis of inverse problems. *Inverse Problems*, 18(3):29–54, July 2002.

[69] K. Mosegaard and A. Tarantola. Probabilistic approach to inverse problems. In *International Handbook of Earthquake & Engineering Seismology, Part A*, pages 237–265. Academic Press, 2002.

[70] R. L. Parker. *Geophysical Inverse Theory.* Princeton NJ, Princeton University, 1994.

[71] G. R. Potty, J. H. Miller, J. F. Lynch, and K. Smith. Tomographic inversion for sediment parameters in shallow water. *J. Acoust. Soc. Amer.*, 108:973–986, 2000.

[72] L. T. Rogers, M. Jablecki, and P. Gerstoft. Posterior distribution of a statistic of propagation loss estimated from radar sea clutter. *Radar Science (in press)*, 2005.

[73] H. Schmidt. *OASES Version 2.2: user guide and reference manual.* Massachusetts Institute of Technology, Cambridge, MA, 1999.

[74] M. K. Sen and P. L. Stoffa. Bayesian inference, Gibbs' sampler and uncertainty estimation in geophysical inversion. *Geophys. Prosp.*, 44:313–350, 1996.

[75] M. Siderius, M. Snellen, D. Simons, and R. Onken. An environmental assessment in the Strait of Sicily: measurement and analysis techniques for determining bottom and oceanographic properties. *IEEE J. Oceanic Eng.*, 25:364–386, 2000.

[76] A. Tarantola. *Inverse Problem Theory: Methods for Data Fitting and Model Parameter Estimation.* Elsevier, Amsterdam, 1987.

[77] A. Tarantola. *Inverse Problem Theory and Methods for Model Parameter Estimation.* SIAM, Philadelphia, 2005.

[78] A. Tarantola and B. Valette. Inverse problems = quest for information. *Journal of Geophysics*, 50:159–170, 1982.

[79] M. I. Taroudakis and M. G. Markaki. Bottom geoacoustic inversion by "broadband" matched field processing. *J. Comp. Acoust.*, 16(2):167–183, 1998.

[80] D. Tollefsen. *User interface to ASSA and FGS with ORCA90.* Norwegian Defence Research Establishment, FFI/NOTAT-2002/04824, Kjeller, Norway, 2002.

[81] A. Tolstoy, N. R. Chapman, and G. Brooke. Workshop'97: Benchmarking for geoacoustic inversion in shallow water. *J. Comp. Acoust.*, 6(1&2):1–28, 1998.

[82] E. K. Westwood, C. T. Tindle, and N. R. Chapman. A normal mode model for acoustoelastic ocean environments. *J. Acoust. Soc. Amer.*, 100:3631–3645, 1996.

[83] M. J. Wilmut, S. E. Dosso, and J. Dettmer. Data error estimation for matched-field geoacoustic inversion. *J. Acoust. Soc. Amer.*, 115(5):2408–2409, 2004.